THE DESIGN, FABRICATION AND TESTING OF A HIGH FREQUENCY, ANGLED ULTRASOUND ENDOSCOPE FOR MINIMALLY INVASIVE SPINE SURGERY

by

Theresa Gu

Submitted in partial fulfillment of the requirements
for the degree of Master of Applied Science

at

Dalhousie University
Halifax, Nova Scotia
June 2023

Dalhousie University is located in Mi'kma'ki, the
ancestral and unceded territory of the Mi'kmaq.
We are all Treaty people

To my family, thank you

TABLE OF CONTENTS

LIST OF TABLES

LIST OF FIGURES

ABSTRACT

Minimally invasive spine surgery is often used to alleviate the symptoms of pathologies that compress the neural structures within the spine, creating a need for better imaging guidance within the limited surgical space.

An angled, high-resolution, small form factor ultrasound endoscope was designed, fabricated, and tested in-lab to provide ultrasound guidance during minimally invasive spine decompression surgeries. The probes were tested for safety and their ultrasound parameters characterized. Images were taken of a human volunteer's wrist and an ex vivo porcine spine.

Two probes were characterized to have an axial resolution of 33-45 μm, a lateral resolution of 130-116 μm, and secondary lobes suppressed to under -60 dB. The probes then demonstrated the capability to delineate both wrist and spinal canal anatomy, where power Doppler visualized blood flow in the wrist and B-mode visualized deformations of the spinal cord's contour upon manipulation by surgical instruments.

LIST OF ABBREVIATIONS USED

CSF	cerebrospinal fluid
CT	computed tomography
FED	full endoscopic discectomies
ICE	intra-cardiac-echocardiography
IEC	International Electrotechnical Commission
IOUS	intraoperative ultrasound
IVUS	intravascular ultrasound
MED	microendoscopic discectomy
MISS	minimally invasive spine surgery
MI	mechanical index
MRI	magnetic resonance imaging
PCB	printed circuit board
PZT	lead zirconate titanate
SAG	sagittal
SCF	sign coherence factor
TI	thermal index
TR	transverse
TMM	tissue mimicking material

ACKNOWLEDGEMENTS

First and foremost, I would like to express my sincere gratitude towards my thesis supervisor, Dr. Jeremy Brown, and co-supervisor, Dr. Tom Landry, for their continued patience and support throughout my studies. This work would not be possible without their knowledge, and their continued patience with all my questions at nonsensical times of day.

I would like to then express my gratitude towards my thesis and defense committee, Dr. Rob Adamson, Dr. Sean Christie, and Dr. Kimberly Brewer for their directions during the conception of this work, their continued input in improving this thesis, and their patience through this entire process.

I would also like to thank Debbie and all my lab mates at the µSonic lab, without whom this thesis would be significantly sadder. I am grateful for all their help during the pursuit of this work, from teaching me how to use the laboratory machines and modelling programs, to days spent working on a safe endoscope sheathing method, to securing a pig for the animal study, so much of this work would not have been possible without their support.

Finally, I would like to thank my family and friends for being a pillar of support during this time. Thanks for keeping me a functioning human with food, reminders to rest, and moral support.

CHAPTER 1 INTRODUCTION

Ultrasound is a highly valuable and versatile modality used in the medical sector that has both therapeutic and imaging capabilities. Originally used in sonar applications for underwater mapping and submarine detection in World War II, the current field of medical ultrasound imaging has grown to be an indispensable component of healthcare [1]. As a penetrative imaging modality, ultrasound benefits from ease of transportation, lack of radiation dangers, low cost, and real-time imaging [2]. Intraoperative ultrasound is also commonly used across a variety of operations for surgical guidance [2], [3].

As surgical techniques move to less invasive approaches, conventional ultrasound probes become unusable in these smaller pathways due to their large size. Despite the limited intra-surgical guidance from extracorporeal ultrasound, these minimally invasive approaches are quickly becoming the primary choice for many procedures due to decreased recovery times for the patient, less blood loss, and reduced trauma to the surrounding anatomy [4]. This has created an unmet need and incentivized the development of new visualization modalities and tools that are capable of high-resolution imaging in smaller surgical corridors at the required depth. Ultrasound imaging is a suitable visualization method for surgical guidance since it provides depth resolved real-time imaging with no harm to the patient. An example of this would be the development of intravascular ultrasound (IVUS) catheters for intra-arterial image guidance during minimally invasive cardiac procedures [5], [6]. Advancements in micro-fabrication technologies has enabled the development and success of these catheters, but they lack image quality due their array's geometry limitations (dimensions less than 1 mm) in comparison to conventional external ultrasound probes. In most minimally invasive procedures however, larger surgical corridors, on the order of a few millimeters, are used. It is hypothesized that ultrasound probes with higher image quality than IVUS catheters could be developed for these procedures through the utilization of several new micro-fabrication technologies.

New microfabrication technologies have not only allowed for the miniaturization of ultrasound probes, but also for probes operating at higher frequencies above 20 MHz.

High frequency ultrasound produces images with higher resolution than conventional ultrasound probes at the expense of 1) lower penetration depth and 2) challenges in fabrication (micron scale sensors) [7]. Although penetration depth is traded off for image resolution in a high frequency ultrasound probe, the approach of minimally invasive surgery allows the probe to be placed near the anatomy of interest, offsetting the penetration depth deficiency. An example can again be found in IVUS catheters, where high frequency ultrasound is used to scan the inside of suspected atherosclerotic vessels with high resolution, but with penetration of just a few millimetres [5], [6]. As mentioned, sacrifices in IVUS image quality are made due to the small size requirements, as it limits typical IVUS catheters to just a single sensor element in contrast to conventional ultrasound systems that use an array of many sensors. There are many surgical applications that would benefit from a transducer that uses sensor array technology (similar to conventional probes) for good image quality, high frequency (similar to IVUS) for high resolution, and a miniature endoscopic form factor of just a few millimeters.

Spine surgery is an area of surgery that has drastically shifted to minimally invasive approaches. One of the most common spine procedures is called “decompression” with the purpose of relieving a pinched nerve within the spinal canal. This pinched nervous structure could be the spinal cord, nerve roots, or nerve bundles that comprise the cauda equina. As an interventional measure, surgery is usually considered when more conservative treatments such as therapy and medication have failed to alleviate the patient’s symptoms [8], [9]. As open spine surgeries require a long recovery time for the patient, a longer hospital stay, and relatively high complication rates, there has been a push towards minimally invasive spine surgery (MISS) [10]. In comparison to open spine surgery where a >5 cm incision is required to access the relevant anatomy, a MISS requires a <2 cm incision for a retractor tube that is guided down to the region of interest [11], [12]. Obstructing bony material, typically a portion of the vertebral lamina, is removed by way of a burr drill, and the pathology is approached with thin, long-necked instruments for removal after temporarily moving the nervous anatomy to the side. After removal or reduction of the offending pathology, the nerves are then assessed for successful decompression by manual palpation with a round-tipped probe by the surgeon

[13]. This judgment is reliant on the surgeon's experience and is a subjective evaluation. Current reoperation rates of minimally invasive spine decompressions vary, with microendoscopic discectomies (MED) reaching reoperation rates as high as 5-16%, a significant number especially when considering that compression is one of the main causes for lumbar spine surgery [14]. As reoperations are costly to the patient and to the healthcare system, reducing this number would greatly ease the burden on both.

The work in this thesis introduces a novel high frequency, small form factor and angled ultrasound transducer that is capable of imaging within the spinal canal through a minimally invasive surgical pathway. It is hypothesized that decompression could be confirmed without manual manipulation of the spinal cord, potentially leading to a reduced rate of reoperation. Tat et al [15] have previously demonstrated that using low frequency intraoperative ultrasound between 3 MHz to 15 MHz during open spine surgeries can visualize a decompressed spinal cord qualitatively from a "free-floating" ventral aspect. This qualitative observation will likewise be possible with an ultrasound endoscope during minimally invasive versions of the same operation. It is also hypothesized that increasing the frequency (resolution) will be able to provide more quantitative measurements of decompression in future studies. High resolution micro-vessel Doppler may also be capable of providing visualization of fine blood flow within the spinal cord, enabling a new intra-surgical functional measurement that has never before been available to surgeons. The work presented in this thesis is an evolution of a previously developed high frequency ultrasound endoscope meant for minimally invasive surgeries, such as those meant for the brain [16]. The spine endoscope design is substantially different than the neuro endoscope and the design, fabrication, performance, and safety characterization are presented. Preliminary tissue imaging of spinal anatomy in a porcine animal model was used to qualitatively evaluate the ability to visualize spinal structures using an identical minimally invasive approach to that used clinically.

1.1 MOTIVATION

As the population ages, pathologies that occur as the human body ages have become more prevalent [17]. The human body deteriorates over time, and as the pillar keeping the

human upright, the spine is not exempt from this deterioration with age. Wear from use, loss of elasticity/cartilage, osteo arthritis, metastatic cancers and especially herniated discs may result in compression upon the nervous tissues within the spinal canal [18], [19]. This compression of the spinal cord, nerves, or roots may cause a menagerie of issues for the patient: ranging from lower back pain to sciatica, greatly decreasing the patient's quality of life [20]. It is estimated that up to 43% of the general population would suffer from sciatica over their lifetime, characterized by radiating leg pain or even motor and sensory deficits [21], and 60-80% overall will be affected by lumbar disc herniations over their lifetime [22]. Currently, over 1.2% of the population will have a spine surgery to relieve back pain in their lifetime making it one of the most prevalent surgeries [23]. Therefore, it is of utmost importance that these procedures inherently have low complication and revision rates. Real-time endoscopic intraoperative ultrasound image guidance could potentially become an essential tool for confirmation of nerve decompression as these surgeries move towards more minimally invasive approaches and fewer image guidance options are available.

Spine surgery has existed for thousands of years [24], although minimally invasive spine surgeries have only existed for the past 30 years or so [12]. Both open and minimally invasive surgery entail the surgeons opening a surgical corridor to the affected vertebral levels, removing some amount of bone and ligament to reach the spinal canal, and then operating within that confined space. While in open surgery visualization is easier with tools such as optical cameras, microscopes, and conventional ultrasound, the amount of tissue and bone removed in minimally invasive surgeries drastically restricts what visualization methods can be used. This is one of the main reasons why surgeons have had to substitute visual assessment with manual palpitation instead [13]. This method of assessing the freedom of the spinal cord is subjective to the operating surgeon and therefore may not demonstrate the necessary consistency or accuracy as required of surgical outcomes.

A clinical unmet need is an objective method for verifying the completion of the decompression surgery, both to prevent the potential need of a reoperation, and to prevent complications that may arise from the current method of assessing an unpinched nerve.

This could greatly improve the quality of life of numerous patients that may have required a reoperation, or have had to suffer complications during their surgery such as dural tears or other damages to the nerve roots [12]. Additionally, by providing surgeons with a tool that that can detect spinal cord micro-vessel blood flow with Doppler, it may also be possible to assess vascular pathways within the spinal cord during spinal cord repair surgeries. This may potentially provide information on narrowed vascular pathways, outline abnormal contours, and vascular conditions in the nearby surrounding regions. Finally, with the high resolution afforded by high frequency ultrasound, anatomical structures such as the dura mater, spinal cord, nerve roots and the thin, potentially sub-millimeter space of the subarachnoid layer of CSF may be more closely visualized for pathologies and irregularities, allowing surgeons to obtain a more complete patient specific diagnosis of the underlying pathologies.

1.2 HYPOTHESIS

It is hypothesized that an angled, high-resolution ultrasound endoscope, will be capable of visualizing spinal anatomy and confirming nerve decompression during minimally invasive spine surgery.

1.3 STRUCTURE OF THESIS

This thesis will be presented in a total of six chapters and this section will summarize the content of each of the 6 chapters.

This first chapter presented a rudimentary background before leading into the motivation behind this work. It also presented the central hypothesis and provides an outline of how this thesis is organized.

The second chapter will provide a comprehensive background for the thesis first by introducing the anatomy of the spine, the relevant pathology to this project, and comparative information on porcine and human spine structures. The chapter will then present the available therapeutic methods for the mentioned spinal pathologies and the progress leading to the current shift towards minimally invasive surgeries. The issue of

visualization within the narrow surgical corridors will be elaborated upon, as well as how ultrasound was previously explored as a surgical guidance method in open spine surgeries. The latter half of the chapter then delves into the technical aspects of ultrasound, from foundational principles to how ultrasound functions, types of transducers, how parameters for an ultrasound array are decided, and finally to the development of miniaturized high frequency imaging transducers.

Chapter 3 presents the methodology of this thesis. There are four segments to this chapter: the design of the ultrasound endoscope, the micro-fabrication processes developed, the methodology and reasoning behind the characterization tests, and the ex-vivo porcine imaging for proof of concept. This chapter presents the processes behind this project following its initial conception to the testing stages where both the probe's safety properties and attributes as an ultrasound imaging device are characterized. Then it will finish with how imaging was evaluated, both for superficial preliminary in-lab tests with volunteers from the lab and the conduct of the porcine spinal testing. Doppler was utilized in the in-lab tests but not with the porcine trials as it was an ex-vivo study and therefore would not detect blood flow.

Chapter 4 presents the results from the fabricated probes and the data collected from the imaging trials of this study. This includes characterization of the transducer array, safety testing, and tissue imaging. The array testing was comprised of probe characterization data such as the impedance magnitude and phase, the pulse echo bandwidth, sensitivity, resolution, insertion loss, and other relevant data. The safety testing data presents the results of acoustic testing for the mechanical and thermal indexes, and the radiative thermal properties. The imaging data presented in this chapter includes qualitative images of the human wrist in vivo and ex vivo porcine imaging of spinal anatomy.

Chapter 5 presents the discussion component of this work, with the subsections directly corresponding to the results presented in Chapter 4. This chapter as with an analysis of the array testing results, comparing the two probes that were tested, and the potential reason for any variations due to the fabrication process. The safety testing results are also analyzed alongside several issues and how results were interpreted. Finally, the obtained

tissue images from the endoscope will be analyzed for their diagnostic potential. A surgeon will also be consulted on the quality of the images, and they will be further assessed from the author's own perspective as a certified but non-practicing sonographer.

Chapter 6 presents the conclusion to this thesis, providing a brief summation of the previous sections and the implications of this work for future studies, such as how to translate the results of this study to patient trials.

CHAPTER 2 BACKGROUND

It is estimated that at least 80% of humans will experience back pain at some point in their lives, making it one of the top five causes for physician visits and attributing to billions of dollars of healthcare in the USA alone [23], [25]. Of this vast number, it is further estimated that although only 1.2% will receive surgery for the pain, this population accounts for almost 30% of back-pain related costs within the same 12-month period [23]. This is further emphasized as humans gain longer lifespans, allowing more time for painful degenerative diseases that impact the spine to occur [17], [26]. A common spinal operation is one that relieves the pressure on a pinched spinal nerve, which is frequently used in conjunction with fusion surgeries where neighboring weakened vertebrae are connected with bone, bone-like material, metal plates or screws to provide additional stability [27]. As medical technology evolves, patient outcomes and quality of life become a higher priority, surgical interventions are also moving towards smaller incisions, reduced patient trauma, and a faster return to normal life [28]. This has led to the establishment of MISS, where the operation is done entirely within the narrow surgical corridor of a retractor tube that allows access to the spinal canal [10]. While these types of surgeries are beneficial towards a patient's recovery by using a smaller surgical corridor, it also limits the surgeon's field of view, which may lead to a significant number of reoperations and complications.

During minimally invasive surgeries, optical-based imaging such as surgical microscopes abides by the limitations of light-based imaging. This renders them incapable of penetrating through opaque structures or sufficiently reflecting/refracting within the surgical corridor to provide adequate visualization of any sub-surface anatomy or optical blind spots. In comparison, ultrasound is constrained by 1) a trade-off between resolution and penetration depth [7] and 2) a trade off between size and image quality. However, because of the confined space within the spinal canal, penetration becomes less of a priority as compared to providing sufficient resolution to delineate fine structures such as the nerve roots, CSF, and spinal cord. With the ability of ultrasound probes to "steer" the ultrasound beam, it also becomes possible to image from alternate angles and obtain a much larger image window than the size of the transducer.

General clinical ultrasound probes typically have a large footprint on the centimeters scale making them too bulky to be used in minimally invasive surgeries. While useful for imaging during open surgeries, and for providing guidance during biopsies, these probes exist on a scale that renders them incapable of assisting in minimally invasive surgeries. Furthermore, ultrasound as a modality is unable to penetrate through bone, therefore making the spinal cord within the vertebrae inaccessible to ultrasound from the skin surface of the patient. The push for minimally invasive spine surgeries evolved alongside the technology that makes it viable, and even as microscopes, optical endoscopes and other imaging methods have allowed these surgeries to become a reality, these visualization methods may be insufficient within the smaller surgical corridors.

Ultrasound is defined as sound with frequency above the human hearing threshold of 20 kHz, and medical imaging ultrasound typically operates in the megahertz frequency range. Although literature varies on the exact definition, frequencies above 20 MHz are generally labeled as high frequency ultrasound [7], [29]–[31]. With the increase in frequency comes an increase in fabrication difficulty, as the operational frequency of the transducer is inversely related to the thickness of the active piezoelectric material, not to mention fabricating arrays of smaller and more fragile elements. Despite the difficulty of constructing high frequency ultrasound probes and the additional difficulty of miniaturizing them, they are of great benefit in the clinical environment by providing high resolution, real-time imaging within confined anatomy and with limited windows, such as the narrow corridors available for minimally invasive surgery.

2.1 THE SPINE

The human spine is an evolutionary marvel and one of the distinguishing features of a human's existence as a vertebrate animal. In total, the spine is composed of 33 vertebrae. As the human grows into adulthood, 5 of these bones fuse together to form the sacrum, and the last 4 fuse together to form the coccyx. In normal anatomy, the remaining 24 vertebrae retain some freedom of movement between neighboring vertebrae and share considerably more similarities in morphology than the 9 that eventually comprise the sacrum and coccyx.

Throughout the length of the spine runs the spinal canal. Within this spinal canal resides the spinal cord, a highway of nerve fibers that travels from the base of the brain down towards the rest of the body, with branches called nerve roots leaving the canal at every vertebral junction through a foramen and with the cord separating into multiple nerve bundles at the lumbar level. These separated nerve fibers are known as the cauda equina. In this thesis, both the spinal cord and the cauda equina will be grouped under the term the “spinal cord”.

Of the many pathologies that may plague the spine, from birth defects to acquired pathologies, a pinched spinal nerve due to degeneration of the spine is one of the most common pathologies that would require surgery. These pinched or compressed nerves may be caused by an extrusion of soft tissue such as pulposus disc materials, tumours, a thickened ligamentum flavum, or overgrowth of bony tissue. The two most common of those causes would be the herniated disc, commonly known as a slipped disc, and bony overgrowth, which is known as a spinal stenosis. However, it is important to note that the term spinal stenosis is also used to describe an overall narrowing of the spinal canal, which may have resulted from any of the previously mentioned conditions. It is possible for some of these pathologies to recover passively over time or with non-surgical therapies such as medication and physical therapy, but when non-surgical methods have demonstrated to be insufficient, the patients would typically require surgery.

2.1.1 SPINE ANATOMY

Human spines are composed of multiple interlocking vertebrae, and while the 24 vertebrae that form the cervical, thoracic, and lumbar spine all share multiple morphological similarities, each region has their own distinct structural characteristics. There are 7 cervical vertebrae, starting at the base of the skull to C7, and 12 thoracic vertebrae, each one associated with a pair of ribs. The last 5 individual mobile vertebrae are those in the lumbar region and are the largest vertebrae in the human spine. Each of the vertebrae from these three regions consist of a vertebral body, a complete arch off the posterior aspect of the body and some number of processes that branch off the vertebral arch. The spinous process is present on all the vertebrae except for C1, and it is the

posterior process that can typically be felt through the skin on the back. The spinal cord runs through the continuous tube formed between the vertebral body and arch within the space known as the spinal canal. Together with the attached musculature, ligaments, tendons and other associated tissues, this entire structure is known as the vertebral column. Figure 2.1 provides a visualization of the general vertebrae anatomy from the cervical, thoracic, and lumbar regions.

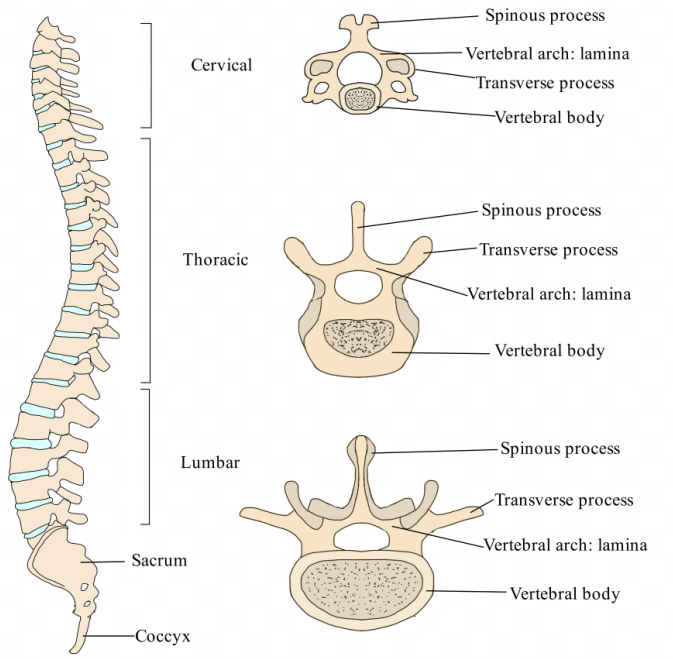

Figure 2.1 Depictions of vertebrae from the cervical, thoracic, and lumbar spine labelled with the vertebral bodies, laminae, transverse processes, and spinous processes.

The three vertebral regions relevant to this work are the cervical, thoracic, and lumbar regions. As shown in Figure 2.1, while the vertebral arch encompasses the entire posterior structure of each vertebra including its pedicles, processes, and facets, specific terminology has also been devised to better describe the different portions of the arch. The stretch of bone between the spinous process and the transverse processes is known as the lamina and is the target of laminectomies or laminotomies. This is also the stretch of bone that is drilled through during minimally invasive spine surgeries conducted through

a posterior approach. The pedicle is the bony material between the transverse process and the vertebral body, forming part of the spinal canal's lateral wall.

While the facets between neighboring vertebrae permits movement and articulation of the joints, the structure that physically connects the two vertebral bodies together is the intervertebral disc. The intervertebral disc is composed of two parts: an external, fibrous ring named the annulus fibrosus, and an internal, pulpous component known as the nucleus pulposus. It is estimated that a quarter to a third of the spine's height is due to the intervertebral discs, and the gradual shrinking height as an individual ages is due to their degeneration [19], [32]. These discs are likewise responsible for load cushioning. Where the external fibrous annulus is more concerned with tensile stresses on the spine, the internal nucleus pulposus is more associated with compressive forces. It is important to note that the blood supply to the intervertebral discs dwindle as the individual ages. While there is a rich supply of blood to the peripheral of the fibrous annulus throughout life, the internal aspect of the outer ring loses its supply of arterial blood after reaching adulthood, and the internal nucleus pulposus does not receive blood flow at all. As a secondary cartilaginous joint [32], these discs also degenerate far earlier than similar joints in the body, with degenerative changes occurring in those as young as teenagers and up to 60% of 70-year-olds living with severely degenerated discs [19]. Disc degeneration can also directly cause compression of the spinal cord.

The spinal canal is the continuous passageway within the vertebrae and houses the spinal cord, the proximal portions of nerve roots, and the nerve bundles that comprise the cauda equina. The spinal cord branches off from the brain stem and terminates at approximately the L1 level of the spine as the conus medulla, a cone-like structure tapering in the direction of the base of the spine. The average diameter of the spinal cord varies greatly between levels of the vertebrae, from the minimal anteroposterior diameter of approximately 6.1 mm to the maximal transverse diameter of 15.5 mm [33], with additional inconsistencies due to the patient's body habitus. From the conus medulla onwards the nerves exist as nerve bundles, collectively termed the cauda equina. As the spinal cord is a structure that is continuous with the brain, it is similarly covered by the three layers of meninges. The layer that is flush with the spinal cord is the pia mater, and

the space between that and the arachnoid mater is the subarachnoid space that contains a cushioning layer of cerebrospinal fluid (CSF) and the nerve roots. The dura mater exists as the outermost layer, and is typically adhered to the arachnoid layer, with a potential subdural space between. The remainder of the spinal canal is filled with epidural fat with minor vasculature.

The primary vasculature feeding the neural structures are the anterior and posterior spinal arteries, although they are supplemented by multiple smaller arteries and are covered by the pia mater. These vessels primarily arise from the vertebral arteries, with the supplementary branches entering the spinal canal from the intervertebral foramen. The ligamentum flavum lies against the posterior wall of the spinal canal, connecting the vertebrae as a single continuous structure both for support and as an additional cushion between the spinal cord and canal. Figure 2.2 below depicts the internal structure of a vertebra with the spinal cord.

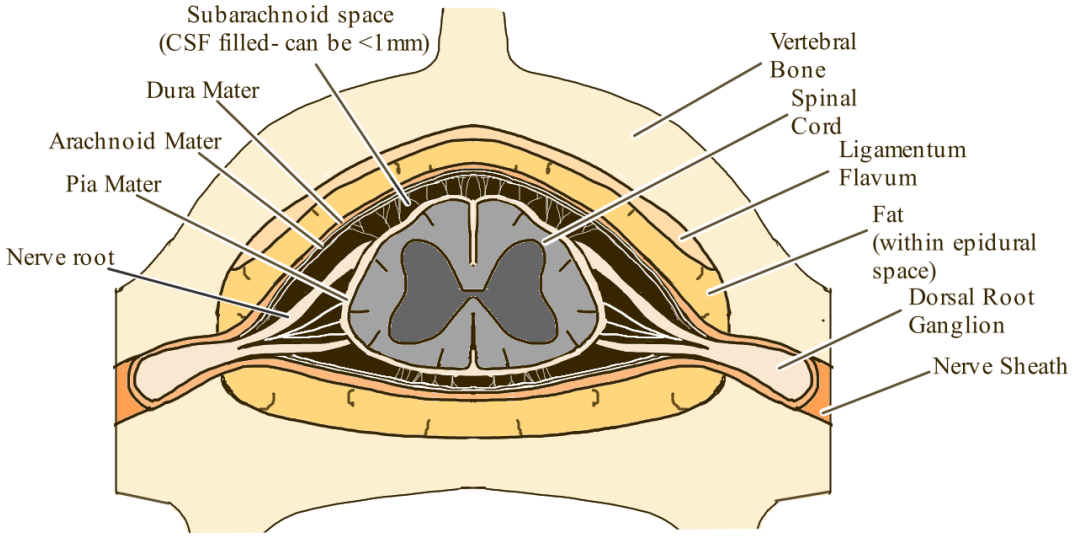

Figure 2.2 Transverse visualization of the internal anatomy of the spinal canal.

2.1.2 SPINAL CORD COMPRESSION

There are many potential ailments that can befall the spine. Congenital malformations include scoliosis and kyphosis, while acquired pathologies include herniated discs and

bone spurs. Of the many pathologies that can be treated using MISS, this work will be examining those that result in spinal cord compression. Compression can be defined as the pathological process where an abnormality results in the spinal cord or offshoot nerves becoming trapped or pinched within the spinal canal.

Spinal cord compressions may result from a variety of pathologies. As the name implies, it is typically a pathology that occurs within the spinal canal and involves the compression of the spinal cord, spinal nerve roots, or the foramina where nerve roots enter and exit the canal, as those openings may narrow and cause a pinching of the nerve. Since spinal cord compressions directly impact the nervous structures, the possible symptoms can vary greatly in type and intensity depending on the level of occurrence and the severity of the compression. Patients may appear asymptomatic, or have symptoms ranging from tingling in the lower limbs to pain and neural claudication [27]. This is commonly seen as sciatica, cauda equina syndrome and back pain [21], [34]. Due to the large range of symptom presentations, the patient may choose to pursue different avenues of treatment to suit their needs and available resources.

While possible at all ages, the odds of a spinal cord compression are greatly increased as the person ages and the spine deteriorates. Two of the most common causes for spinal cord compressions are herniated discs, where at least 9% of the general population will experience one in their lifetime, and spinal stenosis, at over 11% [35], [36]. While spinal stenosis is more generally used to describe the narrowing of the spinal canal due to bone, it may also be a generalization and encompasses a narrowing of the canal due to pathologies such as herniated discs, tumours, or a thickened ligamentum flavum. In the body of this work, a spinal stenosis will refer to the narrowing due to a bony outgrowth. Aside from herniated discs and spinal stenosis, two other potential causes of spinal cord compression that will be encompassed within this work are spinal tumours and a thickened ligamentum flavum.

Herniated Disc: A herniated disc is one of the most common causes of spinal cord compressions and occurs predominantly in the lumbar spine. Therefore, instead of compressing the spinal cord, it is more likely to compress the nerve bundles that

comprise the cauda equina. It is a pathology where the incidence increases with age due to the deterioration, and eventual tear of the annulus fibrosus, and as such is a pathology that is becoming more prominent in this aging society. This tear may occur because of the fibers losing elasticity, trauma to the region, or other forms of degradation, allowing the nucleus pulposus to herniate out into the spinal canal as illustrated in Figure 2.3. The amount of nucleus pulposus that herniates out from the intervertebral space varies, with this variation being the difference between asymptomatic presentation to paralysis, and acute pain in the lower limbs [9]. Treatment for herniated discs depends on symptom severity and extent of herniation, and physical therapy, time, and medications are all possible non-surgical treatments that can either reduce the symptoms or the extent of compression. However, non-surgical treatments and passive observation may not be sufficient. In the US alone, at least 300 000 surgeries are performed for herniated discs on an annual basis [37]. This can be done through open surgery or minimally invasive surgery, where open surgery typically utilizes muscle retractors and a longer incision to approach the site of interest while minimally invasive method use a smaller incision and either tubular retractors or endoscopes for access. Even as microdiscectomies are still considered the gold standard surgical option for lumbar disc herniations [38], tubular spinal decompressions have become the operation of choice for not just lumbar disc herniations, but for lumbar spinal stenosis as well [39].

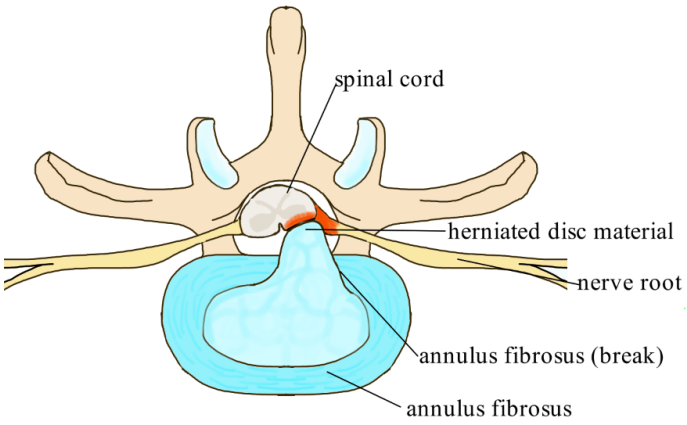

Figure 2.3 Transverse section of a vertebrae depicting herniated disc material compressing the spinal cord within the spinal canal.

Spinal Stenosis: The other common cause of spinal nerve compression is spinal stenosis, where the extrusion of a bone spur into the spinal canal or foramen pinches the spinal cord or nerve roots. While this may also be more prominent in the lumbar spine in a manner similar to herniated discs, spinal stenosis may also occur frequently in the cervical region [40]. It is estimated that within populations of ages 65 and above, spinal stenosis is currently one of the most common and fastest growing reasons that spinal surgery is requested [41], [42]. Causes of spinal stenosis range from arthritis to other bony degenerative diseases and trauma. An example of a bony spur (an osteophyte) protruding from the posterior wall of the vertebral body of a lumbar vertebra is depicted below in Figure 2.4 [43]. Surgical intervention is often required to remove this obstruction in the surgical canal. The area of interest is approached using either minimally invasive or open surgery methods, and the excess bony material is removed to free up the compressed nerve. It is also possible that a laminectomy will be considered, where the lamina of the vertebra is either reduced or removed to relieve the compression. It is common for these surgeries to be used in conjunction with spinal fusions to maintain integrity and stability after the removal of a significant amount of bone. The benefit of using minimally invasive approaches in this intervention as opposed to open surgery lies in the reduced hospital stay, reduced pain and less disruption to back musculature, but it suffers from having a greatly reduced field of visualization and a significantly smaller working corridor.

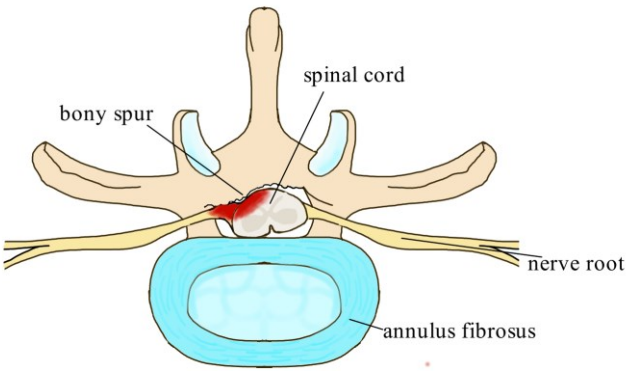

Figure 2.4 A transverse section of a vertebrae illustrating the bony spur protruding into vertebral canal causing compression of the spinal cord and nerve root.

While bone growths and canal narrowing are the most common causes for stenosis, spinal tumours [44] and a hypertrophied ligamentum flavum [45] are also possible. Spinal

tumours can occur either as primary tumours or as metastases, where metastases are far more common. While primary intraspinal tumours occur at an incidence of 1.5 occurrences in every 100 000 person-years [46], it has been estimated that approximately 50% of skeletal metastases occur in the spine [47], [48]. As such, an estimated range of 5-10% of all cancer patients may demonstrate compression from metastatic tumours, and treatment may be palliative instead of curative for patients anticipated to have short or mid-term life expectancy remaining [48]. Under these circumstances, the surgery may aim to primarily restore the patient's quality of life for what time they have remaining [18], [47]. Tumours in the spinal canal can develop within the bony tissue, within the spinal cord itself, as part of the meninges, or within the canal from some other anatomy. A spinal tumour occurring in the vertebral body is depicted below in Figure 2.5, where the presence of the mass compresses the spinal cord. When surgery is chosen in these situations, they are conducted with the goal of removing as much tumour tissue as possible, a task that is made more difficult by the lack of penetrative imaging during surgery. Even then, there is a trend towards minimally invasive methods of excising metastatic spinal tumours in comparison to open surgeries [49]. This is supported by a variety of literature stating that while clinical outcomes remain the same, minimally invasive techniques have established decreased blood loss, decreased complication rates, decreased postoperative drainage and shorter length of bed rest [42].

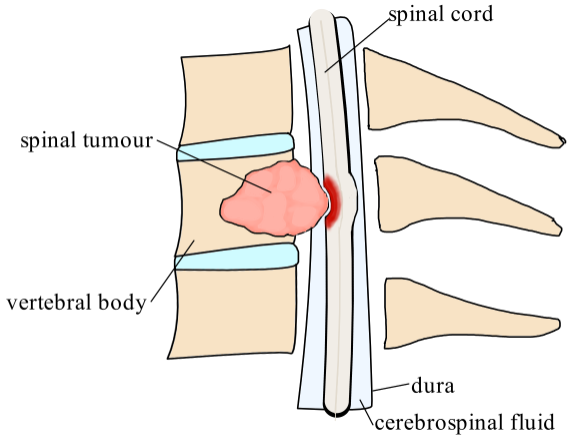

Figure 2.5 Spinal tumour impinging upon the spinal cord.

In contrast, ligamentum flavum hypertrophy may occur due to aging, stress, or changes within the cellular matrix [45]. When inflammation is reduced with medications or other non-invasive therapeutic methods it is possible to conservatively reduce the compression. However, should surgery be required, it will be conducted in much the same manner as a microdiscectomy or microlaminectomy: a narrow surgical corridor will be opened to expose the region of interest and the thickened ligament will be reduced to alleviate the pressure on the nerves.

Due to the wide spectrum of potential symptoms and pathological processes, it follows that there is a spectrum of therapeutic methods for managing spinal cord compressions. From watching and preventative measures for asymptomatic presentations, to surgical interventions for the severe symptoms, health care providers and patients collaborate to devise a treatment plan that works best for the patient. Even within surgeries, there exists multiple methods of treating spinal cord compressions depending on the patient's body habitus, type of compression, level of compression, and surgical complexity. This may change the type of surgery, which may be a minimally invasive surgery or an open surgery. Minimally invasive surgeries can further be separated into a tubular vs an endoscopic approach, and a fusion surgery may be required alongside the decompression [11].

2.2 SPINAL DECOMPRESSION SURGERY

Evidence of a spine surgery was recently found in an Egyptian mummy, demonstrating that it has been an evolving practice for over five thousand years. The first documented operative spinal surgery was performed by Paulus of Aegina in the 7th century [24]. As knowledge of anatomy advanced alongside the development of technology for use in medicine, surgeries became more sophisticated, safer, and protocols were developed to better a patient’s quality of life. This continues to hold true as surgeries move to more minimally invasive approaches. The standardization of technique and equipment now allow surgeons to perform outpatient spine surgeries that require only a single stitch for procedures that originally required days of bed rest and weeks of wound healing. However, while minimally invasive spine surgeries come with a plethora of benefits,

there are also drawbacks due to the small surgical channel that the surgeon would be required to operate within. The long and narrow surgical corridor limits the size and shape of the tools, and the diameter of visualization is limited to approximately 15 mm. As a result, of the many minimally invasive surgeries conducted on an annual basis, a significant number result in complications, are incomplete, or require reoperations. This can be extremely costly to the patient and to the health care system and could potentially be avoided with better intra-surgical visualization.

2.2.1 SURGICAL HISTORY AND PROCEDURE

The goal of a spinal operation is to restore patient function and improve their quality of life, regardless of whether it is done through open or minimally invasive methods. There are multiple factors impacting the choice on whether an open surgery or a minimally invasive approach will be preferred, such as the surgical team's training, patient body habitus, complexity of the surgery, available equipment, and confidence of visualization, although at least 75% of current spine surgeries in the US are performed through minimally invasive means and the number has only continued to grow [50].

As compared to the multiple approaches that may be taken with minimally invasive spine decompressions, there is less variation when conducting open spine surgeries. The procedure is preceded by imaging, which is either conducted through an X-ray or MRI to plan the location and size of the incision. The factors determining the location and incision length are the number of vertebrae that require this intervention, the complexity of the operation, and if spinal fusion will be required [51]. This operation is done under general anesthesia, and a 5-15 cm long sagittal incision is made along the midline of the patient's back. The underlying fascia and muscle layers are carefully parted and held in place to expose the vertebrae while another radiograph is taken to localize the vertebral level. Any additional soft tissue above the vertebrae is removed or moved aside, and a laminectomy or laminotomy is performed to access the spinal canal or reduce spinal stenosis [52]. In this manner, the surgeons can easily reach down and manipulate the area as needed due to the large incision and parted anatomy, with more degrees of freedom offered for the tools. In operations where the amount of removed bone may result in

spinal instability, the surgeons will also proceed onwards with an additional spinal fusion [27]. Once the affected nerve has been decompressed, the muscles are released back into place and the layers of fascia and skin are stitched back together. During this type of open spine surgery, the incision and laminectomy provides a sufficient window for a general ultrasound probe. Intraoperative ultrasound for open spine surgeries have been documented since the 1980s, and it is one of the few modalities that provides the surgeon with continuous real-time imaging of the region of interest, as well as surrounding soft tissue and bone surface visualization [15]. The use of ultrasound in surgery will be further elaborated upon in 2.3.4 ULTRASOUND IMAGING IN SURGERIES.

Minimally invasive spine surgeries (MISS) are similar to open surgeries in that preoperative imaging is done through MRI or X-ray. There are two categories of MISS: those done with a retractor tube system, and those conducted with a full endoscopic approach. The microdiscectomy approach was first described in 1977 as an alternative to the open lumbar disc herniation surgery where a surgical microscope was introduced to the operation as a microsurgical operation [13], [53], [54], while the minimally invasive methods employing retractor tubes was more recently conceived and put into practice in 1993 and full endoscopic discectomies (FED) with supported video feed was introduced in 1997 [12]. The tubular retractor approach is illustrated below in Figure 2.6, where a retractor tube is used in conjunction with a surgical microscope when accessing the spinal canal.

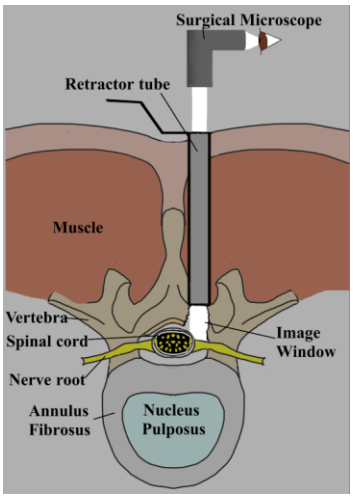

Figure 2.6 Visualization window of a tubular retractor using a surgical microscope.

Minimally invasive decompression spine surgeries can be conducted through a few different approaches depending on the patient's anatomy and the location of compression. Localizing the region of the incision requires more guidance with the minimally invasive surgery, which typically begins with palpating for the relevant vertebrae, opening an incision, and passing a guidance wire through the muscle layers. Intraoperative fluoroscopy X-rays are used to confirm placement of the wire. After the guidance wire is confirmed to be in position, a series of retractor tubes are passed down along the wire, widening the corridor with each successive retractor tube, until the final retractor tube is settled in place and anchored. As needed, the surgeon may use the first dilator tube to palpate for anatomical landmarks before proceeding with the remainder of the dilators [13]. The internal diameter of this working surgical corridor varies on the surgical instruments, but typically ranges between 16 – 20 mm [39]. Once the retractor tube is in place and positioned above the lamina, a portion of the bone is carefully excised with a motorized high-speed burr. The ligamentum flavum within the visualization field is also carefully excised with a Kerrison punch, exposing the spinal nerves [13]. The cause of compression is then removed. This minimally invasive tubular retractor approach has proven to be advantageous in preserving the joint facets, minimizing damage to surrounding soft tissue anatomy to preserve spinal stability, and preserving the spinous process [39].

2.2.2 VISUALIZATION METHODS DURING MINIMALLY INVASIVE SURGERY

To ensure the success of a MISS, multiple imaging methods are used both before and during the procedure, with the primary visualization method differing between types of MISS. For microdiscectomy decompressions using retractor tubes, visualization is typically performed with a surgical microscope or microscope loupes. Endoscopic spinal discectomies without retractor tubes are often conducted with a variety of tailored optical endoscopes for surgical guidance [11]. Before these surgeries, the patient will likely have undergone MRI imaging to localize the region and extent of the compression. By performing preoperative imaging, it allows the surgical team to localize the site of interest, plan the surgical approach and convey the plan to the patient. The possible

approaches to conducting this surgery are transforaminal, interlaminar, anterior, posterior, and caudal, although it has been shown that extreme lateral approaches are also feasible with the endoscopic approach [11], [55]. Most of these approaches can also be applied to the different levels of the vertebrae, although some would be contraindicated by the anatomical details of that level.

After pre-operative planning, the operation begins with X-ray fluoroscopy imaging in conjunction with manual palpation to accurately localize the site of the muscle retractor after positioning the patient. X-ray imaging, while beneficial for observing skeletal anatomy and many surgical instruments, is less capable of visualizing the soft tissues and internal anatomy of the spinal canal and is thus less useful during the surgery itself. It is also an imaging method that utilizes radiation and is therefore best used as minimally as possible. Within the surgical channel, visualization is typically achieved through a surgical microscope, which has the benefit of allowing multiple individuals on the surgeon team to see within the surgical corridor simultaneously without worry of obstructing somebody else's view [13]. These optical surgical microscopes are limited by direct line of sight and can not see past corners or opaque anatomy. This limits visualization when the optical field is obscured by blood and soft tissues such as the dura, spinal cord, nerves, fat, and muscle, all of which can obscure the ventral aspect of anatomical structures as evidenced by the circled regions in Figure 2.7.

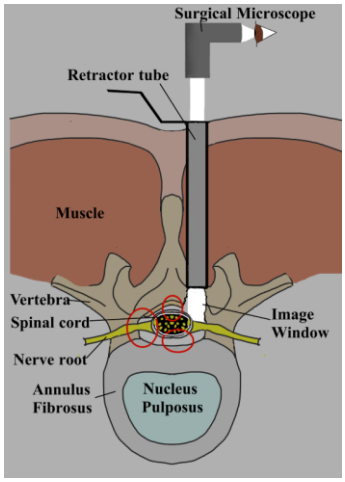

Figure 2.7 The blind spots (circled in red) that are present when using a surgical microscope down a tubular retractor.

Ultrasound has been previously used in spinal decompression surgeries and has been demonstrated to be capable of visualizing relevant anatomy [15]. However, it could only be used in conjunction with open laminectomies due to the footprint size of the clinical transducer. The transducer was contained within a sheath for sterility, with the open cavity filled with saline to provide a coupling agent for the transducer. The findings of those operations demonstrated that spine anatomy was well visualized using intraoperative ultrasound (IOUS) and aided in guiding the surgeries. Therefore, there is justification for pursuing the development of a miniature endoscopic ultrasound probe tailored towards MISS [56].

2.2.3 COMPLICATIONS AND CLINICAL NEED

For all that advancements in medicine and techniques have greatly improved patient prognosis in all fields, it is near inevitable that complications and reoperations will occur in some proportion of the patients undergoing the operation. In spinal decompression surgeries aiming to alleviate the symptoms and give the patient a better quality of life, this may present as a retention of symptoms, complications arising from the surgery, or the need for a reoperation due to an incomplete decompression.

A systematic review conducted on lumbar surgical techniques for discectomies reported a range of values for the multiple possible surgical variations. The authors had analyzed data from open discectomies, microdiscectomies, MEDs and FEDs. They had defined microdiscectomies as those that required a microscope, MEDs as the minimally invasive surgical method that utilized retractor tubes, surgical microscopes or surgical loupes, and FEDs as the minimally invasive surgery conducted completely through endoscopic means. Within contributing studies, they demonstrated that MEDs had a complication rate of approximately 4.4% for intraoperative dural injuries, 0.8% for nerve root injuries, 4.5% for neurological complications, and 1.2% for wound complications [12]. MEDs also demonstrated a reoperation rate of 4.9% within this review. Compared to the other surgical methods that had data provided, MED ranked lowest among wound complications but had a middling to high rate for the remainder types of complications. While the overall complication rate for discectomies was low across the multiple

methods, the variation in complications demonstrated how different methods may be better tailored for different surgical plans, with the additional presence of a steeper learning curve for the minimally invasive methods resulting in higher complication rates at the beginning of a surgeon's career [12]. This is further evidenced by the decrease in peri-complication rates for micro-tubular decompressions over the span of the ten years in which Patel et al. [39] conducted their study, from an estimated initial rate of 29.8% to an 8.78%.

In comparison, decompression for lumbar spinal stenosis is commonly investigated together with fusion, and a study conducted to investigate the long-term reoperation rates found that minimally invasive methods consistently demonstrated a lower reoperation rate compared to open surgery, with the former at 19% and the latter at 26.9% [26]. This held true for the inclusion of fusion, as the addition of fusion as a minimally invasive procedure had a revision rate of 11.1% and 29.2% for open surgery [26]. While it is shown that complication rates of minimally invasive methods are fewer when in comparison to their open surgery counterpart [48], it is necessary to keep in mind that these complications remain a burden for the patient and health care system alike. Over 1 million minimally invasive surgeries are performed annually in the United States alone, which means that between 100 and 150 thousand revision surgeries result (typically from incomplete decompression) [50]. High resolution intraoperative visualization of the compressed nerve along with confirmation of decompression could lessen the number of revision surgeries and represent a significant technological advancement in the field. In addition, if better minimally invasive intra surgical imaging technology was available to spine surgeons, it is hypothesized that a greater percentage of open surgeries could be considered for a minimally invasive approach. This would again benefit patient recovery and lessen the burden on the health care system.

2.2.4 THE PORCINE SPINE AS A MINIMALLY INVASIVE MODEL

It is important to train surgeons on models prior to performing surgeries on actual patients, and as such it is imperative to acquire a model that is sufficiently similar. While it is possible to acquire artificial models such as the synthetic spine model RealSpine by

Realists Training Technologies (GmbH, Leipzig, Germany) [57] or foam models [58], they have several drawbacks. The artificial models can be costly, fail to mimic the potential variations in anatomy, or incorrectly provide tactile feedback for the trainees. Within the potential animal models that would be of a comparable size to a human spine, contenders were the calf, pig, dog, deer, sheep and baboon spines [59]. While baboons share the trait of likewise being bipedal and upright posture, they are difficult and costly to acquire, as well as being not available in the same quantities as spines from common farm animals. Likewise, human cadaver spines are also difficult and costly to acquire.

Within the smaller subset of available spines, comparative studies have shown that pig spines share the most similarities to human spine morphology. While there remains unavoidable anatomical differences such as the anterior transverse processes present on certain porcine vertebrae that humans lack [59] or the difference in variability between the vertebrae of each section [57], the differences are within tolerable bounds. Additionally, the size of the pig may also impact the fidelity of the comparison to the human spine as it will affect the length of the spine, and in older pigs, the potential of variable degenerative changes [57]. To best model a human spinal canal that still contains cerebrospinal fluid, the porcine specimen would either need to be still alive or euthanized within the last twelve hours without any damage to the spine or other neural structures. Regardless, multiple studies have presented pig spines as an adequate substitute for human spines when considering neural structure, vertebral structure, and for use as a training model in minimally invasive surgeries [57], [60], [61].

2.3 ULTRASOUND IMAGING

Ultrasound is defined as sound above the typical human hearing range of 20 Hz ~ 20 kHz [1]. As this implies, ultrasound occurs outside of human perception and thus a variety of instruments are used to measure and characterize ultrasonic signals. In addition, even though ultrasound is defined as frequencies of sound over 20 000 Hz, typical medical ultrasound operates in the megahertz range, with general operating transducers using frequencies ranging between 2 MHz to 18 MHz depending on the anatomy of interest to balance the requirements of imaging depth and resolution [1], [7].

As a medical imaging modality, ultrasound holds numerous advantages but also suffers from some drawbacks. Clinical ultrasound does not use ionizing radiation, is inexpensive, real-time, and portable. Further proof of the safety of clinical ultrasound is demonstrated by how it is allowed to be used for fetal scans. In general, ultrasound imaging can be used to provide diagnostic images for almost every major organ, evaluate abnormalities such as those found in vessels, soft tissue masses, and provide complimentary information to CT or MRI scans.

However, ultrasound has certain drawbacks as well. Ultrasound imaging is highly reliant on the operator's capabilities, as it is possible for sonographers to make up false-positives on a scan or miss abnormalities. It is also dependent on patient body habitus, as one of the drawbacks of maintaining a certain amount of resolution is a limited depth, which may not be capable of producing enough penetration in patients with a larger body habitus. Ultrasound is also incapable of imaging through bone or through gas, as they reflect nearly all the acoustic energy at the tissue-bone or tissue-gas interface.

2.3.1 ULTRASOUND PRINCIPLES

As an imaging modality, ultrasound works by drawing upon the pulse-echo principle as depicted in Figure 2.8, where (a) an electrical pulse is transmitted down the coaxial cable towards the transducer, (b-c) the active material within the transducer vibrates, creating acoustic waves, (d-e) the sound wave encounters an object and is reflected back, (f-g) the reflected echo is converted from vibrations to electrical signals by the transducer which is returned through the coaxial cable. While simple in theory, there are many factors that must be considered for the technique to be capable of producing a high-quality image. For example, all high-quality imaging transducers consist of a large array of transmitter-receiver elements that are used to electronically steer and focus the ultrasound beam. Of the several key concepts crucial to understanding the process of ultrasound transduction, the most important are described below.

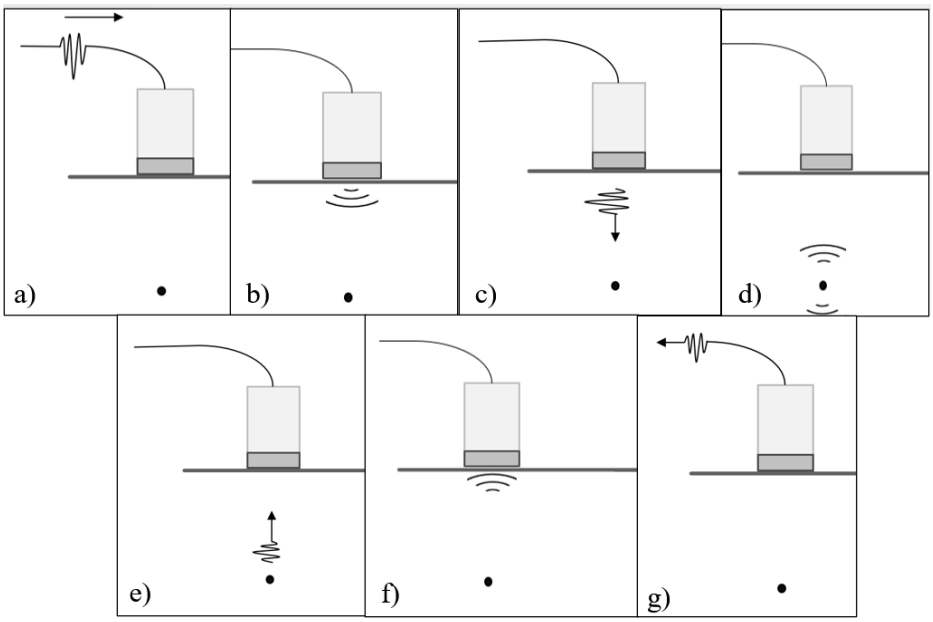

Figure 2.8 The pulse-echo technique (a) an electrical pulse is transmitted down the coaxial cable towards the transducer, (b-c) the active material within the transducer vibrates, creating sound waves, (d-e) the sound wave encounters an object and is reflected back, (f-g) the reflected echo is converted from vibrations to electrical signals by the transducer which is returned through the coaxial cable

Acoustic impedance (Z_o): is a mechanical property intrinsic to a material. Any boundary that has a mismatch of acoustic impedance across the boundary will result in a reflection for any propagating wave [62]. It uses the units Rayleigh (rayls or Rayls), which is equivalent to $kg \times s^{-1}m^{-2}$. The formula used to calculate acoustic impedance is Equation 2.1 where Z_o is the acoustic impedance in MRayls, ρ_o is the density of the material in kg/m^3, and c_o is the speed of sound within that material in m/s.

$$Z_o = \rho_o c_o \tag{2.1}$$

Acoustic transmission and reflection: During the pulse-echo process, the ratio of reflected (R_p) and transmitted (T_p) pressures at a boundary is determined by the acoustic impedance and the incident (θ_i) and transmit (θ_t) angle, where the larger the mismatch between the two materials, the more of the acoustic pressure is reflected. An example would be the boundary between muscle tissue and bone, where the sound waves after traveling through the muscle tissue will almost all reflect at the muscle-bone boundary.

The ratio at which the acoustic pressure is transmitted or reflected is governed per Equation 2.2 and 2.3 respectively.

$$T_p = \frac{2Z_{o2}\cos(\theta_i)}{Z_{o2}\cos(\theta_i)+Z_{o1}\cos(\theta_t)} = \frac{p_t}{p_i} \tag{2.2}$$

$$R_p = \frac{Z_{o2}\cos(\theta_i)-Z_{o1}\cos(\theta_t)}{Z_{o2}\cos(\theta_i)+Z_{o1}\cos(\theta_t)} = \frac{p_r}{pi} \tag{2.3}$$

With each received pulse, the transducer will transform the sound energy back into electrical signals, and a point is mapped on the display based on the time of flight of the pulse as well as the returning intensity.

Attenuation in ultrasound is the reduction of sound strength as it travels through tissue. In the realm of ultrasound imaging, this occurs mainly due to absorption and scattering. Absorption occurs as sound energy is absorbed by the tissue as thermal energy, and scattering occurs when irregular reflectors within the tissue medium reflects the sound away from the transducer. The frequency of the ultrasound is also a key factor in attenuation where higher frequencies correspond to a higher the attenuation coefficient. In clinical use, this is seen as a trade-off between frequency and depth of effective scanning, or resolution and scanning depth. Within a consistent medium, Equation 2.4 is used to approximate the remaining intensity after attenuation, where x is the distance in cm, $\bar{I}(0)$ is the original intensity, and α is the attenuation coefficient. The attenuation coefficient is calculated with Equation 2.5 and involves the ultrasound frequency f, where both a_0 and n are dependent on the material properties and the temperature of the medium [63].

$$\bar{I}(x) = \bar{I}(0) \cdot e^{-2\alpha x} \tag{2.4}$$

$$\alpha = \alpha_o f^n \tag{2.5}$$

Ultrasound machines implement time-gain compensation to offset depth-dependent attenuation to an extent. By amplifying signals received based on their received timing, it is possible to produce higher amplitudes, and thus brighter echoes within the image. However, this technique is limited by the noise floor of the ultrasound system as it will amplify the received noise alongside the signal, and once the signal is too weak to be

distinguished from the noise, it will not be possible to produce an enhanced signal regardless of the time-gain compensation.

Acoustic matching: There is a large acoustic impedance mismatch between the active piezoelectric material and the coupled human tissue, which results in a significant amount of energy being reflected at the element/tissue boundary as shown with Equation 2.3. This loss of sound energy at the boundary greatly reduces the sensitivity of the ultrasound transducer as insufficient signal would make it into the human body or back to the transducer. However, more of the signal would be able to transmit across the boundary when a matching layer is applied to act as a bridge as shown in Figure 2.9.

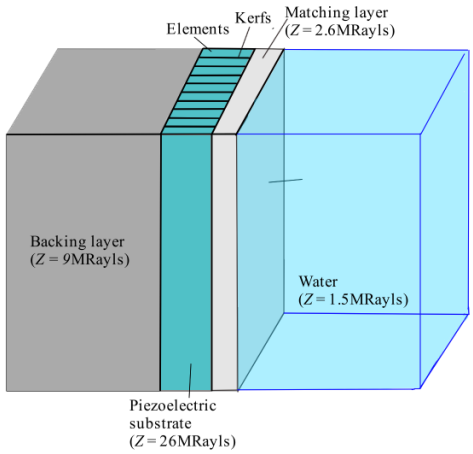

Figure 2.9 Illustration of the layers of a transducer coupled to water, including the piezoelectric substrate, the backing layer, the matching layer, and the water with example acoustic impedances.

There are three factors to consider when deciding on the matching layer: the number of desired layers, the acoustic impedance of the layers, and each layer's thickness. Despite the potential benefits of using multiple matching layers for better sensitivity and bandwidth, there is also a diminishing return and increase in fabrication difficulty with the number of increasing layers. As such, one or two layers are generally sufficient for most purposes. The work presented in this thesis will use a single matching layer.

When calculating for a single matching layer's desired acoustic impedance, Equation 2.6 can be used [62], [63]:

$$Z_{o2} = \sqrt[3]{Z_{o1}Z_{o3}^2} \quad (2.6)$$

Where Z_{o2} is the acoustic impedance of the matching layer, Z_{o1} is the acoustic impedance of the piezoelectric material, and Z_{o3} is the acoustic impedance of water or tissue.

Comparatively, the thickness of the matching layer is much simpler to calculate, as the optimal thickness is ¼ the wavelength of sound traveling within the material. This thickness enables constructive interference to occur at the probe face due to the phase changes that occur within the material when reflecting off the front face and then the back face before exiting into tissue, preserving a significant amount of signal.

2.3.2 TRANSDUCERS

A transducer is a device that transforms one form of energy into another. In ultrasound transducers, it converts electrical energy to acoustic energy and vice versa. While there are many types of ultrasound transducers, they can be broadly categorized by how they achieve imaging. This is further emphasized with the potential of send and receive beamforming with certain types of arrays, allowing for electrical focus and a sweeping acoustic beam that does not require mechanical translation. However, among these arrays, there are limitations posed by the geometry of the elements such as the introduction of grating lobe artifacts, and certain arrays will also require the use of an elevational lens to achieve focusing in the elevational plane.

Arrays

The main types of transducers are single-element, linear array, annular array, phased array, and 3D transducers, which are a branch of phased arrays. The configuration of elements for these arrays are depicted below in Figure 2.10, where both linear and phased arrays utilize approximately the same element configuration.

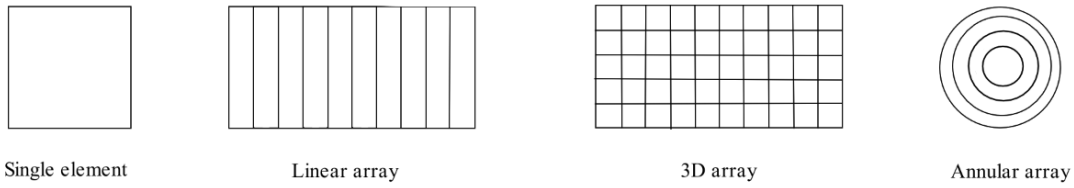

Figure 2.10 Depictions of the element configuration of a single element array, linear array, 3D array, and annular array.

Of the mentioned transducers, neither the single element nor the annular array transducers can produce sweeping acoustic beams. The inability to sweep the acoustic beam through the scanning area translates to the need for mechanical movement to acquire multiple scan lines, which may be done through side-to-side translation or rotational translation to form a single image. As each ultrasound image is composed of numerous scan lines stitched together to form a 2D field of view, it is evident how the requirement of mechanical translation, which can be time extensive, inaccurate, and subject to the possibility of the mechanical components breaking, may not be desirable. In comparison, linear arrays can produce full 2D images without the need for mechanical translation as they can sweep the origin of the beam through the line of elements.

Additionally, single-element transducers are unable to focus beyond a weak passive focusing due to its inherent geometric properties while an annular array can manipulate its focus down its central axis. In contrast, linear arrays are capable of electronically focusing throughout the image. Ultrasound focusing is achieved using three possible methods: through physical means, electronic configurations, or a combination of the two. A physical lens provides an immobile focus either through a curvature to the array itself or with an external lens, while electronic focuses are achieved by transmit and receive delays. By manipulating the delays in which an element is pulsed as illustrated in Figure 2.11, it is possible to electronically manipulate the locations at which constructive interference of the waves from each element occur, effectively focusing on that location. Unlike single-element transducers, array transducers also do not need to trade-off the lateral resolution achieved by focusing with the depth of field (the axial range in which this lateral resolution is achieved). Both of the above points will be further elaborated upon in focused line imaging.

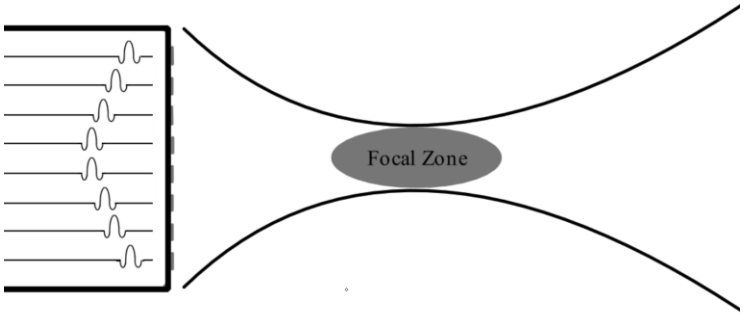

Figure 2.11 Linear phased array demonstrating elements being pulsed with time delays and how it creates a focal zone.

As such, compared to single-element and annular transducers, array transducers benefit from being able to acquire images without mechanical translation, the capability to focus throughout the image, and extend the depth of field without sacrificing lateral resolution.

Phased Arrays

Although both linear and phased arrays are fabricated with a linear array of elements, there are characteristics of phased arrays that makes them superior to linear arrays. As linear arrays acquire their multiple focused scan lines by multiplexing a sub aperture of their entire array down the length, the lateral dimensions of the image cannot exceed the transducer aperture [64]. Even after including the usage of steering, the final field of view would be a parallelogram where the width of the image remains the same as that of the transducer. Additionally, due to this manner of multiplexing a sub aperture down the transducer face, the transducer will typically have a large number of elements to produce both a sufficient number and sufficiently focused scan lines.

In contrast, phased arrays, also known as linear phased arrays, can image a significantly wider field of view. This is due to being able to angle each scan line individually by manipulating the delays applied upon transmitting and receiving. Unlike a linear array where a subaperture of elements are pulsed for every sound pulse, phased arrays utilize every, or almost every element to acquire each scan line, and uses the delays to manipulate how these scan lines are angled and where they are focused. Therein lies the benefit of phased array transducers: an ability to provide focused, high resolution real-

time scanning and do so with a transducer aperture significantly smaller than the field of view without requiring additional translation to build the image.

Focused Line Imaging

As previously described, focusing is achieved either through physical means such as geometrically shaping the piezoelectric substrate or a lens, or through electronic means. Electronic focusing had been briefly touched upon in the section on Arrays earlier, and more detail as to how electronic focusing is achieved will be elaborated upon here.

There are two parts to electronic focusing: focusing upon transmitting, called transmit focusing, and focusing upon receiving, called dynamic focusing [64]. Both rely on how the elements of a phased array can be individually driven, which allows the incorporation of time delays both into the transmitting and receiving. Figure 2.11 illustrates transmit focusing down the central axis, where it is possible to focus the acoustic beam by delaying the central elements, causing the acoustic energy from all elements to reach the focal zone at the same time. This is further illustrated in Figure 2.12 where through delaying one side of the elements more than the other, it is possible to focus the acoustic beam in plane towards one side of the field of view. This capability to steer the imaging beam to the sides with focused pulses enables imaging of a wider field of view.

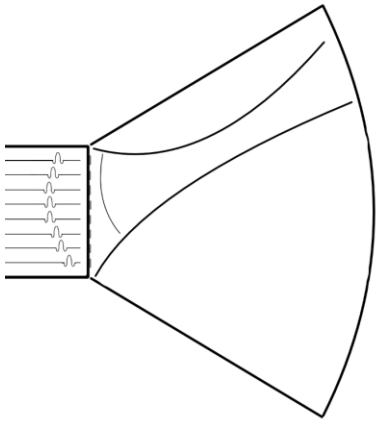

Figure 2.12 Phased array transducer focusing towards a side of the image

The other half of focusing is dynamic focusing, where a calculated time delay is added to the received signal at every element so the signals received from the same point in space

can be summed for a stronger signal. This is shown in Figure 2.13, where the individual elements of a phased array transducer are receiving signals from a point off to the side. As the signals are captured, a delay is applied so that all the signals from the same target are synced to produce a stronger signal [64].

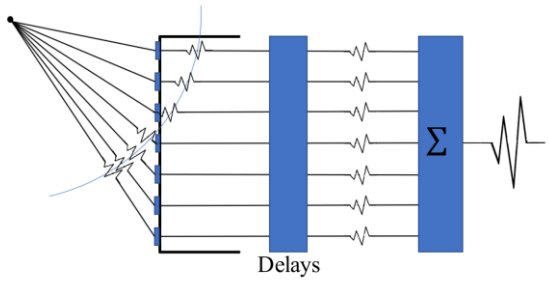

Figure 2.13 An illustration of dynamic focusing where the received signals are all delayed, synced and summed for a stronger signal from a given point.

One of the benefits of ultrasound compared to other medical imaging modalities is its capabilities to image in real time by transmitting and receiving hundreds to thousands of acoustic beams within a fraction of a second for high temporal resolution and focusing these beams to provide a high spatial resolution within the focal zone. In a general manner, the cost of high spatial resolution, or the addition of multiple focuses per image, comes at the cost of a reduced temporal resolution even if it is still efficient enough to be considered real-time imaging.

This trade-off between temporal and lateral resolution of phased array transducers is due to the nature of how focused line imaging functions. The time between the sending and receiving of each sound pulse is the time-of-flight and determined by the depth of the image as calculated by Equation 2.7.

$$t = \frac{2d}{c} \tag{2.7}$$

Where t is the time of flight, d is the distance between the transducer to the point source or the depth of the image, and c is the speed of sound within tissue.

Each pulse can capture the information to construct a single scan line with a single focus, and each additional focus added to the image would require an additional pulse per scan

line. Therefore, by increasing the number of focuses within an image from 1 to 2 would halve the frame rate should all other variables be held constant. However, by increasing the number of focuses within an image, more depths are imaged at a higher lateral resolution and as lateral resolution is one of the limiting factors of ultrasound image quality [65], directly contributing to higher image quality.

However, by combining the fact that phased array transducers produce singular, focused scan lines rapidly at varying, steerable angles, this demonstrates how these transducers can scan a sector shaped field of view instead of having the image width being constrained by the transducer width. Therefore, with the usage of a phased array signal processing strategy to achieve focused line imaging, linear phased arrays can produce real-time focused images that have both a larger depth of field and field of view than the other available types of transducers.

Grating Lobes

In ultrasound, there are multiple types of imaging artifacts: features that appear on the screen when they do not exist within the anatomy and are caused by tissue, mediums, or transducer characteristics. Grating lobes are ultrasound artifacts where extraneous sound reflections from outside the imaging plane are incorporated into the received sound due to reflection and result in artifacts within the image. They can be "pushed" out of the image by increasing the angle at which they are received, which forces them outside the image by decreasing the pitch between elements. The ultrasound array pitch is the distance between elements, including the element itself and the adjacent kerf.

The grating lobe location angle is calculated through Equation 2.8 where λ is the wavelength of sound within the active material, p is the pitch, and θ is the angle of the grating lobe from the normal [62].

$$\theta = sin^{-1}(\pm\frac{\lambda}{p}) \tag{2.8}$$

Through this equation, it is shown that it is generally desirable to have a pitch less than or equal to the length of a wavelength to push the grating lobe to 90°, or outside of the field

of view. In phased array transducers, the pitch is typically aimed to be either 0.5 or 0.75 of the wavelength to ensure that the grating lobes are pushed outside the main image when steering the beam to non-zero angles [63]. However, should the pitch be greater than the wavelength and the grating lobe localized to within the main image, it is possible to use sign coherence weighting to suppress the grating lobes in a manner as shown by [66]. Sign coherence factor (SCF) is a simplified phase coherence weighting factor and has been demonstrated to be effective in suppressing the grating lobes in phased arrays where the pitch size is sufficiently large for grating lobes to appear in the field of view [65], [66].

Elevational Lens

The importance of focusing cannot be overstated in the terms of acquiring images with significantly high resolution. However, as the linear array is a single line of elements, it cannot focus on the elevational plane due to the singular element in the height dimension. Unlike axial and lateral resolution, elevational resolution determines the slice thickness of an ultrasound image, preventing additional out-of-image structures from appearing as artifacts due to being near the scanning slice. Therefore, it is necessary to incorporate passive focusing into the elevational dimension, achieved through one of the previously mentioned physical means such as the application of an elevational lens. Equation 2.9 below is used to approximate the effective beam focus of the lens, where F is the focus distance, R_c is the radius of the lens curvature, and n is the velocity ratio between the lens material and water. [63], [67].

$$F = \frac{R_c}{(1-n)} \tag{2.9}$$

2.3.3 ULTRASOUND MODELS

In ultrasound design, there are two well-known and well-validated methods for modelling transducer response and beamforming: the KLM model and the Field II model respectively. By using these models, it is possible to design transducers based on a set of characteristics that one wants to achieve, such as bandwidth, resolution, frequency, secondary lobe, grating lobe locations and more. The models also provide a source of

comparison after fabrication, to evaluate the performance of the transducer and assess for significant differences and why they may have occurred.

KLM Model

The KLM model, abbreviated for its creators Krimholtz, Leedom, and Matthaei, is a lumped parameter model that takes the many components required for ultrasound and simplifies them into a series of electrical components [68]. As such, the KLM model can model the transducer response by taking the inputted electrical pulse and modelling the output acoustic pulse, and then further modelling the returned electrical pulse based on the chosen medium that the transducer supposedly received the signal from.

The benefits of the KLM model are that it is possible to toggle individual components of the modelled transducer, co-axial cable, and scanning medium to model the parameters of the probe to optimally meet the given characteristics and is an effective method of calculating the optimal matching layer thickness. After setting the ultrasound parameters as a series of matrices, the model takes an inputted electrical pulse in the time domain and through the outputs, calculates the corresponding pulse waveform, bandwidth (BW), acoustic working frequency (awf) and more as illustrated in Figure 2.14, enabling further calculation to obtain the axial resolution as it can be defined as the -6 dB width distance of the pulse waveform. However, as the KLM model calculates based off of singular elements, it cannot accurately model the behaviour of ultrasound arrays or those of more complex geometries.

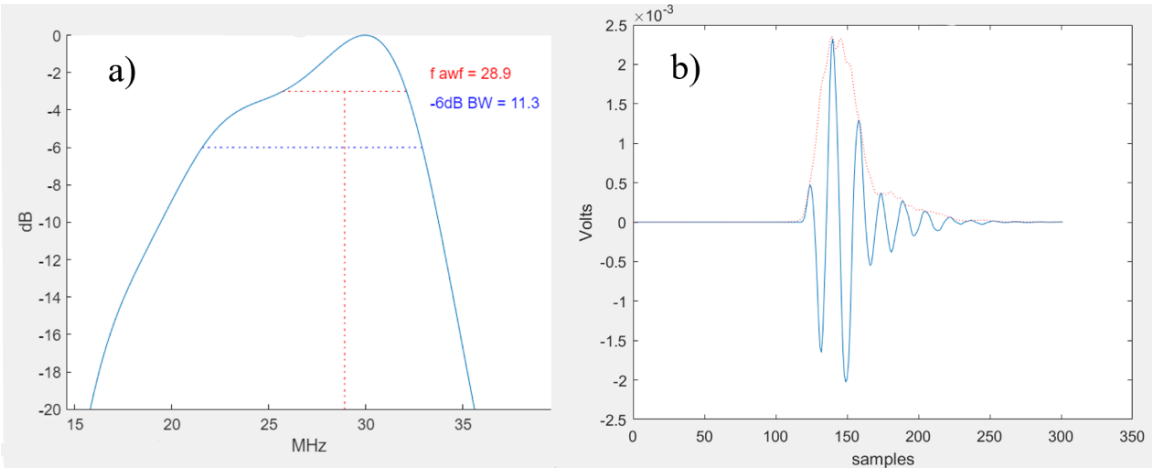

Figure 2.14 A KLM model of transducer with a matching layer demonstrating a) the two way pulse FFT with the -6 dB width calculated and b) pulse waveform with pulse envelope

FIELD II

The Field II program is similar to the KLM model in that it is a well-known and verified model, but instead simulates the ultrasound beamform or the transducer field. The program takes inputs such as the number and height of elements, element pitch, kerf spacing, operational frequency, the position of the point target and more to calculate and output a simulated ultrasound field.

The benefits of using Field II to simulate an ultrasound field lies in its ease of use for manipulation, allowing efficient tests of multiple parameters. Furthermore, the generated field can then be dissected at the depth of the point target to obtain a radiation pattern demonstrating the pressure across that slice such as Figure 2.15 (a), allowing efficient calculation of the simulated transducer's lateral resolution. The -6 dB width of the point target peak as illustrated below in Figure 2.15 (b) would give the lateral resolution of the particular transducer at that particular angle, and by varying the angles from the central axis at which the point target is present, it is also possible to judge the radiation pattern for the presence of grating lobes, their intensity, and their location. This is illustrated in Figure 2.15 (c), where all variables but the angles are kept constant and a grating lobe originally absent at 0° and 12.5° becomes visible at 25°.

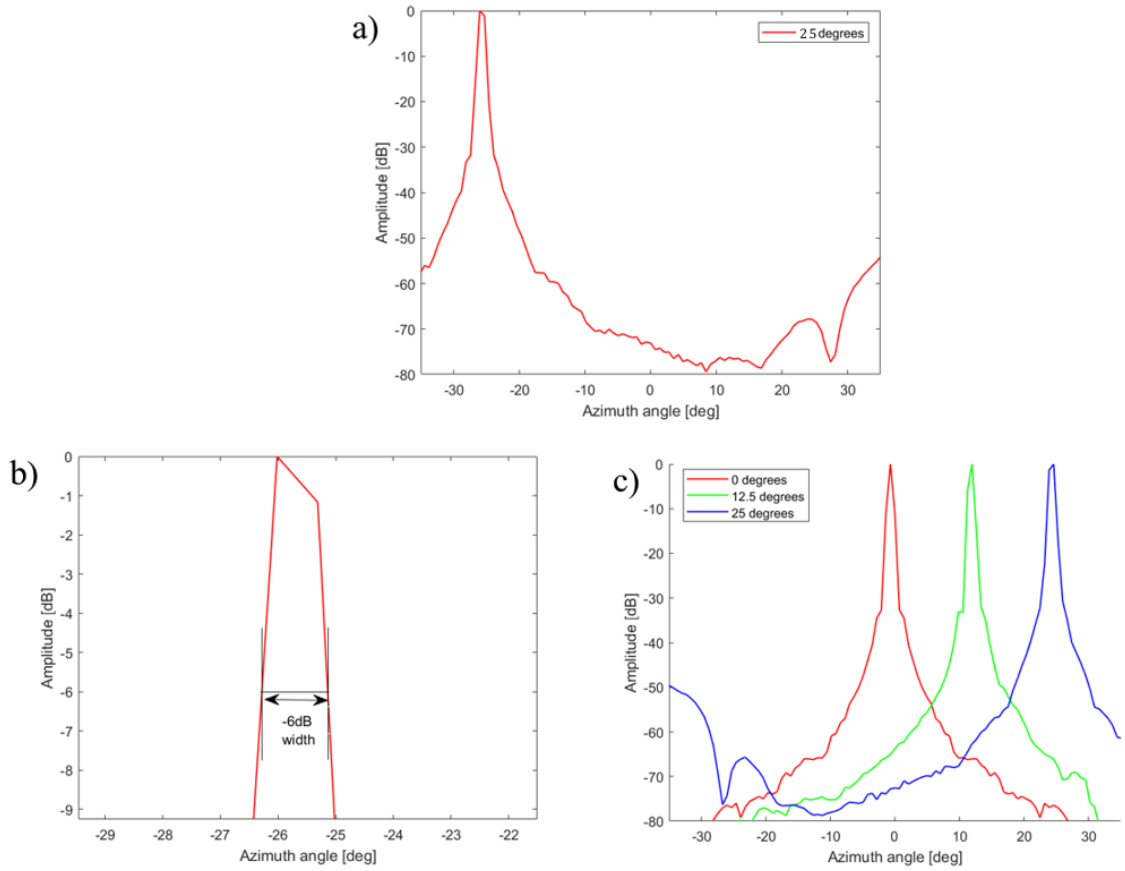

Figure 2.15 Field II radiation patterns to demonstrate a) 25° off central axis b) radiation pattern zoomed in to demonstrate the -6 dB width as the Azimuth angle and c) radiation patterns at 0°,12.5° and 25° to demonstrate the emergence of grating lobes.

2.3.4 ULTRASOUND IMAGING IN SURGERIES

As an imaging modality, ultrasound has long since proven to be beneficial during surgical procedures. Ultrasound has been commonly used to guide biopsies for both superficial masses such as those found in peripheral soft tissue and breast tissue, to deeper anatomy such as the liver and kidneys [69]. The usage of ultrasound during these procedures allows both live imaging of the needle, localization of the mass, obtaining images, and video clips of the biopsy needle penetrating the mass to ascertain its success and for future tracking. Needles used for ultrasound guided biopsies can range between 14 to 22-gauge, and under ultrasound guidance lesions as small as 5 mm can be successfully biopsied. [69] There is also the development of an ultrasound array capable of fitting

within a biopsy needle to provide further high frequency imaging and localization of micro-calcifications [30].

Outside of biopsies, ultrasound has also found a place in the OR as a surgical imaging modality where its ability to provide penetrative imaging in real time allows surgeons to access the surgical site in a quick and effective manner. As ultrasound and radiography are modalities capable of locating lesions within an organ in real-time while performing the necessary incisions to reach the lesion, they are invaluable tools in the OR. Within the realm of ultrasound, laparoscopic ultrasonography and endoscopic ultrasonography are of particular importance [70].

Ultrasound has also made an appearance in aiding visualization in spine surgeries, having been put in use as early as 1984. As demonstrated by Aoyama et al [71], LOGIQ 9 and 8c microconvex probes that operated between 4 - 11 MHz were used intraoperatively after a hemi-semilaminotomy was performed to access the spinal canal. The length of the skin incision was 3 - 4 cm, and saline was introduced to the cavity for ultrasound imaging. Adequate images were procured in all patients that required herniated disc removal, as well as normal anatomy such as the dural sac, nerve root, ligament, and other connective tissues. Ultrasound was also capable of visualizing residual herniated material after the surgeon had considered the procedure finished, and it was demonstrated that post herniated disc material removal the dural sac and nerve roots became easier to identify as compared to pre-removal, where the disc material may appear isoechoic to the nerve root. Furthermore, it was stated that ultrasound was only indicated for intraoperative use in spine surgeries where the operative field is of a larger size, which would rule out those that are conducted through minimally invasive means [71]. With the current trend of pushing for less invasive surgeries, it would be advantageous to provide a method for using ultrasound in these reduced spaces.

2.3.5 HIGH FREQUENCY ULTRASOUND TRANSDUCER FABRICATION

There are several components critical to the functioning of an ultrasound device. These components are the active element(s), the matching layer, the lens, the backing layer, the casing and ground shield, and the cable connecting the transducer to the remainder of the

electrical system. Each component plays a unique role in determining the functionality of the ultrasound transducer as they contribute directly to forming the electromechanical transduction. To understand the difficulty of fabricating high frequency ultrasound probes, it is necessary to first understand how ultrasound transducers are made and how the difficulty in fabrication increases with frequency. There are two transducer components of those listed that are the most challenging to fabricate at high frequencies; the piezoelectric array elements and the matching layer.

High Frequency Arrays

The operating frequency of the ultrasound transducer is primarily determined by the thickness of the piezoelectric substrate, where the thickness of the array elements are proportional to the wavelength of the acoustic wave. The thickness of the piezoelectric element is ideally ½ the wavelength of the sound wave as it passes through the material, and so the higher the desired frequency, the thinner the piezoelectric material needs to be. The formula for wavelength in terms of frequency is:

$$\lambda = \frac{c}{f} \tag{2.10}$$

Where λ is the wavelength within the material, c is the speed of sound within the material, and f is the operating frequency.

There are difficulties both in fabricating a very thin piece of piezoelectric material as well as complexities that occur in the micromachining of the array elements into the piezo. For example, lack of precision in the fabrication process may result in the piezoelectric substrate being thinner on one end of the array meaning elements have slightly different heights at one end of the array compared to the other. Considering the elements of a 30 MHz PZT array are approximately 54 µm tall, variation of just a few microns across the array results in a significant shift in operating frequency across the array and loss of image quality.

Engineers and researchers have taken multiple approaches to fabricating high frequency ultrasound arrays. As the pitch, element height, and kerf size all shrink as the desired

frequency increases, conventional micro-dicing saws are no longer capable of creating the necessary microscopic element and kerf sizes. Some approaches that researchers have taken to solve this issue include deep reactive ion etching [5], using stacked laminate [72], and even interdigital bonding to fabricate high frequency arrays [73]. While each method comes with its own benefits, they are also restrained by equipment, precision, materials, and efficiency. The method chosen in this project is laser etching, as the laser spot size, efficiency, and power are all suitable for the sizes of the kerfs and materials used for this work [74]. It is with recent advancements in micro-fabrication technologies that it has became possible to fabricate high frequency ultrasound arrays.

High Frequency Matching Layer

The matching layer is also difficult to fabricate for high frequency ultrasound transducers. As the frequency increases, the wavelength of the sound within a given material will decrease. When considering that the matching layer thickness is ¼ of the wavelength, this reduction results in an extremely thin and precisely machined layer. Additionally, the acoustic impedance of the matching layer will need to be carefully tuned to couple the piezoelectric elements to water, which is an additional challenge as this conventionally has involved the mixing of high impedance particles within a low impedance polymer at differing ratios [75]. While lower frequency transducers can utilize lapping methods to fabricate a thin matching layer that is glued to the transducer, this becomes rapidly unfeasible at high frequencies due to the decreasing margin of error and the sound wavelength approaching the size of the high-density particles [75]. As such, different methods have been used in the fabrication of the matching layer, such as a method based on a mass-spring approach, and another based on the electromagnetic microwave theory. Both methods are capable of circumventing the need for the matching layer to be ¼ of a wavelength thick [75], [76]. Another method that is still reliant on the ¼ wavelength thickness, but can be precisely thickness controlled, is with vacuum deposition of the matching material, such as parylene [76]. Regardless of the method, the matching layer is essential to ensuring the sensitivity and bandwidth of an ultrasound probe and a challenge to fabricate at high frequencies.

High Frequency Lens

In addition to the difficulty of fabricating a precise high frequency matching layer, to provide adequate elevational focus a lens tailored for the high frequency ultrasound is also necessary. A wide range of materials have been researched for ultrasound such as epoxy, metamaterial, adjustable liquid, silicone, sapphire, and fused silica lens [77].

However, in high frequency probes highly attenuating materials are avoided for the lens due to potential beam apodization and a significant drop in the transducer's sensitivity [78]. As the conventional material choice of a vacuum-deposited silicone rubber is too highly attenuating, this led to the use of a low-density plastic or resin for the lens instead [63]. Additionally, due to the silicone in conventional probes having a lower speed of sound than tissue, this allows the use of a convex lens, while the plastic or resin would be of a concave-shape due to having a higher speed of sound than human tissue [63].

Other Components

Additional components that would impact the imaging quality of ultrasound would include the backing material, transducer shielding, and cable impedance. The backing layer was illustrated in Figure 2.9 and functions to reduce acoustic pressure transmitting out the back of the piezoelectric material and ringing. The shielding is used to reduce the noise within the imaging, as the transducer contains sensitive electrical components and may detect unwanted signals from surrounding machinery, and the co-axial cable is necessary to carry the electrical signals to and from the transducer. The electrical impedance of the cable should match the transducer and the beamformer to optimize signal transmission.

2.3.6 MINIATURIZED HIGH FREQUENCY ULTRASOUND

General ultrasound probes in the hospital setting are of the large footprint variety. Although sizing differs between companies and probe types, low frequency transducers such as those used for abdomen, neck, and leg veins can be multiple centimeters wide, making them bulky tools to use and maneuver. This is especially true for ultrasound

transducers that achieve 3D imaging with a built-in motor such as those used for obstetrics imaging, where the probe is even larger and has a rounded face. Small-form factor transducers for pre-clinical small animal imaging and catheter-based transducers such as those used for intravascular or intracardiac imaging demonstrate an ability to provide high resolution imaging using smaller transducer probes, trading penetration for higher resolution imaging [79], [80].

Although single element miniature high frequency transducers have been successfully commercialized for decades in the form of intravascular transducers, very few high frequency array transducers have been developed [75], [79]. Single element IVUS transducers are mechanically translated to generate a 2D image and suffer from low image quality as the acoustic beam is not focused. Of the high frequency arrays developed to date, there are only one or two examples of successful commercialized probes, and these are not in a miniaturized form factor with a couple exceptions. Xu et al. [6] fabricated a 35 MHz 1D phased array for the purpose of intravascular scanning, where the transducer consisted of 12 elements with dimensions of 0.3 × 1 mm. By integrating 4 of these miniature transducers within a guidewire, the sector width allows it to be possible to obtain a complete 360° view of the vessel walls without the need for a motor. However, because of the low element count, the resulting image quality was low. Our own group at Dalhousie has previously developed a 2.5 mm forward looking 64 element 45 MHz phased array [79] and more recently a forward looking 3 mm 64 element 30 MHz array [81]. Finally, there has also been a lot of work in developing small form factor low frequency arrays for intra-cardiac-echocardiography (ICE). For example, Han et al. [80] fabricated a 10 MHz phased array intracardiac transducer with a packaging of 2 mm × 7.4 mm mounted on the end of an ICE catheter with the array mounted at a 90° angle.

When constructing an ultrasound probe, key features that characterize the operation of the probe include the number, width and height of the elements, the pitch, the thickness and acoustic impedance of the matching layer(s), the lens if applicable, and the thickness and acoustic impedance of the backing layer. Therefore, the size of the array would be dictated by the number and size of the elements and the thickness of the backing layer,

with the orientation of the array when mounting influencing the final packaging size. In higher frequency arrays, the elements, matching layer, and backing are a magnitude smaller than general use lower frequency probes, and so it is less of the array size resulting in difficulties of additional miniaturization and more due to the electrical interconnects.

Compared to array transducers, single element transducers are considerably easier to miniaturize as only the one element requires an electrical connect and are therefore easier to manage. However, to connect the circuit board traces to the elements of the array, the size of the elements and the orientation of the circuit board become considerably more relevant, both in terms of size and difficulty. The method of array interconnect would influence the lateral dimensions of the probe as demonstrated by [79], where an interconnect method of wire bonding the traces in the PCB's thickness dimension to the array's bonding pads was used in the present study. By connecting in the thickness-dimension of the PCBs instead of the length, this method reduced the lateral dimensions by saving the space that the bending of a flexible circuit board would have occupied.

CHAPTER 3 METHODOLOGY

Chapter Synopsis: This chapter describes the design, fabrication, and method of testing of a high frequency angled ultrasound endoscope developed in this thesis. The chapter will first provide details on the design of the probe to meet the requirements for this clinical application. Next, this chapter will describe the fabrication process developed for the probe, the methods used for performance testing/characterization of the endoscopes, and finally the approach to demonstrate imaging for proof of concept.

3.1 DESIGN

It was necessary to first define the required performance metrics of the ultrasound endoscope prior to fabrication for this application of guiding MISS. This was done by assessing what characteristics were required for it to be useful in the surgical environment such as the ergonomics for this narrow surgical approach, image size, and resolution. To determine the parameters for the array design, two ultrasound models described in the following sections were used to simulate spatial resolution and secondary lobe levels.

3.1.1 DESIGN REQUIREMENTS

The endoscope was designed to be used within a surgical tubular retractor with an internal diameter of potentially less than 15 mm. As the endoscope would need sufficient room for maneuvering as well as allow the presence of other surgical tools within the space, it was determined that the form factor of the endoscope tip should be limited to 4 mm × 4 mm. The tubular retractors are also equal to or less than 12 cm in length, which led to the endoscope requiring a neck length of at least 12 cm. Furthermore, the endoscope would have a bayonet bend after the neck like other minimally invasive surgical tools to accommodate visualization down the retractor tube without the surgeon's fingers blocking the view. Therefore, the endoscope was designed to have an outer packaged aperture of 4 mm × 4 mm, a neck length of 12 cm, a total length of 16 cm including the bayonet bend and completed with an ergonomic probe handle designed by a fellow lab member for ease of manipulation. Finally, as the retractor tube approaches the spinal canal lateral to the spinous process, an angled face of 40° to the normal was

designed at the tip of the probe to optimally capture anatomy within the spinal canal outside of the direct field of view as shown in Figure 3.1.

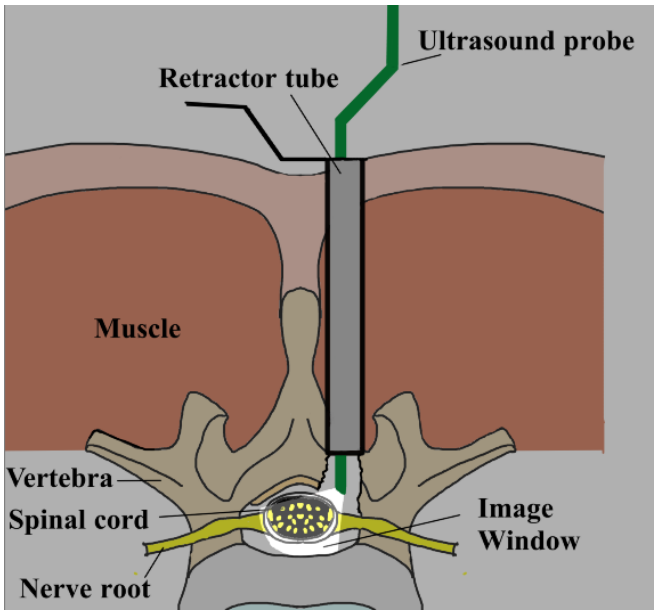

Figure 3.1 Concept diagram of the ultrasound endoscope within a retractor tube and corresponding window of visualization with an angled face.

The design requirements for the array itself are dependent on what anatomy visualization is desired from the ultrasound images. For this application, the endoscope needs to be capable of delineating the dura mater and the potentially thinner than 1 mm CSF that surrounds the nervous structures within the spinal canal as depicted below in Figure 3.2 [82]. This will be important for determining whether there is compression on any nerve roots or whether the nerves are freely floating in the CSF. It will also be important to visualize whether the dura is indented from an external disk or bone spur. In its decompressed state, the dura should appear round and smooth. To visualize these details, it was estimated that it would require a lateral and axial resolution of <150 μm to resolve the nerve root within the CSF of the dural sac [83], [84]. It is also desired for the array design to suppress secondary lobes to less than -60 dB, which is the standard for ultrasound images to have good soft tissue contrast. Additionally, a scanning window of ±35° and a depth of 15 mm would be required to capture the entire spinal cord, as the average transverse diameter of the largest cross section of the spinal cord is approximately 14 mm [85].

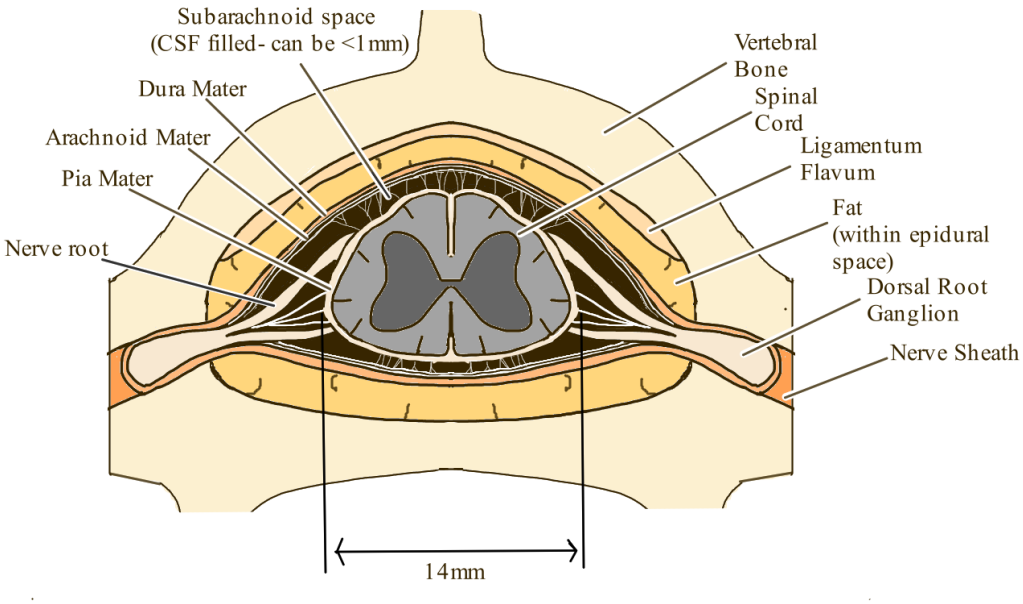

Figure 3.2 Enlarged depiction of the internal structure of the spinal canal with measurements denoting the requirements of an endoscope.

3.1.2 DESIGN PARAMETERS

Once the required performance parameters were determined, it was possible to use modeling to find corresponding array dimensions and outer probe aperture. Both the previously introduced KLM model and Field II simulations were used in the modelling of the array, and a starting point for design parameters were taken from previous work in the lab [81], where a 30 MHz phased array transducer was fabricated to provide live rodent brain imaging during ultrasound therapy.

As mentioned, to provide the high-resolution imaging required for resolving the fine structures within the spinal canal, the resolution must be <150 µm. To provide sufficient imaging depth within the spinal canal, the transducer also needed to be able to image at least 15 mm deep with a steering angle of ±35° as this would capture the entire spinal cord. From previous work in the brain with a similar transducer design, a 30 MHz array was able to penetrate up to 15 mm and had a resolution of 40 µm – 130 µm [81]. Therefore, this work's endoscope also began with the parameters established by the neurosurgical probe as this array met the acoustic design requirements.

Using the Field II simulations, an array was designed that had a fixed operating frequency of 30 MHz. This frequency was chosen because we knew from previous work that this frequency would provide 15 mm of penetration depth and allow for visualization of the entire spinal cord, as well as the best possible resolution for this imaging depth. Through simulations, it was determined that 64 elements with an element-to-element pitch of 48 µm and element height of 2 mm should yield a lateral resolution of 106 µm at 0°, 110 µm at 12°, and 119 µm at 25° at a depth of 7 mm, as illustrated in Figure 3.3. The array was also designed with a sub-diced zigzag through the middle of each element to suppress lateral modes [81]. In addition, the simulated design goal for the level of secondary lobes suppressed below -60 dB was met and the grating lobe when steering to 25° was located at approximately -30°.

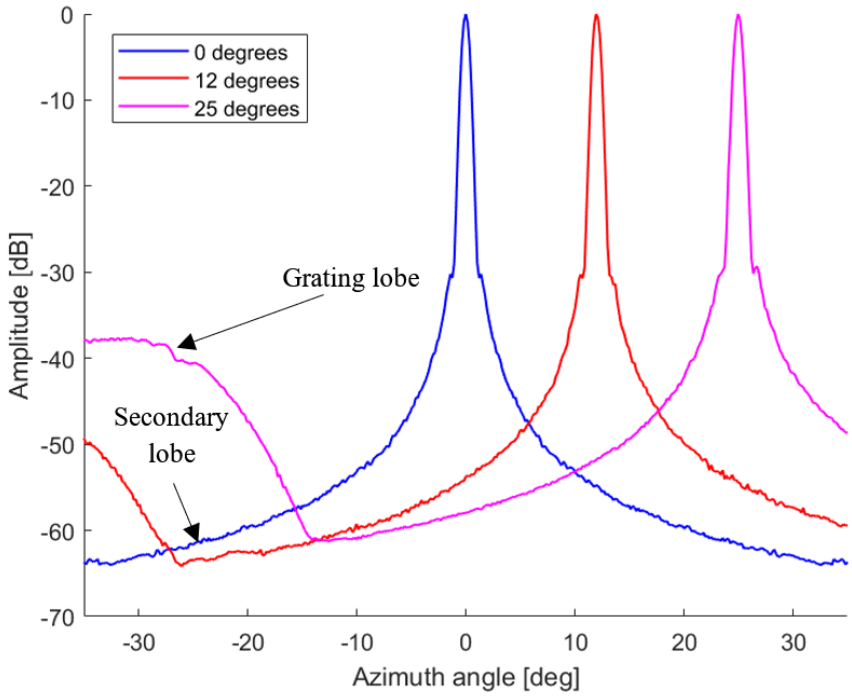

Figure 3.3 Radiation pattern of the modelled transducer at 0°, 12°, and 25°.

The parameters were then modelled using a MATLAB KLM program that was developed and modified in house. The resultant bandwidth and pulse waveform are shown below in Figure 3.4. The modelled bandwidth was demonstrated to be approximately 59.4%, the peak frequency at 32.3 MHz, and the axial resolution as obtained from the waveform

envelope was calculated to be 32 µm, sufficient for the purposes of resolving the relevant spinal anatomy.

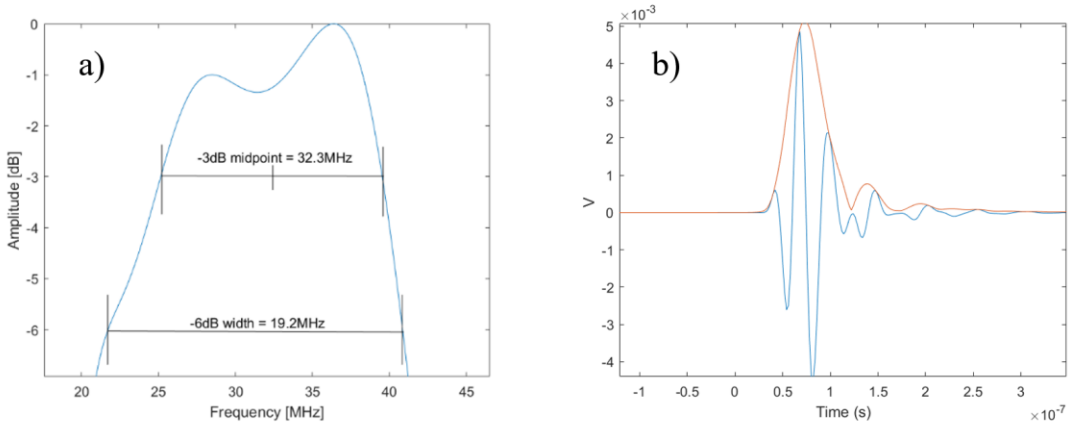

Figure 3.4 KLM model demonstrating a) the bandwidth from the frequency spectrum and b) the waveform in blue and the Hilbert transformation envelope in red.

The parameters used for modelling the KLM model with the cable, matching layer, and tuning all enabled are recorded below in Table 3.1.

Table 3.1 Parameters used for modelling the KLM model

Parameter	Value	Parameter	Value	Parameter	Value
Element area	9.6×10^{-8} m^2	Piezo Clamped Dielectric	3100	Matching layer Speed of sound	2142 m/s
Element Thickness	52 µm	Piezo Density	6300 kg/m^3	Matching layer Impedance	2.66 MRayls
Water impedance	1.54 MRayls	Piezo Coupling kt	0.50	Matching layer Thickness	19 µm
Backing impedance	9 MRayls	Piezo Speed of sound	4170 m/s	Matching layer loss	2000
Pulse centre frequency	30 MHz	Piezo loss	100	Cable transmission speed	2.21×10^8 m/s
Damping coefficient	2×10^{16}	Cable loss	0.09	Cable length	2.65 m
				Cable impedance	75ohm

3.2 FABRICATION

The probe that was fabricated for this project was a long neck, small form factor, high frequency, angled scanning face ultrasound transducer. Although individually many of these characteristics would not be cause for a significant increase in fabrication difficulty compared to the endoscopes previously fabricated at the µSonic lab for neurosurgery, all changes resulted in many unforeseen obstacles. A detailed methodology of the fabrication process is outlined below, from the designing and manufacturing of the components, assembling the base form of the probe, wire bonding, to casting on the matching layer and lens.

Multiple probes were fabricated over the course of this study, with varying frequencies and characteristics owing to the minor variations that occurred during the fabrication process. These characteristics were documented when possible.

3.2.1 COMPONENTS

There are three primary components that are required in the fabrication of the angled high frequency ultrasound probe: the printed circuit board (PCB), the 3D printed base, and the array stack. Components that are additionally required for the probe to generate images would be the cable and cable connector, the beamformer, and the software necessary to electronically focus the transmit and receive signals, then digitize and transform them into a scan converted image. All these additional components were developed prior to this project.

PCB

The design of the PCB was modified from a neuro focused probe previously fabricated in the µSonic lab. The modifications necessary for this project included an elongation of the PCB neck, and an angle incorporated into the tip. As per the requirements, it was deemed that an angle that was 40° from forward looking would be ideal. The angled traces at the tip were purposefully designed to be longer than the probe would require as demonstrated in Figure 3.5, as this allows dicing (see the white line) using a micro-dicing saw to obtain

exposed and polished copper traces that will act as wire bonding pads [79]. The PCB board designs were sent to an external fabrication company to be made to the required specifications (Summit Interconnect, Santa Clara, CA, USA).

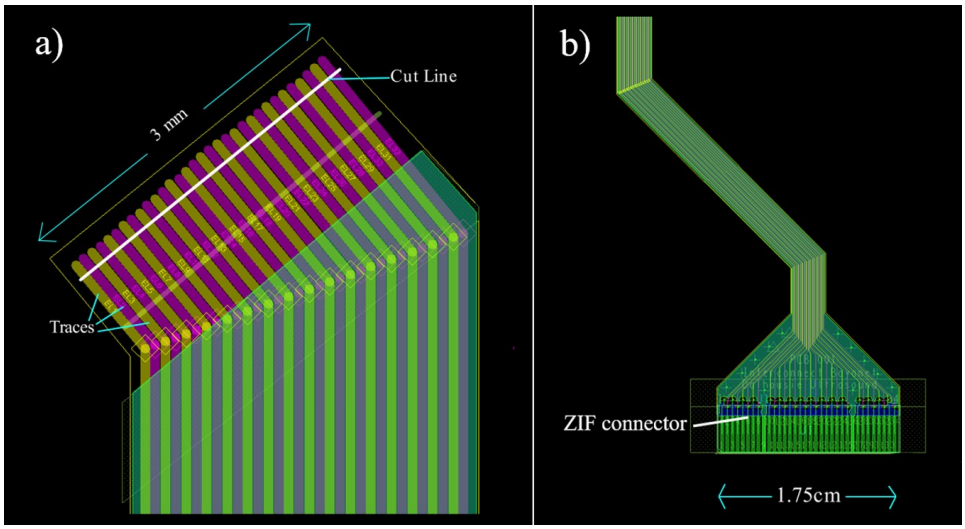

Figure 3.5 Enlarged view of the PCB depicting the a) traces and the angled tip and b) the bayonet bend and the ZIF connector.

3D Print

The 3D prints as shown below in Figure 3.6 serves as a base to both hold the circuit board and array stack in place, as well as to provide structure and durability to the endoscope. The initial design, similar to the PCBs, were modified from bayoneted forward looking neurosurgical probes. The necks were elongated corresponding to the extended length of the PCB's neck, and a rounded beveled side was incorporated into the design as a reference for PCB positioning and for an overall rounded contour, visible in Figure 3.6 (b). A channel as seen in Figure 3.6 (c) was designed to run down the junction between the raised sides and the seat of the PCB to leave a margin of error when printing. The 3D print prototypes were printed in the lab with V4 white methacrylate resin in a Form 2 printer (Formlabs, Somerville, MA, USA), and the edges were carefully pared and sanded down to remove any potential sharp edges. Unlike the PCB designs where the angled tip was a protrusion to bond the edge of it to the stack, the tip of the 3D print was concave to accommodate the height of the inserted stack and the epoxy, also seen in Figure 3.6 (a) and (c).

Of the three components, the 3D prints underwent the most iterations. Later iterations gained wings at the handle-end to allow a better fitting into the handle, while neck-long channels were added to the rounded beveled sides to permit the passage of ultrasound gel when inserting the probe into a sheath. The finalized model as of writing this thesis is presented below in Figure 3.6, where (a) presents the two pieces that make up the endoscope base, and (b) and (c) present the later added wings and channel through the print. The 3D print was also split into two pieces for assembly, as the ultrasonic welding wire bonder (model 4526, Kulicke & Soffa, Singapore) was unable to accommodate the full height of the print. The connection between the two pieces was a dovetail connection, and the finished prints were carefully modified with a scalpel and fine-grained sandpaper to ensure a smooth fitting.

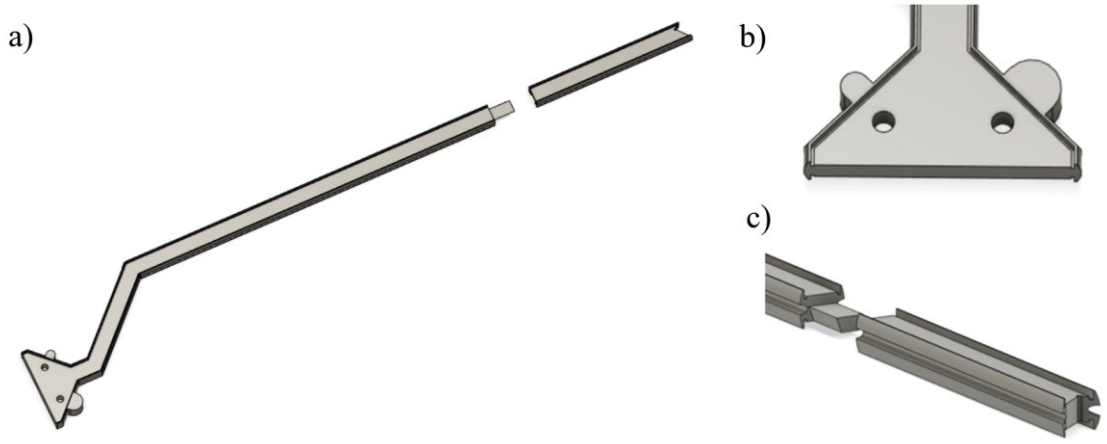

Figure 3.6 a) both pieces of the 3D print b) wings on the cable end c) channel and dovetail connection.

Array Stack

The final component that required fabrication was the ultrasound array stack: the smallest and most delicate of the three components, as well as the one most prone to error. The subdiced phased array for this endoscope was designed and fabricated in-lab in a similar way to that described in [81]. A piezoelectric substrate (PZT-5H, piezo.com, Woburn, MA, USA) diced to approximately 2 cm × 2 cm was lapped to a thickness of 54 µm, with 2 µm aluminum sputtered on the front side and 0.8 µm on the back. The lapping process was completed over multiple runs until the target thickness was reached to minimize

error. The sample was then backed with a conductive epoxy mixed with tungsten powder to increase its density. While the piezoceramic component measured 54 µm thick, the complete wafer including the backing epoxy was approximately 2 mm in height and the backing was also lapped flat. The wafer was then mounted with the backing side down (piezo side up) and the array pattern was cut onto the slab with a 3 µm spot size, 355 nm wavelength pico-second laser (Oxford Lasers, Didcot, England, UK).

The laser-etching stage would cut multiple arrays into the piezoelectric wafer, up to 30 under ideal circumstances. An electrode pattern is first etched on the surface of the array electrodes and wire-bonding pads. The laser then cut kerfs between the elements all the way through the piezo substrate. In addition, the elements were sub-diced with a zigzag pattern to supress any lateral modes within the elements as inherited from [81]. The etching and cutting speed, power, and number of runs may all vary depending on the materials used for the electrode and the status of the laser, but the desired results were elements with a pitch of 48 µm, kerf width of 8 µm, and elements sub-diced with a 3 µm – 4 µm wide zigzag pattern. Widened bonding pads were etched at the ends of the electrodes to facilitate easier wire-bonding. Before laser etching, it was necessary to assess the sputtered surface to ensure that there were no scratches or other types of superficial damage crossing the area of the array as it may result in a disconnect or shorting of the elements.

The final step of fabricating the arrays was using a DAD3220 dicing saw (Disco, Tokyo, Japan) to individually cut out the arrays. This requires a 500 µm blade and a procedure of performing cuts on one side of one array at a time to best preserve each individual array. To prevent the stacks from detaching from the glass slide that they were bonded to, the arrays were re-bonded to the glass slide after each cut with wax. Once the arrays were diced and separated into individual stacks, they were gently cleaned with methanol to remove remnant traces of wax from the bonding process.

3.2.2 ASSEMBLY

The precise assembly of the fabricated parts is essential for a successful wire bonding and the structural integrity of the final ultrasound endoscope.

The first step of the assembly process was to put together the base of the probe, which consists of the two PCBs that electrically connect the array to the cable and provides the grounding with the 3D printed base. Due to the length of the spine probe and the limited height clearance for the wire bonder in the lab, it became necessary to manage this in two steps where the tip of the 3D printed base was first assembled with the PCBs instead of using a singular print. This affords the assembly sufficient flexibility to be used within the wire bonder. An array stack was temporarily affixed to the tip of the 3D print for better alignment of the circuit traces with the elements on the array under the microscope during bonding, as each exposed trace needed to match up to an element on the array. Another dimension to align was the height, where while it was permissible for the edges of the PCBs to be slightly higher than the surface of the array, the array face being higher than the PCB edges would be detrimental for wire bonding. As such, it was with nonconductive epoxy that the 3D print was carefully aligned and joined together with the PCBs, in both the height and side-to-side orientations. Following the mounting process, the stack was then aligned and bonded to ground connection pads on the inside of the PCBs using conductive epoxy. Figure 3.7 below shows a prototype where the array was just mounted on the probe tip. It can be noted that the bonding pads were closely aligned to the traces of the PCBs and there is the smallest amount of conductive epoxy visible between the array and the PCB on the left side of the image.

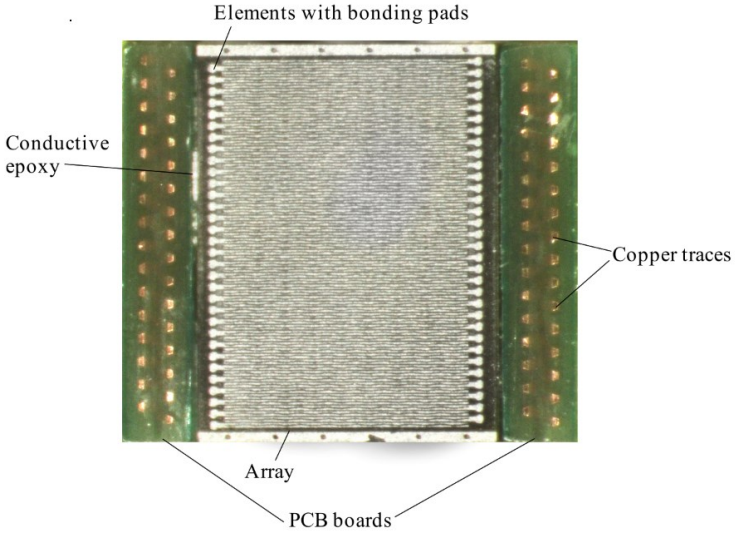

Figure 3.7 Labelled figure of aligned array between diced PCBs.

Mounting the array was carefully performed under the microscope. However, as this process was where mistakes were most likely to occur and ruin the array, it requires a great deal of additional care. A thin layer of conductive epoxy was applied to the cavity where the array was to be mounted, with the amount sufficient to both ensure that the array is firmly in place and to electrically connect the grounding of the PCBs with the backing of the array as depicted in Figure 3.8. The array was carefully set into the base while ensuring that displaced epoxy does not overflow from the seams to reach the elements or the exposed circuits.

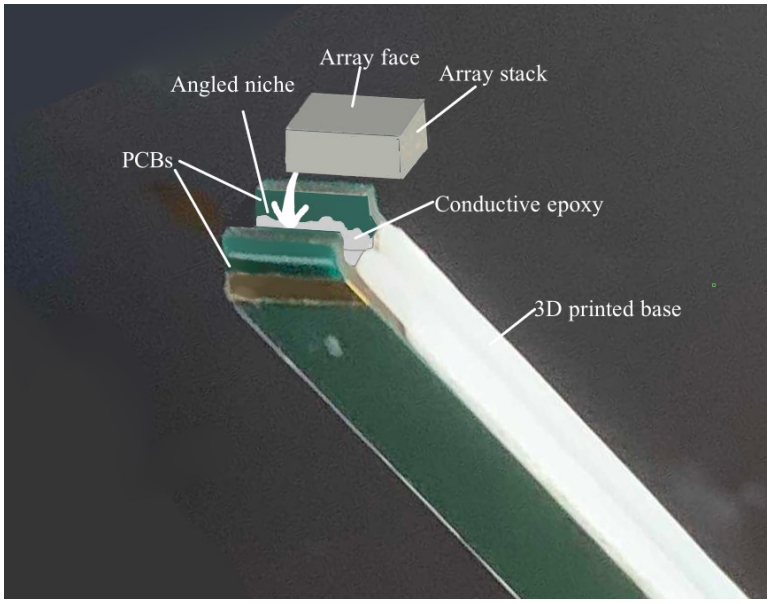

Figure 3.8 Mounting an array stack.

Due to the conductive nature of the epoxy, any epoxy reaching the kerfs may result in a shorted element. Figure 3.9 provides a few examples of potential accidents that may occur during the mounting process such as (a) scratching of the array face, or (b) conductive epoxy flakes between the kerfs.

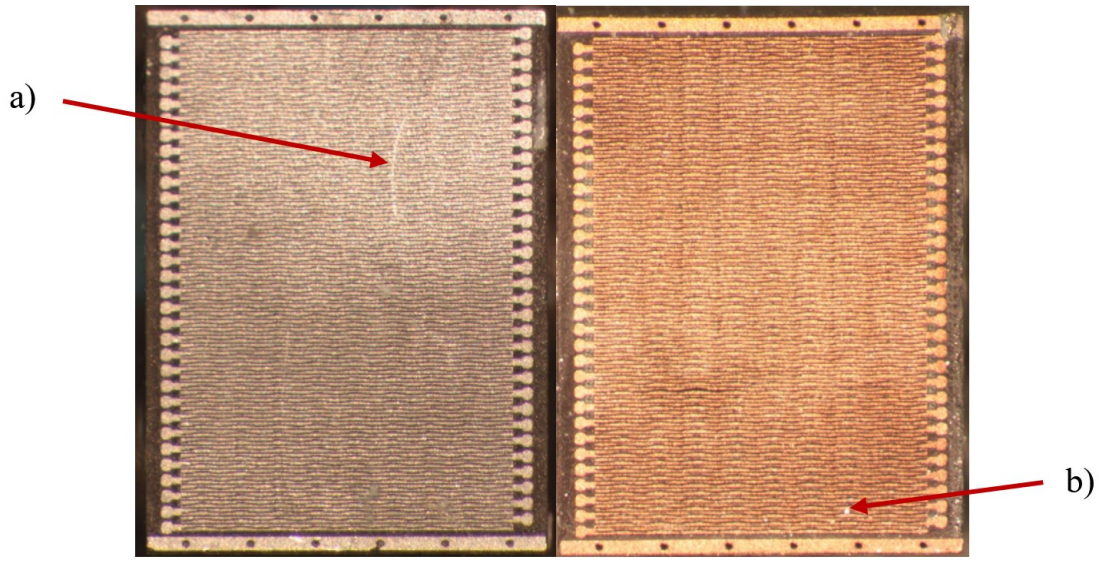

Figure 3.9 Arrays rendered unusable due to a) scratch b) presence of conductive epoxy within the kerfs.

A partially assembled probe is depicted below in Figure 3.10, where the array has been mounted and has yet to be wire-bonded.

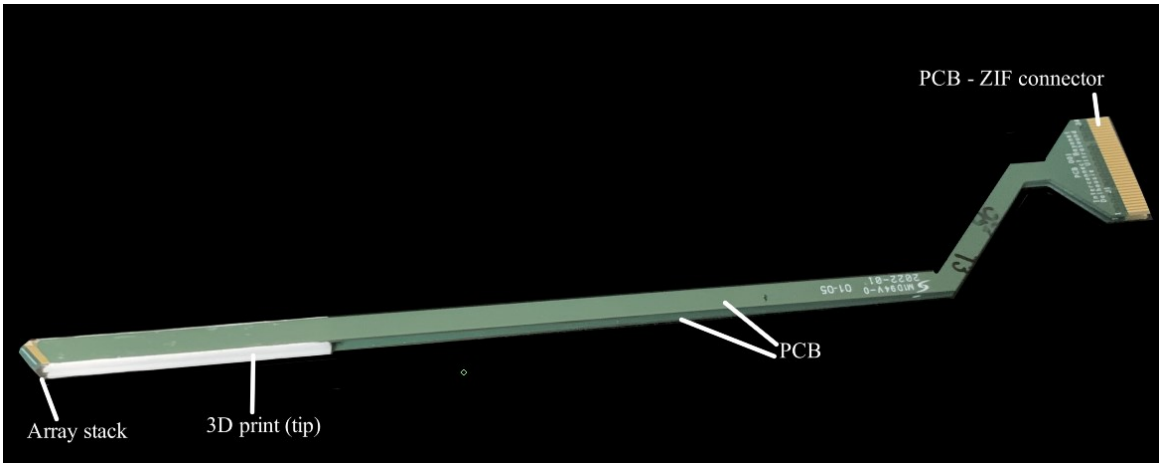

Figure 3.10 A partially completed endoscope just prior to the wire-bonding step.

Once the epoxy has set, the array elements were wire-bonded to the PCBs using 15 µm diameter aluminum wire connecting the wire bonding pads on the array to the exposed copper PCB traces.

The wire bonding process as illustrated in Figure 3.11 was the final step to making the endoscope electronically functional, and as such before proceeding onwards to applying

the remaining working layers it is prudent to check the integrity of the elements using an impedance analyzer. If any elements were found to be non-functional, it was necessary to inspect the wire bonds for any breakages or non-connections and repair them if possible. Depending on the results of this interim testing (e.g. how many elements are functional), the probe may be declared non-viable and scrapped.

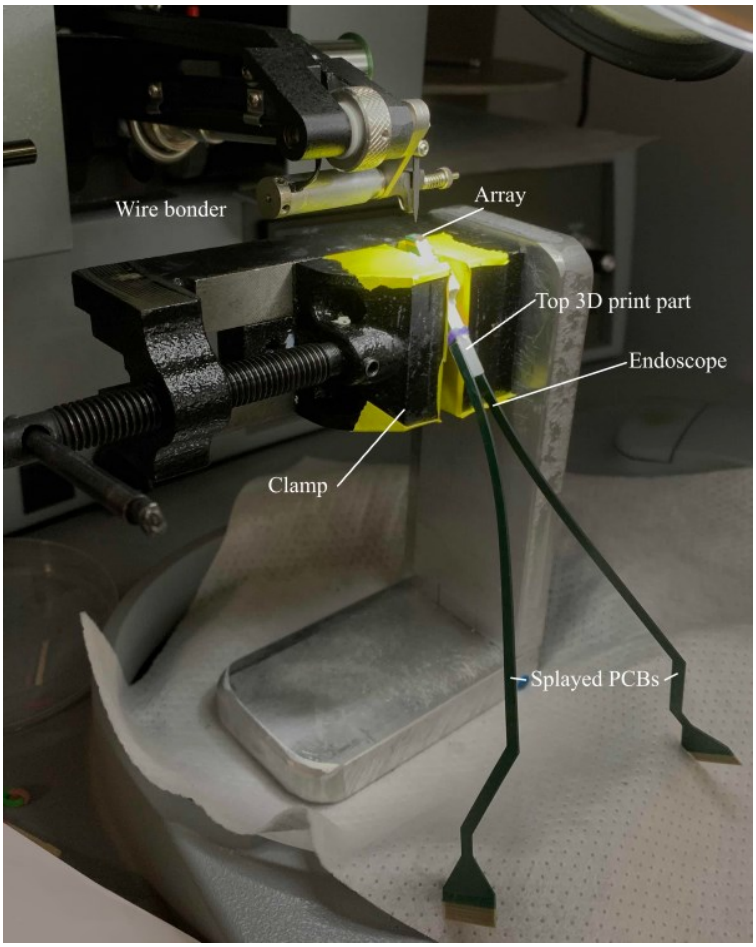

Figure 3.11 Wire bonding set-up.

Due to the fragility of the exposed wire bonds, they were carefully encapsulated with a potting epoxy to hold them in place, shown below in Figure 3.12. The second half of the 3D print was attached after the potting epoxy has cured.

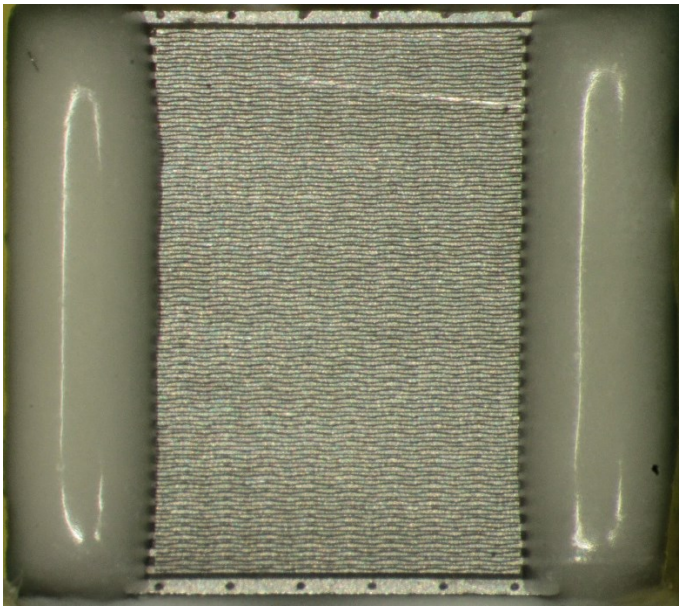

Figure 3.12 Wire-bonded and potted array face, where the wire bonds are obscured from view by the opaque potting epoxy.

3.2.3 FINAL LAYERS

After assembly of the main components of the probe, the next step was to apply the matching layer and the lens. Both steps were preceded by plasma etching, as it removes microscopic debris from the array surface and roughens the overall surface of the endoscope. This provides a better surface for the deposited layers to adhere to, as delamination is a potential issue that may occur even after the endoscope's completion.

Matching Layer

The matching layer material used was parylene C (Specialty Coating Systems, Inc, Woodland Drive Indianapolis, IN, USA), a biocompatible and conformal coating for electrical components that can be vacuum deposited onto samples due to its vacuum stability. The electrical connections at the end of the probe were first carefully covered and sealed with electrical tape to prevent parylene from coating the connections, and then a thin layer of parylene was deposited onto the endoscope using a specialty deposition machine. This is illustrated in Figure 3.13. The effectiveness of this material as a matching layer and deposited in this manner is demonstrated in [76].

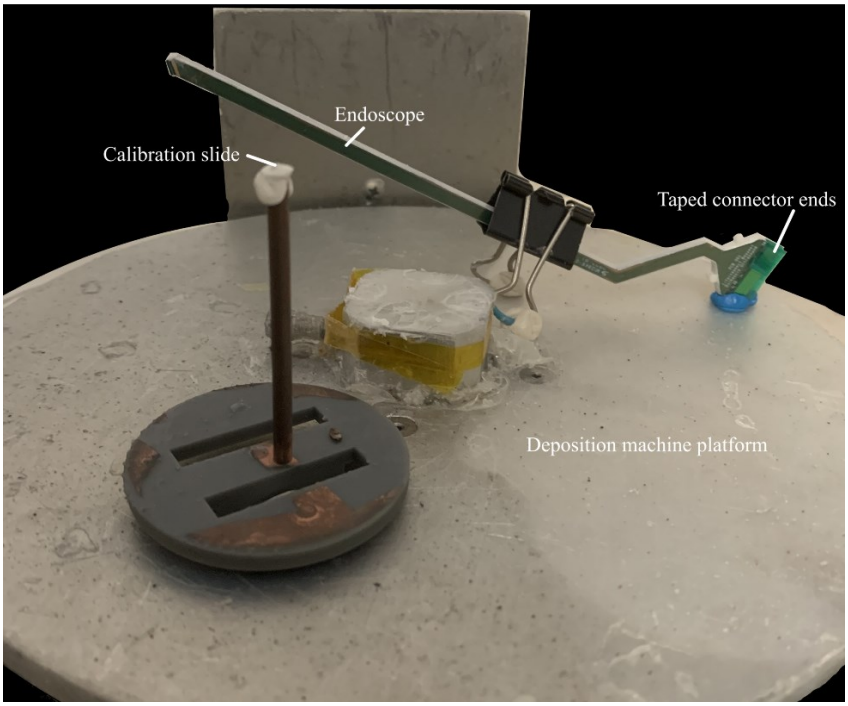

Figure 3.13 Matching layer deposition set-up.

As mentioned in above 2.3.1 ULTRASOUND PRINCIPLES, the purpose of a matching layer is to match the acoustic impedance of the piezoelectric material to that of tissue or another coupling medium, thereby maintaining a large bandwidth for high resolution. The equation used for determining the matching layer's acoustic impedance is derived from the acoustic impedances of the materials it bridges. However, as the material was determined to be parylene C, it was only necessary to use a KLM model to optimize the desired thickness. An in-lab KLM model program takes the measured impedance magnitude and phase curves to produce a matched simulated array impedance by adjusting the parameters of the piezoelectric stack, and the matching layer thickness is optimized through simulation after adding in the electrical components such as the co-axial cable and endoscope PCB. For each potential transducer, this was performed for several elements to obtain an average ideal matching layer thickness. As the endoscopes fabricated for this project operated in the 25 MHz to 35 MHz range, the parylene layer thickness predicted for optimal signal would be generally found between 19 µm to 23 µm.

To prevent evaporating an excessive amount of parylene onto the array face, the deposition was typically completed in a two-step process. The first run would use the calibration of the previous runs of the deposition machine to reach approximately 80-90% of the desired thickness. After this first round of parylene, the probe would be taken back to the impedance analyzer to analyze the amount of deposited parylene to derive a new calibration constant with the KLM model. The new calibration constant would be used in the second top-up run that targets the final thickness. The probe with the completed matching layer would be once more characterized using the impedance analyzer and the KLM model, both for the final thickness and to save the information as part of the probe's data.

Elevation Lens

In this linear phased ultrasound transducer, an elevational lens is necessary to focus the beam in the elevation dimension and define the slice thickness. The lens curvature of the endoscope in this work was designed to be 2.77 mm in radius, producing a beam focus at 8.3 mm in accordance to Equation 2.9 [67]. The lens material for the endoscopes fabricated in this project was composed of Alumilite water clear polyurethane resin (Alumilite Corporation, Michigan, USA), with an estimated speed of sound of 2250 m/s. In practice, however, this lens on a 30 MHz endoscope has been demonstrated in lab to produce a focus at a depth of 6.5 - 7 mm.

After the parylene coated probe has been plasma etched again, the endoscope face was carefully cleaned and inspected for areas where the parylene might have delaminated. The lens was then cast onto the probe using a Teflon rod with a radius of 2.77 mm and a self-designed silicone mold fitted to the tip of the probe. When positioning the mold and Teflon rod on the probe face, it was done so in a manner to keep the lens thickness as low as possible. A cut-through diagram of the process is shown below in Figure 3.14, where the Teflon rod would sit just above the probe face when the mold is in place. The lens material was carefully deposited into the mold with the use of a 22-gauge needle. Both the mold and the Teflon rod were held in place with sticky tack to prevent shifting when transporting the endoscope and the casting set-up. To prevent the presence of bubbles within the lens, the mixed Alumilite water clear solution was degassed in a vacuum

chamber prior to the casting. To prevent the resurgence of bubbles in the curing process, the endoscope cured in a pressure chamber held at 100 psi at 70°C for approximately 7 hours.

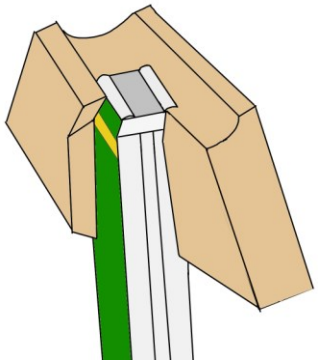

Figure 3.14 Cut through of probe prepared for lens casting with mold, not to scale.

The mold was removed by carefully carving through with a scalpel after the lens has cured, and the Teflon rod gently eased off to prevent the lens from delaminating. Any excess material that may have seeped out into the surrounding mold was removed with a razor and the sharp edges of the lens were pared down. As the edges of the lens were positioned above the potting of the wire bonds and not the effective array surface, the edges can be blunted significantly without any detriment to the imaging. An additional step to secure the lens to the probe and to round out any remaining edges was to spread a thin layer of MarineWeld epoxy around the boundary between the lens material and the endoscope body. A completed probe is shown below in Figure 3.15 (a), and a close-up of the probe tip is presented in (b).

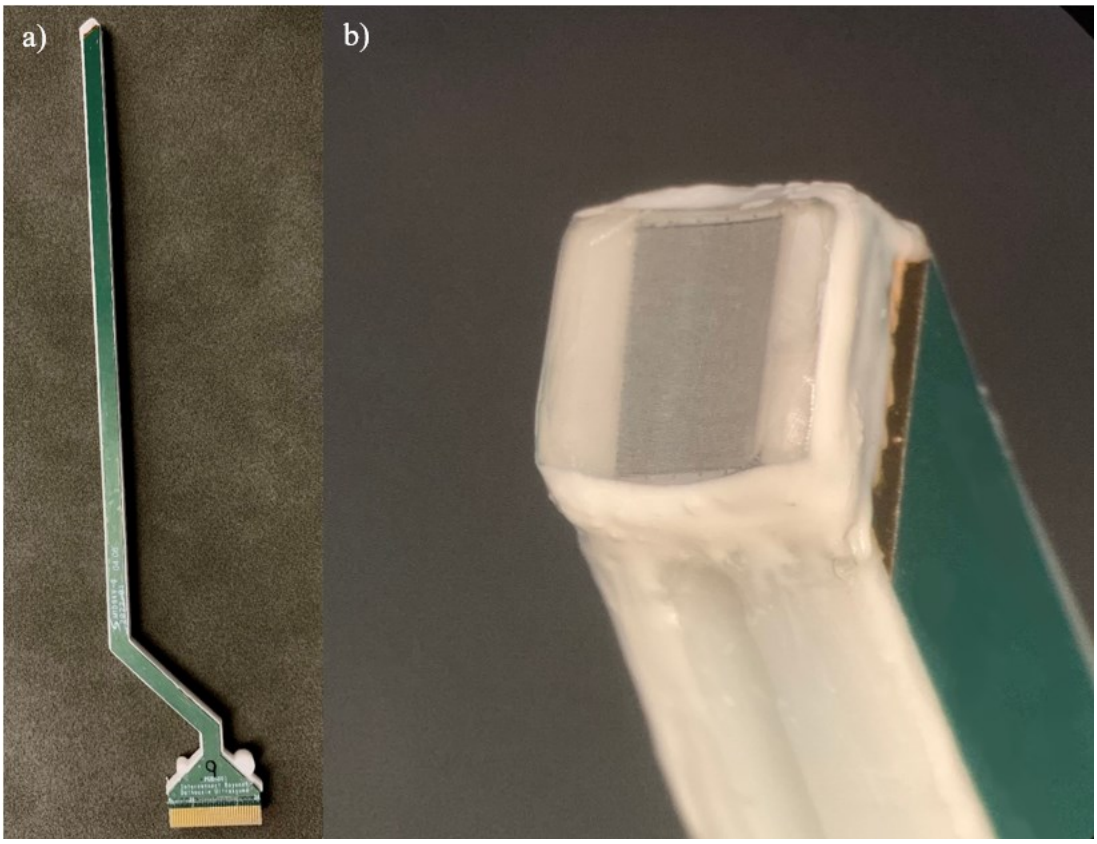

Figure 3.15 a) Completed endoscope and b) close-up of endoscope tip.

At this stage, the fabrication process is technically complete. However, due to piezoelectric materials depolarizing from high temperatures experienced during the fabrication process, an additional step that could potentially increase the sensitivity of the endoscope would be to repolarize the endoscope. The repolarizing process was performed at 80°C for 2 hours, where every 1 μm of PZT thickness requires 2 V for repolarizing. A final electrical impedance measurement was taken across the multiple elements for record keeping and characterization purposes.

3.2.4 SYSTEM COMPONENTS

The completed probe was used in conjunction with other in-house fabricated components. Handles were 3D printed for minimally invasive usage and molded for an ergonomic grip that also contains enough space to attach the necessary electrical components to the endoscope. The electronic hardware and software were developed previously in the lab and are capable generating real-time high-quality images when connected to the probe.

The beamformer hardware with the co-axial cable and assembled transducer are depicted below in Figure 3.16.

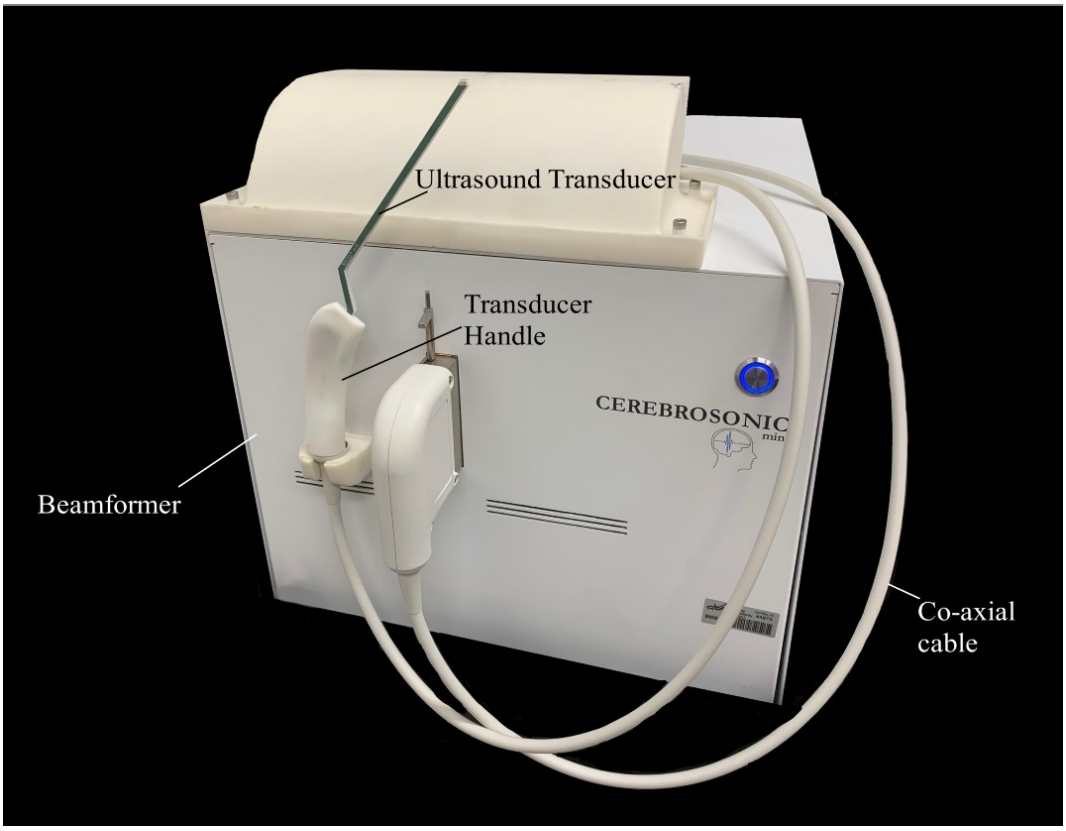

Figure 3.16 The hardware of an ultrasound system including the beamformer, co-axial cable, and ultrasound endoscope.

3.3 LAB TESTING

To demonstrate the viability of the fabricated probes, they underwent a battery of benchtop tests to characterize both their imaging performance and other attributes as an ultrasound probe. Each transducer was individually tested for safety in the lab using standards and guidelines as set by the IEC 60601 medical device standards before they were approved for use in the clinical setting. This ensures that the transducers comply with Health Canada safety regulations and minimizes potential risks to patients.

The two types of lab testing conducted can be separated into safety testing and array characterization. Safety testing can be further divided into thermal contact and acoustic testing, where the former measures the amount of heat generated on the surface of the

probe during usage and the latter quantifies the potential bioeffect risk of the acoustic beam. Performance characterization tests measured the electrical impedance, pulse echo response, and focused radiation patterns. The data obtained from the characterization tests provided a quantitative understanding of the probe's performance in areas such as resolution and sensitivity. After endoscope performance characterization and safety testing, the work proceeded onwards with pre-clinical testing. This was separated into an informal segment where scanning was performed on a volunteer's wrist within the lab setting for a preliminary characterization of the endoscope's performance, and a formal anatomy study where the endoscope was tested on an ex vivo porcine spine model.

3.3.1 SAFETY TESTING

It is paramount to test the probes for safety before considering them ready for clinical use. The three transducer tests necessary for endoscopic intraoperative ultrasound devices are thermal contact testing, mechanical acoustic testing, and thermal acoustic testing. Thermal testing was conducted across five conditions/phantoms according to the IEC standard, and acoustic testing was performed to obtain the mechanical index (MI) and thermal index (TI).

Thermal Contact Testing

Thermal testing was performed in accordance with the regulations as set out by the IEC 60601-1 and IEC 60601-2-37. In total, five different conditions were evaluated for thermal testing: still air testing, skin surface simulation, soft tissue surface simulation, soft tissue penetration simulation, and bone surface testing. System settings remained mostly consistent throughout testing, with the voltage set to ±24.5 V aside from a single bone tissue test where the voltage was set at ±26.5 V on the system. To ensure that the frame rate was at the highest possible value between 27 to 28 fps during testing to obtain the highest thermal output from the probe, additional processes that would reduce the frame rate such as Doppler were disabled. A physitemp TZAT-2LV (Physitemp, Clifton, NJ, USA) controller box with a bead thermocouple was used to obtain temperature changes with a sensitivity of ±0.05°C. All 5 testing conditions required the endoscope to continuously run for 30 minutes while the thermocouple was coupled to the probe face or

coupled to the sample adjacent to the probe face. To comply with IEC standards, the limit of the temperature increase for thermal testing is 27°C increase for still air testing, 10°C for skin surface testing, and 6°C for the bone surface, tissue surface, and internal tissue testing.

To perform the testing conditions, tissue mimicking material (TMM) blocks were used for tissue mimicry, a silicone sheet used for skin mimicry, and a piece of human skull bone was used for the bone testing. A sheath was used to cover the probe during the thermal testing process as this would be how the probe would be used in sterile OR conditions. This involved injecting a small amount of ultrasound gel into the sheath and sheathing the endoscope. During periods of non-use, the TMM blocks were stored within a sealed container filled with a 12% glycerol solution. The TMM blocks were made in-lab following the recipe as described in by the IEC 60601-2-37. Unfortunately, it was found that the evaporation of the glycerol solution brought the temperature of the TMM block below 20°C. As the standards set by the IEC 60601-2-37 had set the lower limit of the permissible starting ambient temperature to be 20°C, modifications were made to ensure that the temperature stabilized above this lower threshold for the TMM blocks. This was done by wrapping the blocks in plastic wrap which greatly reduced the surface area for evaporation. The tests were also performed within a mostly sealed container, again to reduce the amount of evaporation. Each individual trial was interspaced with sufficient time for the thermocouple to return to approximate room temperature, which was recorded at the start of the testing session.

Of the five thermal testing conditions, the only trial that didn't require a coupling medium was still air testing, where the thermocouple was placed in direct contact with the probe face through the sheath and held in place with a small amount of minimally thermal conductive adhesive. The remainder of the trials all required ultrasound gel as a coupling medium between the sample, the probe, and the thermocouple. The probe was held in place with a clamp during the trials and the cable secured to prevent the weight of it from shifting the probe during the 30 minutes time span.

For the tissue surface, skin surface and bone surface testing, the temperature of the surfaces was first evaluated with the thermocouple after the temperature stabilized, and the endoscope was then placed so that the probe face was on the sample and set before the thermocouple as shown below in Figure 3.17. The temperature was taken again after the probe was in place, and then the endoscope was excited on max settings for 30 minutes. The temperature at the end of the 30 minutes was recorded. At the beginning of excitation, it was possible to check the display to determine if the thermocouple was within the ultrasound beam. This is important as the interference of the ultrasound beam with the thermocouple would result in unwanted temperature increases from the ultrasound beam instead of the tissue.

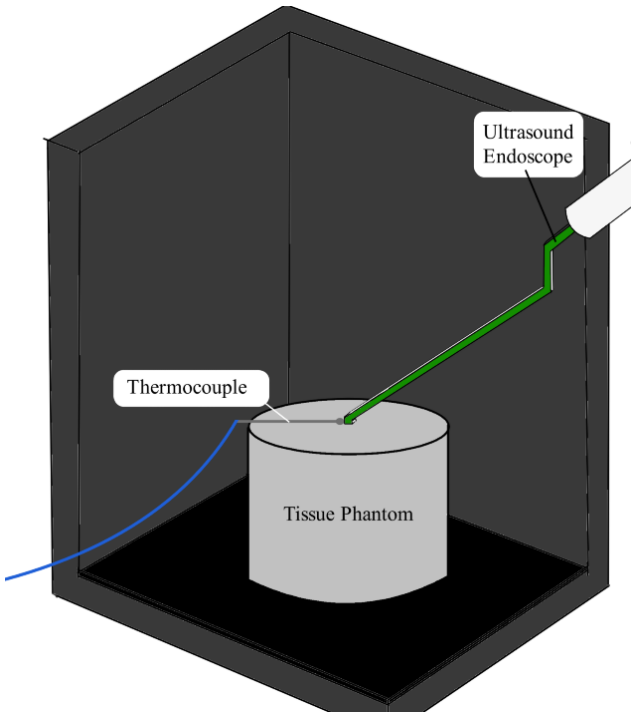

Figure 3.17 Thermal testing set-up for tissue surface testing.

The internal tissue testing was performed with two blocks of TMM: a base block with a channel for the thermocouple and a block with a channel casted within to allow the passage of the endoscope. The channel was filled with gel and both blocks had their sides wrapped with plastic wrap. The probe was carefully positioned with visual aid from the

screen display, where the desired image was a screen of tissue phantom speckle with no interference from the thermocouple.

Acoustic Testing

Acoustic testing was performed for each individual probe as it determines the endoscope's thermal and mechanical indices, both of which are limits set by the IEC 60601 standards and are usually displayed on the ultrasound system during clinical use for a sonographer's perusal.

The thermal index (TI) characterized how much temperature increases within the tissue at the focus of the acoustic beam within the tissue. This is different than the surface temperature rise previously described since TI is a numerical value proportional to the acoustic energy that gets transformed into thermal energy within tissue. This value differs within different tissues and at tissue boundaries, being the most pronounced at the tissue and bone boundary. The TI limit is not a single limit and instead is tied to a maximum scanning time with the ultrasound probe held stationary. A few examples to understand the scale used for determining how the thermal index is used would be the values of 1.0, 2.9 and 5.9. At a TI of 1.0, it is permissible to continuously scan without a time limit and without shifting the endoscope or sweeping the beam elsewhere. At 2.9, this increased index value corresponds to a shorter permissible scanning time of less than 4 minutes before the tissue heating has become significant, and at a value of 5.9 not even 5 seconds is permitted for general imaging [86]. These thresholds are further reduced in the case of neonate and obstetrics scanning, where developing fetal tissue is more sensitive to temperature changes, eye imaging, and transcranial applications. When calculating the 4 TI values of an ultrasound probe, the radiation pattern is evaluated at the breakpoint distance, or the closest possible plane to the probe where the acoustic beam is no longer unpredictable as determined from the endoscope geometry. The breakpoint distance used for the fabricated endoscopes was 2.9 mm. In comparison, the mechanical index is calculated at the focal point.

The mechanical index (MI) is a value calculated that predicts the risk of exceeding the cavitation pressure threshold. If a strong enough peak-negative pressure is reached, a

cloud of cavitation bubbles will form within the tissue and cause mechanical bioeffects [87]. Although the MI primarily correlates with the risk of cavitation, another potential mechanical bioeffect effect is streaming, albeit to a lesser degree. While the potential for cavitation depends on potential gas bodies within the anatomy, the hard limit set for MI by Health Canada and the FDA is 1.9, with the sole exception being the eye where the limit is set to 0.23 [87], [88].

Both MI and TI tests were performed in distilled water with a fibre optic needle hydrophone (Precision Acoustics, Dorchester, Dorset, UK) distanced from the endoscope face operating at full strength as illustrated in Figure 3.18. An in-lab program used three motors (Thorlabs Inc, Newton, NJ, USA) to move the endoscope across a plane perpendicular to the needle hydrophone. The data recorded by the hydrophone was displayed as radiation patterns and were obtained at the focal plane and breakpoint plane respectively.

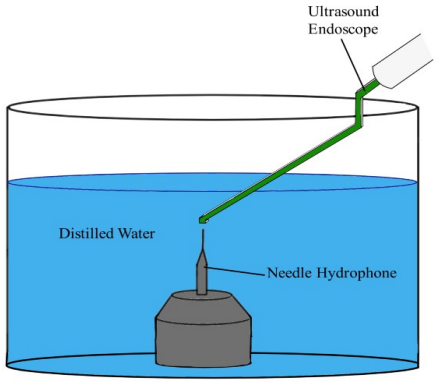

Figure 3.18 Simplified acoustic testing set-up.

3.3.2 CHARACTERIZATION TESTS

The ultrasound endoscopes were also evaluated through multiple characterization tests. In addition to the radiation patterns collected from the acoustic testing, data collected for the endoscopes also included the electrical impedance, waveform and bandwidth, resolution, sensitivity, and element crosstalk.

The endoscope's electrical impedance was repeatedly tested during the fabrication process and after fabrication was completed. The electrical impedances provided data on connectivity between elements and the PCBs, the uniformity across elements, operating frequency, and provided magnitude and phase curves that could be matched to a KLM model. Impedance analysis would take place after wire bonding, during and after parylene coating should more than one coating be required, and after the lens was cast onto the probe. The impedance curves were then compared with those modelled with the KLM model. The impedance analyzer used was an Agilent model 4294A (Keysight, Santa Rosa, CA).

The waveform and bandwidth of the probe was collected by pulsing a single element of the array at the center frequency in distilled water, reflecting the pulse off a block of quartz, and calculating the information obtained from a model MSO-X 3052A Mixed Signal Oscilloscope (Keysight, Santa Rosa, CA, USA). This test measured the bandwidth and center frequency of the signal and allowed for further calculation to obtain the axial resolution as demonstrated by [63], [89]. The resolution was determined by the temporal pulse envelope and was calculated using Equation 3.1 to reconstruct the pulse shape from the -6 dB width and centre frequency from the frequency spectrum, then transforming the pulse with a Hilbert transform and obtaining the absolute value of the new function. The resulting function is normalized and converted to a logarithmic scale where the -6 dB width in the temporal spectrum is used to derive the axial resolution [89].

$$g(t) = \cos(\omega_c t) \times e^{\frac{-t^2}{2\sigma_\omega^2}} \tag{3.1}$$

Where σ_ω is standard deviation and ω_c is the angular frequency calculated from the centre frequency.

In comparison, lateral resolution was obtained by calculating the -6 dB width angle from a wire target at the focal depth, which can be obtained from an embedded program within the imaging software. The acquired results were then compared with the Field II model.

As the final sensitivities of the probes needed to be obtained after the lens casting process, it was difficult obtaining a two-way insertion loss from an element pulse echo

since they are focused in the elevation dimension and defocused in the azimuth dimension. Because of this, it is more typical to just measure the one-way sensitivity of a focused transducer, where a hydrophone was set at the focus point to measure the peak pressure at various driving voltages to obtain a kPa/V value.

Crosstalk is characterized as unwanted signal bleed over from neighboring elements, regardless of whether the excitation is electrical or mechanical in nature. It can be affected by array characteristics such as element shape, kerf size, kerf depth, as well as the design of the PCB and the proximity of other electrical connects [90]. Overall, a lower crosstalk value is desirable, and many avenues have explored methods to lowering this value for better element directivity and preventing the degradation of single-element, angular responses [91]. Within this project, crosstalk was measured by electronically exciting a single element and measuring the signal received by the neighboring elements. As the elements of the array were designed so neighboring elements were connected to different PCBs, the closest elements would be those on the opposite PCB, and the next closest would be connected to the traces of the original PCB.

Characterization data for each individual probe will be kept within their own document data sheet for future reference, and to also maintain a record for comparison after in vivo testing to ensure that the probe has not deteriorated.

3.4 IN VIVO TESTING

The last testing component of the fabricated probes was imaging tests conducted in anatomy models. There were two aspects to this testing: first the probes were tested on the wrists of volunteers, and second, they were used to image a spine in an ex-vivo porcine model. Both testing methods demonstrated the ability to obtain relevant images and visualize anatomy.

3.4.1 IN VIVO HUMAN WRIST IMAGING

The purpose of imaging a human wrist on a willing volunteer was to obtain a preliminary understanding of how well the probe functions in a hand-held, real-time, soft tissue

scenario. This was demonstrated by seeing how well the endoscope can delineate contours, differentiate anatomy, assessing the depth penetration, and for the presence of imaging artifacts. As the wrist was a superficial scanning location, the probe did not need to be sterilized beforehand, nor did it require a sterile sheath for operation. A reasonable amount of gel was deposited over the area of interest, and the individual performing the scanning handled the probe with a thin layer gel between the probe face and skin. The operator then used the probe to visualize the forearm muscles, vessels, nerve bundles, and other soft tissues. Doppler images of the wrist vessels were also collected to demonstrate the potential of the probe in delineating and observing the small-caliber vessels with slow moving flow such as those present in the spinal cord.

3.4.2 PORCINE SPINE IMAGING

Ex-vivo testing was conducted by an experienced surgeon with a porcine spine model. The specimen was sacrificed at a local farm and the carcass was delivered to the clinic for imaging under protocol #I23-17 as approved by the Dalhousie University Committee on Laboratory Animals.

The porcine specimen was arranged in a prone position to expose the back, and the surgeon palpated for the spinous processes to locate the site for the incision. A tube was passed down the incision after separating the muscle fibers and localizing the lamina and facet joint of the chosen thoracic vertebrae. Soft tissue above the bone was removed with forceps, and the bone itself was gradually removed with various Kerrison rongeurs and Kerrison punches. During this removal process, visualization was achieved with a surgical microscope. However, due to the limitations of the surgical tools available and not having access to a burr drill to drill through the lamina, it became necessary to remove the tube and instead use muscle retractors to open a slightly larger incision site to open the lamina with the tools on hand. Portions of the ligamentum flavum was also excised with a Kerrison rongeur once exposed.

After the surgical corridor was established, saline was injected into the cavity to provide a visualization window and the sheathed ultrasound probe was used to investigate the

exposed anatomy. During the trial, it became necessary to instead use ultrasound gel instead of saline due to the saline escaping the spinal canal.

When the probe was placed in position, mimicking a standard minimally invasive surgery, anatomy was imaged such as the spinal cord, dura, the spinal canal borders, and ligamentum flavum. The collected data was saved on the beamformer hard drive as video clips marked with timestamps for later processing and retrieval.

CHAPTER 4 RESULTS

Over the course of this work, multiple ultrasound endoscopes were fabricated, each with slightly varying characteristics due to human error, deliberate changes, and machining error. Differences in the thickness of the piezoelectric elements resulted in varying resonating frequencies, ranging from 25 MHz to almost 50 MHz, and depositing an erroneous amount of parylene for the matching layer would result in matching not optimally balanced between transmission and bandwidth. Similarly, the positioning and thickness of the lens affects the sensitivity of the probe, the location of the focus, and elevational resolution. As such, it was crucial to individually characterize each completed endoscope prior to clinical usage. This work presents the results from two individual endoscopes: probe 8 and probe 9. The results presented in this chapter pertain to the outcomes of the array testing, safety testing, and anatomical imaging.

4.1 ARRAY TESTING

As described in 3.3 LAB TESTING, the ultrasound endoscope was characterized with multiple tests ranging from its electrical properties to its acoustic beam characteristics. The proceeding section will present the results of probe 8 and probe 9 and the results will be discussed in chapter 5.

4.1.1 IMPEDANCE EVALUATION

Electrical impedances were measured before and after applying a matching layer, and pre-matching the impedances were inputted into the KLM model to estimate the optimal balanced matching layer thickness. The original electrical impedances with the matching KLM overlay for probe 9 are depicted below in Figure 4.1 (a) and (b), and the resulting impedances after the matching layer was applied was once again overlaid with those modelled with the KLM model in (c) and (d). Between the impedance magnitude and phase, the measured magnitude correlated more closely to the modelled impedance. The pulse waveform after the matching layer was applied was then modelled and presented in Figure 4.1 (e).

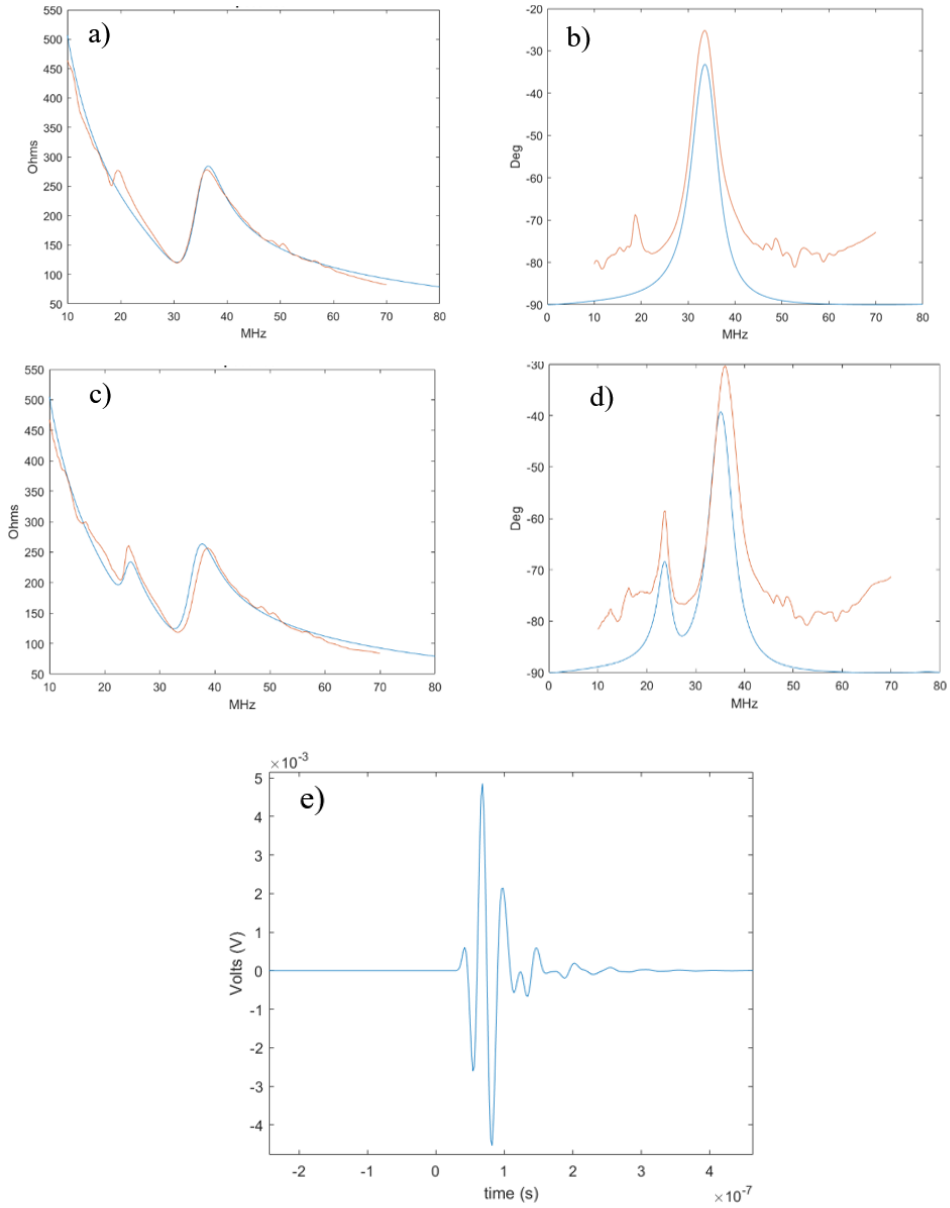

Figure 4.1 Probe 9 measured (red) and KLM program model (blue) a) magnitude pre-matching layer b) phase pre-matching layer c) magnitude post-matching layer d) phase post-matching layer and e) modelled two-way pulse waveform after matching.

Following lens casting, probe 8 had a mean max peak magnitude of 195 Ω and a mean max peak phase of -35.5°, while probe 9 had a mean max peak magnitude of 233.4 Ω and a mean max peak phase of -40.5°. Both endoscopes demonstrated proper electrical

conductivity and impedances across all elements, and an example overlay of the impedance traces from probe 9 is visualized in Figure 4.2.

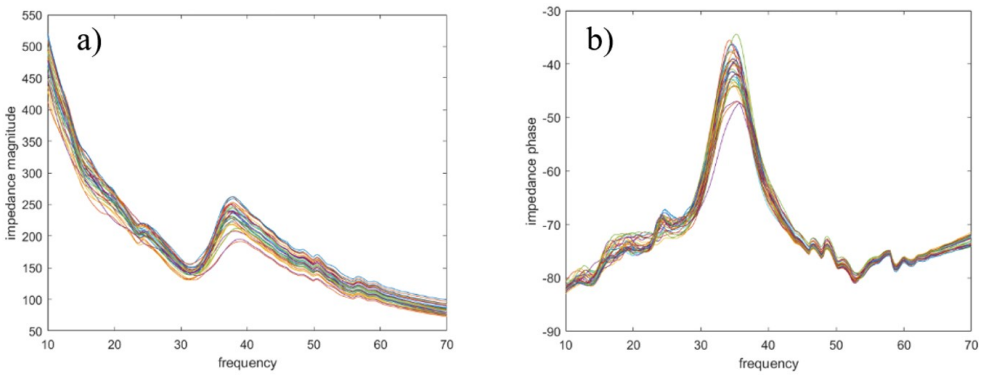

Figure 4.2 Impedance a) Magnitude and b) Phase of probe 9 across multiple traces.

4.1.2 AXIAL RESOLUTION

Both probes had their bandwidth and center frequency evaluated by pulsing a single element in the array and reflecting the pulse off a quartz flat. The receive signal was captured using a Mixed Signal Oscilloscope (Agilent Technologies, Santa Clara, CA, USA). Probe 8 demonstrated a center frequency of 29.5 MHz with a bandwidth of approximately 69%, while probe 9 demonstrated a center frequency of 25 MHz and a bandwidth of approximately 58%. The pulse bandwidth was similar to the KLM simulated bandwidth of 59.4%. Figure 4.3 provides an example of probe 9's bandwidth as evaluated on the oscilloscope, showing both the shape of the received echo pulse in yellow and the FFT spectrum bandwidth in pink at 7.8 mm from the probe surface.

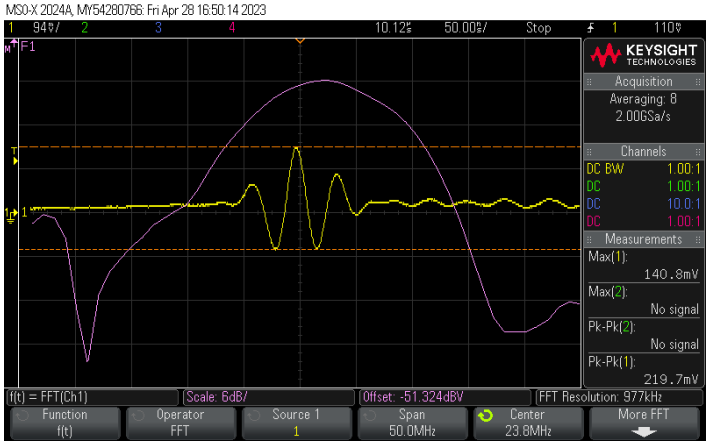

Figure 4.3 Oscilloscope screen of the bandwidth and signal shape of a single element from probe 9 during excitation.

Within the Figure 4.3, the x-axis of the frequency spectrum spans 50 MHz, while the x-axis of the temporal waveform spans 500 ms. The y-axis increments for the frequency scale are 6 dB. Using the method previously described in 3.3.2 CHARACTERIZATION TESTS, the axial resolution was calculated with the center frequency and the bandwidth, giving 33 μm for probe 8 and 45 μm for probe 9. Both acquired resolutions were worse than the predicted 32 μm of the earlier KLM model.

4.1.3 LATERAL RESOLUTION

Both probes had their lateral resolution measured by using a 15um aluminum wire target suspended in distilled water. Figure 4.4 below shows example radiation patterns obtained for probes 8 and 9 at angles of 0°, 12°, and 25°, comparisons to the modelled radiation patterns from Field II and with sign-coherence weighting factor (SCF) enabled [65]. The probes overall demonstrated secondary lobes suppressed to approximately −60 dB as shown below in (a) and (b), where the secondary lobes for enabled SCF was also demonstrated to be approximately −90 dB. After taking the −6 dB peak width from the pressure intensity graphs, the lateral resolution of the probes at the focus were measured to be 130 μm and 116 μm for probes 8 and 9 respectively. Both probes demonstrated worse lateral resolution at 0° than the 106 μm predicted by the model in 3.1.2 but fell well below the required 150 μm threshold. In addition, when comparing the measured radiation patterns of probe 8 to that of the Field II simulation at multiple angles in (c), the level of secondary lobes was comparable, although the presence of grating lobes were more prominent within the measured patterns. For further comparison of the endoscope's settings during actual use, measured patterns with SCF enabled at 25° were also overlaid with the modelled pattern in (d).

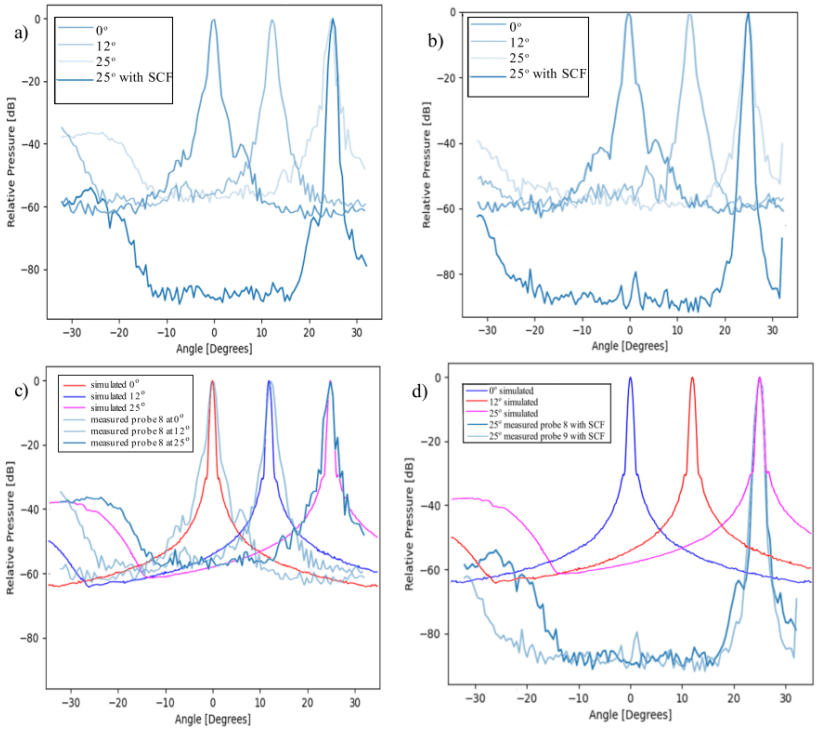

Figure 4.4 Radiation patterns found at 0°, 12°, and 25° from: a) probe 8 and with SCF enabled at 25° b) probe 9 and with SCF enabled at 25° c) Field II simulation model overlaid with measured values from probe 8 and d) simulations of probes 8 and 9 overlaid with measured values taken with SCF enabled at 25°.

4.1.4 SENSITIVITY AND CROSSTALK TESTING

The sensitivities of both probes were evaluated by measuring a range of received signal voltages when the system was driven at voltages between ±0.9 V and ±6.8 V. After adjusting the data to the kPa/V scale, when exciting all 64 elements probe 8 demonstrated a sensitivity of 168 kPa/V while probe 9 demonstrated a sensitivity of 272 kPa/V. Crosstalk was evaluated for randomly chosen elements on both probes. On probe 8, on average the crosstalk from the neighboring element of the same PCB was -27.1 dB, the next neighboring element was -27.9 dB, and the first neighboring element on the opposing PCB was -27.5 dB. In contrast, the average crosstalk on probe 9 from the neighboring element of the same PCB was -27.0 dB, the next neighboring element was -27.5 dB, and the first neighboring element on the opposing PCB was -26.3 dB. Further elements did not demonstrate a significant signal.

4.2 SAFETY TESTING

Thermal and acoustic testing was performed for both endoscopes to evaluate the potential of heating or other bioeffects when used endoscopically. The data for the tests are summarized below in Table 4.1, where the first column provides the safety limit as set by the IEC, FDA, or Health Canada, and the latter columns document the values obtained for the endoscopes. As the threshold values for thermal testing exist in a range, both the maximum allotted threshold and the minimal threshold of concern are documented in the table. The TI values were also separated into four categories corresponding to the boundaries. During the tests, the transducers were driven at three different levels: the MI and TI had the highest driving voltage of 28.2V, probe 8 was driven at 26.5V for the bone thermal test, and the remainder thermal tests were all conducted at 24.5V and this was set as a hard limit that the system may not exceed.

Table 4.1 Safety testing results

Test	Limit	Probe 8	Probe 9
Still air testing	27°C	12.5°C	8.9°C
Bone surface	6°C	5.9°C *	5.5°C
Skin surface	10°C	4.3°C	5°C
Tissue surface	6°C	4.1°C	4.5°C
Internal tissue	6°C	2.3°C	1.9°C
MI**	1.9	0.961	1.2336
TI (soft tissue, at surface) **	6 (<1 is negligible)	0.302	0.380
TI (soft tissue, below surface) **	6 (<1 is negligible)	0.301	0.380
TI (bone, at surface) **	6 (<1 is negligible)	0.689	0.878
TI (bone, below surface) **	6 (<1 is negligible)	0.301	0.380

*used ±26.5 V instead of ±24.5 V

**used ±28.2 V instead of ±24.5 V

4.2.1 THERMAL TESTING RESULTS

As the thermal testing trials were performed over several days, the ambient room temperature varied between trials from 22.4°C to 22.9°C. The bone testing for both probes were done on a separate day than the other thermal testing trials. The skin surface and tissue testing both used a cylindrical TMM block. The internal tissue testing used a cube shaped TMM block with a smaller, hexagonal block with a channel molded to the transducer to model the passage. The still air testing trial was conducted with the endoscope sitting on the beamformer's probe holder to best model the temperature increase that occurs when the probe is on but not in use, and the remaining trials were conducted in a large container with the top enclosed with a thin film of plastic to minimize air flow and evaporation in the container. All thermal test results remained under the required threshold, and while the bone test for probe 8 reached a 5.9°C increase, the subsequent tests were conducted at a lower voltage and the system from then onwards was hardcoded to the decreased voltage output. The test conditions also represented worst possible conditions for heat build-up, as clinically it is not expected for the endoscope to ever have to image the same structure continuously for 30 minutes while stationary in conditions contrived to minimize cooling by evaporation.

4.2.2 ACOUSTIC TESTING RESULTS

Radiation pattern slices were obtained after the ultrasound beam was adjusted to an acceptable angle perpendicular to the motor axis (within 5°). Probe 8 had an angle deviation of approximately 4.4° and probe 9 had an angle off beam axis of 0.4°. The dimensions of the radiation planes were determined by the range where the signal detected by the hydrophone has dropped by a given amount: -6 dB for the focus, and -12 dB for the breakpoint plane. The patterns were obtained for both probes, where Figure 4.5 (a) and (b) show the pattern at the breakpoint plane for probes 8 and 9 respectively, while (c) and (d) provide the radiation pattern at the focal plane. The data was imported into MATLAB for further calculation of the TI and MI values as well as the acoustic working frequency. The measured MI and TI values are recorded above in Table 4.1.

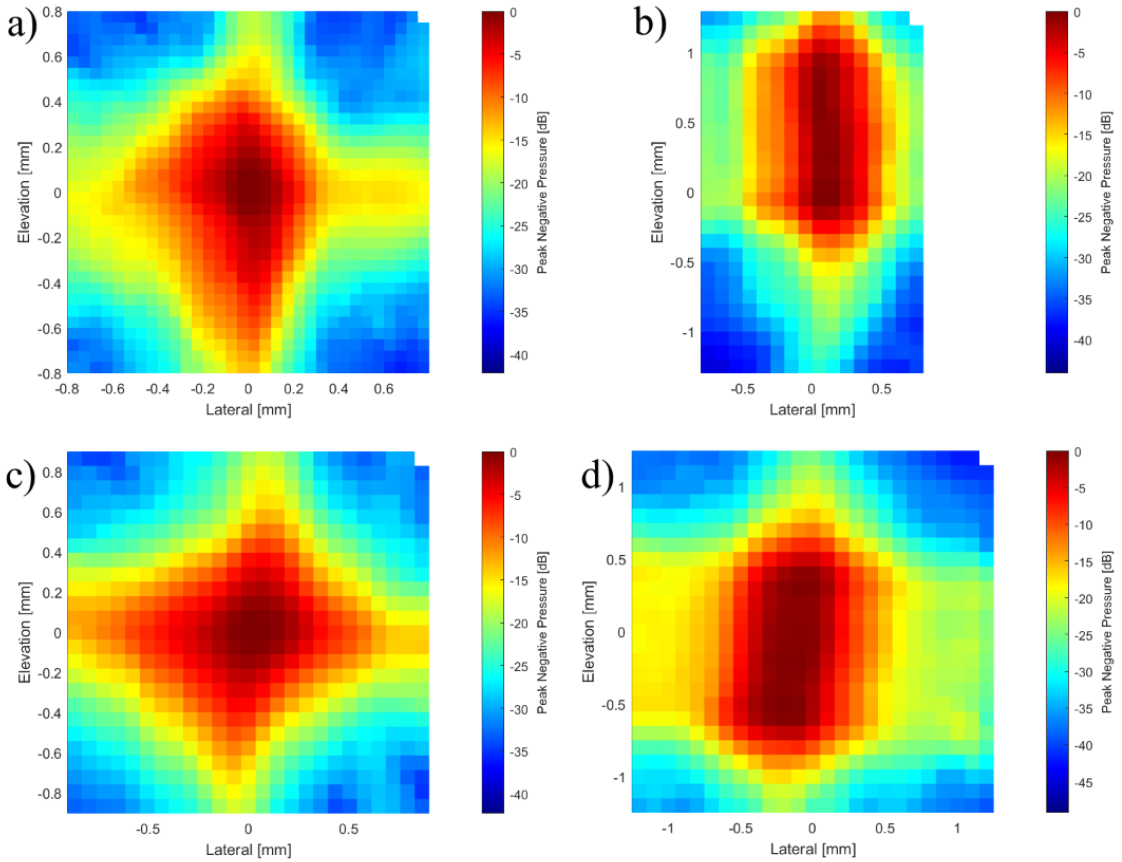

Figure 4.5 Radiation patterns measured with a hydrophone for acoustic testing. a) probe 8 MI at focal plane b) probe 8 TI at breakpoint plane c) probe 9 MI at focal plane d) probe 9 TI at breakpoint plane.

4.3 ANATOMICAL TESTING

Numerous clips and images were obtained from the two anatomical imaging tests to demonstrate both the image quality of the probe and proof of concept spinal cord imaging. The first testing was on a volunteer's wrist and the latter with an ex vivo porcine spine model. The endoscopes were tested at a transmit voltage setting of ±28.2 V.

4.3.1 WRIST IMAGING

The images in Figure 4.6 were taken of a human volunteer's wrist using the real-time B-mode and Doppler software. The area scanned was the radial side of the forearm and proximal to the palm with the probe held by hand. The images were taken in both

transverse and sagittal orientations, demonstrating nerve bundles, vessels, muscles, skin, and other soft tissue fascia. The imaging depth was 15 mm, and Doppler imaging was obtained when imaging the vessels.

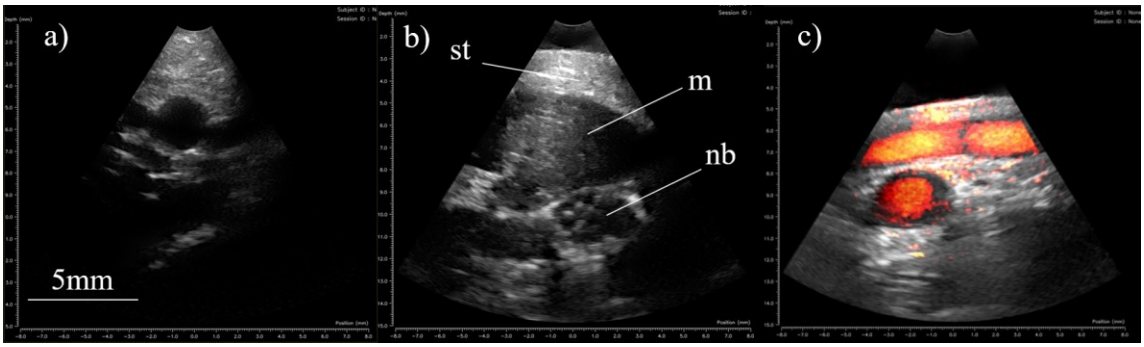

Figure 4.6 Images generated of a human wrist: a) Transverse view of wrist featuring three vessels b) transverse view of the wrist featuring muscle (m), subcutaneous tissue (st), and a nerve bundle (nb) c) power Doppler image of a deep transverse vessel and a superficial sagittal vessel in the forearm.

In the brightness mode images (B-mode), the vessel walls were clearly delineated in (a), where a superficial wrist artery is seen down the center at a depth of approximately 5 mm accompanied by two veins lateral to either side. The vessel walls are hypoechoic, and the vessel lumen appears anechoic. In Figure 4.6 (b), the hyperechoic skin layer is depicted towards the top of the screen, as is the subcutaneous tissue directly deep to it. The muscle appears hypoechoic with characteristic striations, and two nerve bundles can be seen deep to the muscle. The nerve bundles are cushioned by connective tissue and appear hypoechoic with multiple small anechoic circular regions within. In Figure 4.6 (c) where power Doppler is demonstrated as the red-orange coloring, there is tissue motion artifact occurring outside of the vessels, but the superficial vessel that runs sagittal through the image demonstrates fill even at a vessel diameter of less than 2 mm.

4.3.2 PORCINE SPINE TESTING

To emulate how the probe would be used on human spine imaging, a minimally invasive muscle splitting tubular retractor was used by the spine surgeon in an attempt to access the spinal column similar to that approach used in the OR. Figure 4.7 shows the steel tube along with the probe. The probe size was demonstrated to easily fit in the tube with room to spare for both optical microscope guidance and potentially an additional surgical tool.

As mentioned in the methods section, as it was difficult to remove the bone without a burr drill, the tubular retractor was removed and the surgical access channel was opened an additional amount in order to remove about 5-7 mm of the lamina bone so that the spinal cord could be accessed.

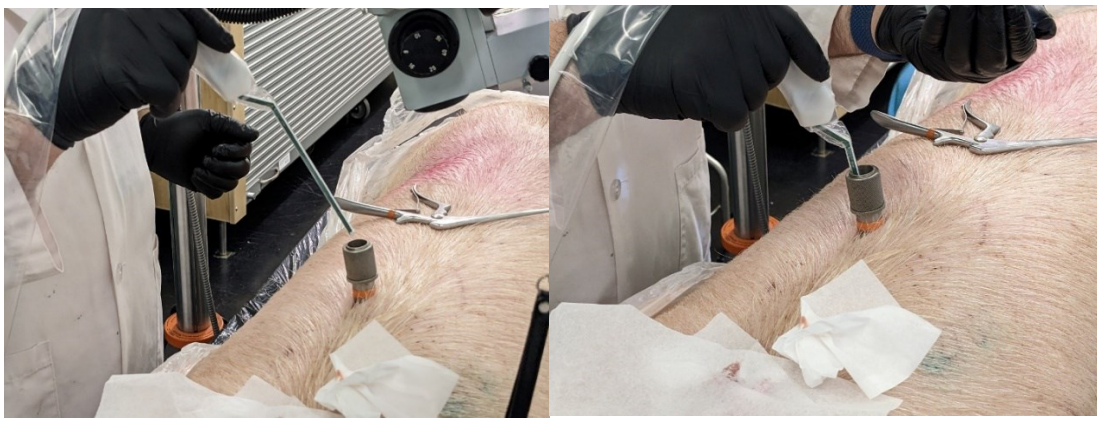

Figure 4.7 Ex vivo porcine spine imaging with an inserted steel tube where a) the probe is held above to compare the probe tip to the entrance of the tube and b) the probe has been lowered into the tube.

Multiple video clips were obtained from the porcine trial, which were then browsed for shorter clips and still frames that best outlined key features. The images below in Figure 4.8 are taken from probe 9's imaging run, as probe 8 obtained comparatively suboptimal images due to lower sensitivity. Most of the images are in a transverse (TR) orientation, with only a single image taken in a sagittal (SAG) orientation.

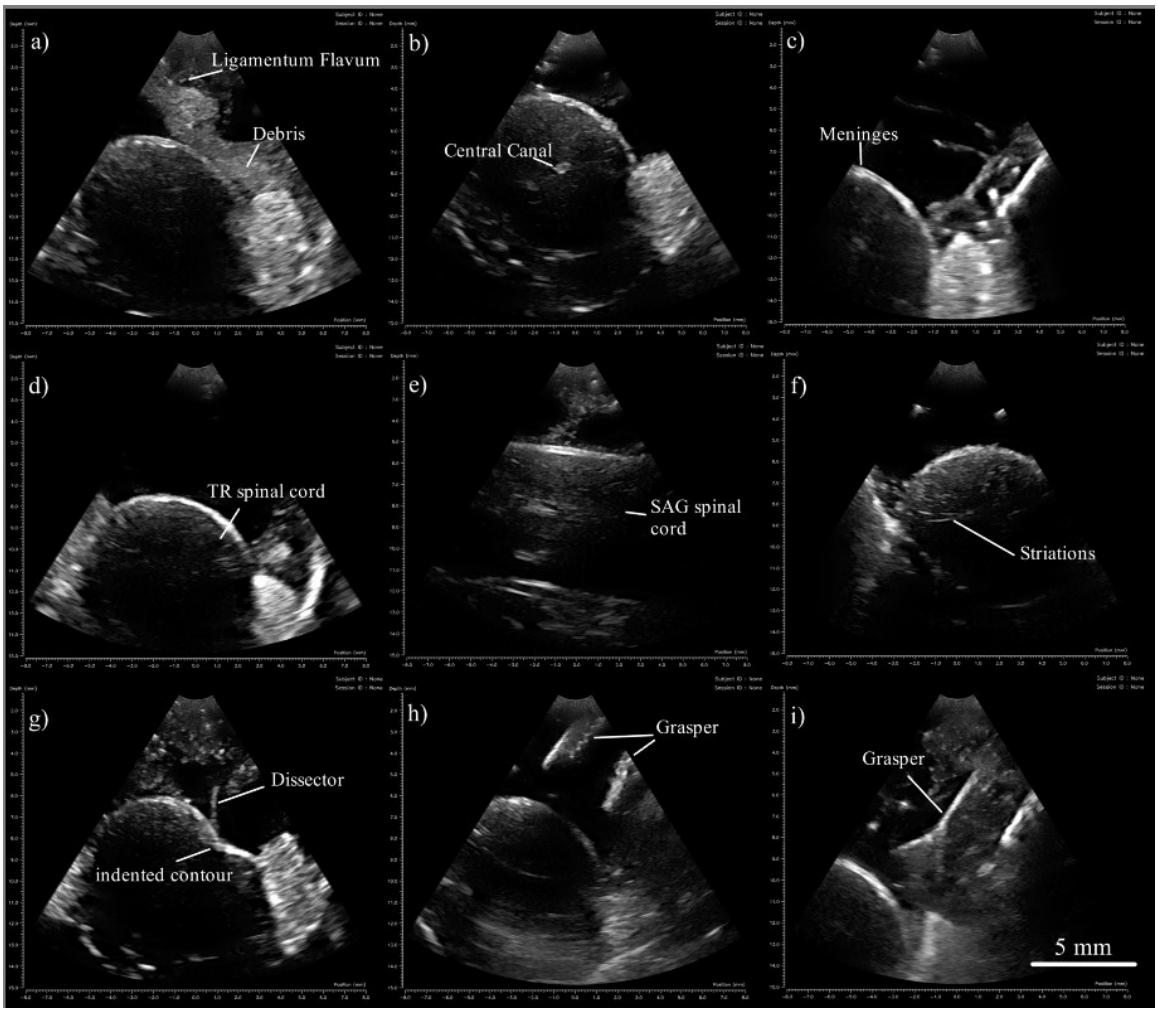

Figure 4.8 Ultrasound images of: a) TR spinal cord with anterior ligamentum flavum and tissue debris b) TR spinal cord with visible central canal c) partial TR spinal cord showing fine structures in the anechoic region d) TR spinal cord e) SAG spinal cord with central canal visible f) echogenic striations within TR spinal cord g) indented TR spinal cord contour from a dissector h) TR spinal cord with forceps in image i) TR spinal cord with smaller graspers in plane.

Multiple anatomical landmarks within the spinal canal were imaged in the study as illustrated above. In Figure 4.8, (a) demonstrates a general view within the spinal canal, where the dorsal contour of the spinal cord is well delineated and a heterogenous, mostly echogenic mix of debris and ligamentum flavum can be perceived within the anechoic region superior to the spinal cord. An echogenic structure lateral to the spinal cord is also demonstrated. In (b), the spinal cord is examined in a more superficial manner, with less debris and ligamentum flavum superficial in the imaging window and details less

shadowed within the spinal cord itself. The central canal of the spinal cord is also visible in this image. Image (c) presents a thin anechoic delineation within the contour of the spinal cord contour and demonstrates the axial resolution of the endoscope through thin, echogenic strands within the anechoic space. Image (d) demonstrates the anechoic space free of artifacts and debris, and (e) presents a sagittal view of the spinal cord including the meninges and the central canal. Image (f) then provides another visualization of the transverse spinal cord, where echogenic strands were seen within the cord itself. Image (g) is the first view demonstrating a noticeable indent in the spinal cord's contour, where a surgical tool is out of frame and palpating the structure, and this is followed by image (h) and (i) where two different graspers are in frame.

CHAPTER 5 DISCUSSION AND FUTURE CONSIDERATIONS

This work encompassed the design, fabrication, and testing of an angled, high frequency, ultrasound endoscope tailored for MISS. It was designed based on the requirements of a minimally invasive surgical tool for this application, and the ultrasound array fabrication was similar to a previously developed endoscope for neurosurgery. Testing was performed for both array characterization purposes and exploring the endoscope's capabilities when scanning anatomy. This section includes a discussion on the fabrication and testing stages as well as the images generated with the endoscopes.

5.1 DESIGN AND FABRICATION

By employing the techniques used by [79], [81] in the fabrication of the endoscope, the characterization and imaging tests demonstrated that viable angled, high frequency endoscopes can be produced in this manner. However, aside from the successful probes fabricated over the duration of this project, there were multiple variables that resulted in inconsistencies and difficulties during the fabrication process. Therefore, this section will focus on discussing the differences between fabricating probe 8 and 9, and the difficulties that were encountered during fabrication.

5.1.1 DIFFERENCES IN FABRICATED PROBES

Although only probes 8 and 9 were evaluated through the full battery of tests for this work, there were six probes that were fabricated prior as probe 7 did not exist. Of these six, only three reached the fully completed stage where image acquisition was possible. Table 5.1 below summarizes the issues faced by the earlier endoscope models. The most common issue occurred in the array fabrication process, where the frequency was outside of the acceptable range even though the endoscope would still be imaging capable, as this would result in inadequate penetration. Another more severe issue that could occur would be during the mounting process where elements may be damaged or shorted. In addition, errors during or after lens casting may result in delamination of the lens, which may also damage the matching layer underneath.

Table 5.1 Unsuccessful probes.

Probe number	Issue
1	Imaging capable, but frequency too high
2	Lens delamination
3	Shorted elements
4	Misalignment during mounting
5	Imaging capable, but there were broken traces
6	Imaging possible, but the frequency was too high and issues had occurred during lens casting

In contrast to the unsuccessful probes, the largest difference between probes 8 and 9 was the thickness of the piezoelectric substrate. While probe 8 aimed for elements in the 52 μm thickness range, the array fabricated for probe 9 had a higher thickness of approximately 54 μm. This directly affected the operational frequency, where probe 8 operated at 29.5 MHz and probe 9 at 25 MHz. This deliberate decrease in frequency was to evaluate the difference in scanning quality of deeper anatomy, which while not as visible during wrist scanning, was made more evident in the porcine cadaver as will be assessed in 5.3.2 PORCINE SPINE.

The two probes also differed in their matching layers. First due to their operational frequencies, probe 9 would require a thicker matching layer to contend with its longer wavelength from its lower frequency, and because during the deposition process an excessively thick layer had been unintentionally deposited onto probe 8. Probe 9 encountered the opposite issue, in that the matching layer deposited turned out thinner than the amount calculated to be optimal by the KLM model. Although not by a significant amount, there was some reduction in bandwidth.

5.1.2 FABRICATION DIFFICULTIES

As [81] provided a comprehensive overview of transducer fabrication, the most prominent issues in the fabricating of the angled, long-necked probe occurred due to dimensional changes. These issues stemmed from two reasons: most of the lab equipment being tailored for fabricating and assembling probes of a shorter length, and the angle presented difficulties for alignment of the stack and the lens cast.

The length of the probe was too long for the space beneath the wire-bonding machine, which reduced maneuverability and the overall capability of being able to wire bond the array to the PCBs. This was solved by changing the original single, long 3D print of the probe to two smaller pieces, where the PCBs and array would be first attached to the shorter, tip print. With only a portion of the probe neck held immobile by the 3D print, the remaining excess length of the PCBs could be bent to reduce the overall height, allowing it to fit within the constraints of the wire bonder as illustrated previously in Figure 3.11. As such, the two-piece design of the probe's 3D print was a solution to the long length of it unable to fit within the wire bonder during the early stages of assembly.

It was during lens casting that the major fabrication hinderance occurred. The lens material used for the endoscopes begins as a slightly viscous, colourless fluid, and it was deposited into a concavity created by a silicone mold around the probe tip before a Teflon rod with the correct curvature was nestled upon the mold. The material was then cured using heat and pressure over a period of hours. While this normally does not pose any issue, the angled shape of the tip of the probe required a new custom-cast mold that incorporated the bend at the tip. This required a few versions of printed molds to complete, and even the final version did not completely compensate for the endoscope's beveled edges, much less the slight variations at the head of the probe due to the topography differences from the epoxy. This further held true during the curing process, as the angle must be maintained so the probe face is facing upwards to prevent the resin from seeping out while the lens cured. To ensure that the maximal amount of resin remain within the mold for a successful casting, an angled holder addition was printed to be attached to the pre-existent straight endoscope holder. However, even with the holder in

position, the diameter of the pressure chamber was just barely sufficient for the length of the probe as pictured in Figure 5.1. Alternative methods such as tilting the chamber and keeping the entire structure stable on a hot plate were considered should the diameter prove to be insufficient, but ultimately discarded as the angled base was just wide enough for a lens casting.

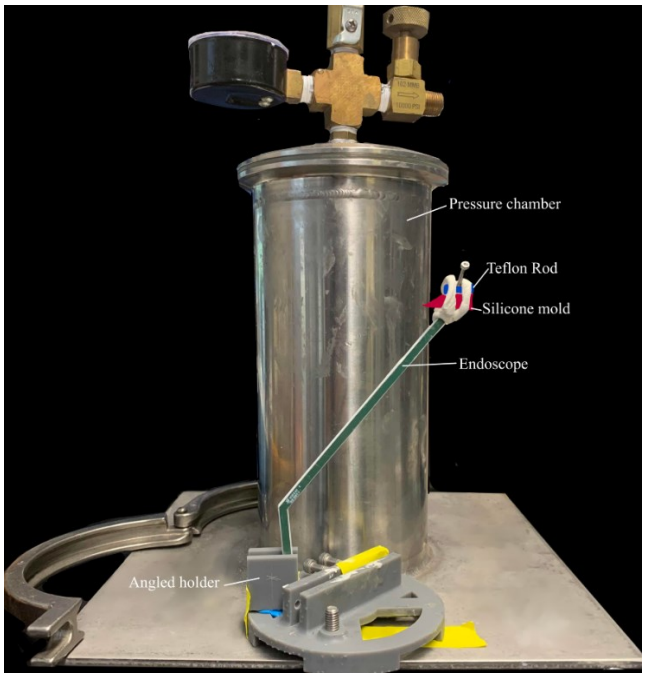

Figure 5.1 Lens casting set-up and pressure chamber.

5.1.3 FABRICATION CONSIDERATIONS FOR THE FUTURE

Multiple endoscopes reached the final testing stages, but to improve the odds of successfully fabricating this angled, long necked variation a few improvements may be considered for the future.

To optimize the matching layer, it may be beneficial for the KLM model to first re-pole the endoscope prior to acquiring the impedance data. While this wasn't done for the completed probes, it was advised to be added as a future step. Due to the temperature that the piezo substrate experiences during mounting, sputtering, and laser cutting, the substrate's piezoelectric properties decrease. Repoling it may result in better piezoelectric properties and therefore imaging performance.

In addition, while both using a calibration slide and measuring the actual thickness layer of the probe can be beneficial towards assessing the current amount of parylene deposited, they come with different drawbacks. Using a calibration slide allows the endoscope to be held in the same position throughout both the original and the top-up run, which reduces deposition thickness variations due to how parylene thickness varies depending on the height and distance from the center of the chamber. However, it is limited by how accurate the calibration slide is, as the thickness of parylene on the slide also depends on the placement location in all three dimensions. In comparison, while re-evaluating the probe's impedance curves can produce a more accurate assessment of the amount of deposited parylene, it runs the risk of repositioning the endoscope during the second run that would affect the accuracy of the calibration constant produced by the first run as well. Fortunately, there is a given amount of leeway for the matching layer's thickness by ±1 μm, and thus the choice of how to calculate the amount of parylene for the top-up run would depend on the personal preference.

Finally, to better account for the angled tip of the probe, it may be beneficial to print more angled probe holders or grips to assist in the positioning process. They may be used during assembly, during deposition of the matching layer, during lens casting, and more, providing further consistency between endoscopes.

5.2 ARRAY CHARACTERIZATION

A plethora of tests were performed to characterize the completed endoscopes. The results included those for impedance measures, bandwidth, operating frequency and axial resolution, lateral resolution, secondary lobes and grating lobes, endoscope sensitivity, and element crosstalk. As two probes were tested, they can also provide a point of comparison.

Both probes had their impedances evaluated after the final lens casting, resulting in the impedance magnitude and phase charts in Figure 4.2. At the time of evaluation, all the elements demonstrated proper connectivity, and were relatively regular across each probe. While deviations between elements existed, they can be attributed to a slight

variation in element height, width, and any other defects that occurred during the fabrication process.

When assessing for bandwidth and operating frequency, probe 8 demonstrated a wider bandwidth of 69% and a higher centre frequency of 29.5 MHz than probe 9, resulting in an axial resolution of 33 μm in comparison to probe 9's 58% bandwidth, 25 MHz frequency and decreased resolution of 45 μm. Probe 9's axial resolution being worse than probe 8 was to be expected as probe 8 had both a higher frequency and larger bandwidth, and this likewise held true for how the probes measured up to the model. While both probes demonstrated a similar or larger bandwidth than the modelled 59.4%, the resolution based on the pulse envelope was worse than the simulated 32 μm as both had lower frequencies than the model's 32.3 MHz. Probe 8 was worse by 1 μm, while probe 9 was worse by 13 μm. However, the lower axial resolution is understandable when considering that probe 8 was operating 2.8 MHz lower than the model and probe 9 was 7.3 MHz lower. Even with both probes demonstrating a slightly worse resolution that the simulation, they both more than fulfilled the resolution requirement of less than 150 μm.

The lateral resolution was analysed by imaging a wire target suspended in water and producing radiation patterns that also provided information on the secondary lobes and grating lobes. While both probes were measured to have worse lateral resolution than the model, they still followed the models closely, and potential reasons for discrepancy would include using a wire target instead of a point target and misalignment of the endoscope. At 0°, Probe 8's lateral resolution measured 130 μm, and probe 9 measured 116 μm in comparison to the model's 106 μm. The results were still sufficient as per the goal of 150 μm, and due to decreased lateral resolution at larger steering angles, both probes demonstrated a sufficiently high resolution at 0°. When examining for the presence of secondary and grating lobes, an important distinction to make between the models and the actual measured values would be that SCF would be enabled during actual scanning. Therefore, while the probes without the presence of SCF demonstrated secondary lobes around -60 dB as well grating lobes that exceeded -40 dB per Figure 4.4 (a), enabling SCF weighting significantly improved all these attributes. This was especially evident in Figure 4.4 (d), where the SCF enabled measurements for both

probes were compared to their modeled counterparts, and the SCF measurements demonstrated lower secondary lobes and significantly reduced grating lobes. When SCF weighting was enabled, it also appears that probe 9 was superior in both how low and how far grating lobes were pushed in comparison to 8. However, this overall demonstrated the fact that while the physical probe attributes themselves may not match up to the models, by enabling SCF it would more than make up for the shortcomings.

Evaluating the endoscope sensitivity was a task made difficult by the presence of the lens already casted onto the probe. Generally, two-way ultrasound sensitivity can be evaluated through an insertion loss measurement made by measuring a pulse echo off a reflector very close to the transducer (without beam diffraction) [92]. Due to the presence of the lens with a focus at depth, insertion loss is difficult to measure as a reflector can not be placed close to the transducer. Therefore, a one-way focus was used to measure sensitivity. The entire array was transmit focused using varying driving voltages and a hydrophone was used to capture the strength of the signal at the points of focus. The obtained values for probe 8 and probe 9 were 168 kPa/V and 272 kPa/V respectively, a significant difference between probes. As a high sensitivity is desired, it is evident that in this regard that probe 8 is inferior to probe 9. The sensitivity difference of the transducers can be explained by variations in 1) lens thickness, 2) operating frequency, and 3) slight piezoelectric depolarization.

Finally, the crosstalk was evaluated for both probes, where two elements were randomly chosen on each probe for the measurement. Both probes demonstrated a similar level of crosstalk, where the nearest elements to the tested element on the same flex demonstrated an average of -27.0 dB, the next furthest demonstrated -27.7 dB, and the nearest element on the opposite flex demonstrating -26.9 dB. Further elements overall did not demonstrate significant crosstalk. Despite the consistency between the probes and the elements, the crosstalk desired between ultrasound elements in conventional ultrasound arrays is -30 dB or lower. As the levels between the two endoscopes were similar, it can be assumed that the cause would likewise be shared between the endoscopes. As such, potential reasons for the higher than estimated levels of crosstalk would be small kerfs between elements as well as the proximity of the traces within the PCBs itself. Further

exploration onto this topic would be beneficial towards pushing the levels of crosstalk down further as high levels of crosstalk would degrade image quality by affecting properties such as the acoustic beam's ring down time, the pulse-echo response, and causing array beamforming artifacts [90], [91], [93].

5.3 SAFETY

In the designing and fabrication of biomedical tools to be used in surgeries, it is of utmost importance to ensure that they are safe for the patient. In the case of this ultrasound endoscope, these guidelines would be set by the IEC, Heath Canada, and the FDA. The tests required to determine the safety of the endoscopes are the acoustic and thermal tests, one performed to evaluate the potential acoustic and thermal bioeffects, and the other for temperature change aside from being directly within the field of scanning. The electrical system itself had already been previously approved for use as it was shown to meet safety requirements. The results from the tests will be discussed in the order they were obtained, and the encountered challenges will also be discussed.

5.2.1 SAFETY TESTS

As had been demonstrated in 4.2 SAFETY TESTING, both probes passed the safety tests. However, there are a few points that are worth mentioning pertaining to the testing process, as well as evaluate the obtained results.

Chronologically, the radiation tests for TI and MI occurred first and was driven at ±28.2 V. The hydrophone testing for acoustic testing was mainly complicated by the angled tip. While 40° is a known angle, minute variations in how level the array sat on the 3D print, as well as the presence of a minute bend where the two 3D prints connect during curing affected the exact angle of the face. As such, an additional probe holder compensating for the bend and the length had to be designed and printed for the testing apparatus.

When evaluating the values obtained for TI and MI, it was demonstrated that probe 9 had significantly higher values than probe 8, which followed a similar trend to that of probe

9's sensitivity being higher than that of 8. This therefore supports the potential that probe 9 overall demonstrates a higher output signal than probe 8, which despite its weaker axial resolution and bandwidth may mean that it can still prove to be a better scanning transducer than probe 8. Additionally, both probes stayed well within the limits set by the IEC and FDA for the TI and MI. While the TI values are present for four conditions involving different tissues and interfaces, both probes had their highest values within the four categories at the bone interface, which is likewise expected. Even at the bony interface with tissue, the probes didn't demonstrate a TI value that exceeds 1, which would be the first threshold that would impose a scanning time limit upon the endoscopes when bony tissue is within the sound beam's limits. For MI testing, neither probe breached the limit of 1.9, although probe 9 managed to reach just over 1.2. These values demonstrate that both endoscopes are safe for scanning all manners of anatomy, aside from eyes, when the system is operating at ±28.2 V. Additionally, as the max voltage that the endoscopes can be operated by was decreased following the thermal tests, it can be safely assumed that the values of MI and TI would be even lower.

The thermal contact tests were conducted afterwards, and there were significantly more obstacles as compared to the MI and TI tests. When considering the thermal contact tests, a total of 5 different tests were conducted for the endoscopes. Still air testing, skin surface testing, tissue surface testing, internal tissue testing, and bone surface testing. Of these tests, the still air testing is the most lenient with a temperature increase of 27°C set as the limit, whereas skin surface is 10°C and the remainder are 6°C.

The thermal tests conducted at the original driving voltage of ±28.2 V proved to be too high and resulted in a temperature increase that exceeded the bone surface test limits. As this had occurred with the bone surface trial for probe 9 after completing the tissue surface, skin surface, and internal tissue trials with no issue, it was determined that the remainder values would continue to remain within limits if the voltage was lowered for the bone surface test. For probe 8, it was shown that lowering the voltage to ±26.5 V was just sufficient to not reach the 6°C threshold, but the power exceeded the threshold once again for probe 9. It was only by reducing the voltage output to ±24.5 V that the bone surface testing for probe 9 also fell within limits, and the remainder soft tissue, tissue

surface, and still air tests were all repeated for the two probes. Even through the probes now fall within the safety limits, users should avoid having the probe face in prolonged contact with bony surfaces. While the bone surface testing was not originally an IEC requirement for these endoscopes and were only included as an additional precaution, the outcomes of the test nonetheless resulted in a decreased output that would decrease imaging sensitivity.

5.2.2 SAFETY TESTS ADDENDUM/OBSTACLES

As per the IEC thermal testing requirements, the ambient starting temperature must be above 20°C. This was not anticipated to cause any issue as the ambient room temperature within the testing room ranged approximately between 22 and 23°C. Still air testing proved to be simplest, and no issues were seen. However, further trials with the bone, TMM, skin, and penetration tests all demonstrated complications due to the temperature of the phantom surface decreasing rapidly until gradually approaching an equilibrium significantly below 20°C. Again, as per the IEC standard, the starting equilibrium temperature must be 20°C or higher. Thus began the task of determining why the temperature decrease was occurring, and how to best reduce or negate this.

The first observation was that the amount of air flow around the phantom could cause differences in temperature stabilization. This was then negated by performing the test within a small, clear container on a lower shelf of a desk where air flow would be minimized. However, the temperature drop continued to occur, albeit not as dramatic as seen previously, and the continued decrease was then hypothesized to be due to the TMM block itself. New TMM blocks were created. While this did not provide the desired effect of negating the temperature change, the new blocks were better form fitted to the probes that were to be tested.

It was then theorized that the temperature decrease might be due to the evaporation of the ultrasound gel, and testing demonstrated that uncovered gel left out at room temperature would indeed decrease past the 20°C threshold. As evaporation is an interaction between a liquid surface and air, potential solutions included reducing this surface area, such as through plastic wrapping the structures, by restricting airflow, and by ensuring that the air

is sufficiently humidified from alternative sources. This proved to be sufficient in later trials, as the equilibrium temperature settled between 20°C and 22°C when the container was covered with a plastic film, the exposed areas of the samples wrapped in plastic wrap, and open containers of water were placed within the testing container.

5.2.3 ULTRASOUND STERILITY

To use a medical instrument during surgery, a requirement is sterility to avoid the risk of exposing the vulnerable patient to pathogens. The predecessor to this angled, small form factor spinal probe was a neuro-endoscope fabricated with a silicone coating to allow sterilization by an outside and approved facility. However, the silicone had several drawbacks including difficulty in the application, attenuation of the ultrasound, and the discontinuation of the specific brand of silicone used. In addition, the sterilization process itself is expensive to get certified by a third party. As such, this probe instead used a custom designed sterile sheath approved for neurosurgical usage. A sheathing protocol was compiled to prevent accidental cross-contamination between sterile and non-sterile entities in the OR, and the sheath was tested for leaks under a series of tests. The sheath is designed with two different polymers, a softer polymer near the probe tip and handle and a stiffer one for the remainder of the cable. Unfortunately, as the junction between the two polymers was not fluid-tight, it was necessary to devise a plan wherein a Tegaderm film was carefully used to fold away the seams. The patched sheaths were then tested for leaks, and demonstrated to be watertight even under pressure, even as it is not anticipated that there will be pressure of any kind at the level of the junction.

Similarly, the sheaths were also tested for integrity, where gel was inserted into the sheath tip and the ultrasound probe inserted to observe for any leaks from the increased pressure. The sheathed probe was then used to perform mock examinations within a skull model, and the tests were only deemed adequate if no beading of gel is observed on the outside of the sheath post usage.

5.3 IMAGE EVALUATION

Two types of imaging tests were conducted on anatomy: on a live human wrist and on a cadaveric porcine spine. Both tests provided a plethora of clips and images and were useful in demonstrating different aspects of the probes. Unfortunately, due to this work being recorded in a static media meant for eventual printing onto paper, it was not possible to demonstrate the excellent temporal resolution of the clips, nor the anatomical details that are captured more readily in clips compared to still images.

5.3.1 WRIST IMAGING

The human wrist was chosen for a few different reasons: it is simple for the person performing the scan to image their own wrist in multiple planes, the anatomy is both superficial and sufficiently complex to demonstrate a variety of anatomical structures, and the superficial vessels present allows the use and evaluation of Doppler. Within the 15 mm depth window of a scan of the wrist, it is possible to observe and assess the sonographic appearance of muscles, the skin layer, subcutaneous tissues, tendons and ligaments, blood vessels, peripheral nerve bundles, and more.

Each image from Figure 4.6 demonstrates either a different capability of the endoscope or the visualization of a different aspect of anatomy. From anechoic vessels visualized in transverse, to nerve bundles under layers of muscle, skin, and subcutaneous tissue, to the capability of the system to capture blood flow in vessels less than 2 mm in diameter with the endoscope, the wrist scanning component was very useful in outlining some of the endoscope's functionalities.

To be capable of outlining a vessel in both sagittal and transverse with a clear lumen, the endoscope would require sufficient elevational resolution to not catch out-of-plane anatomy within the image and have a noise floor low enough that the dynamic range can depict the anechoic lumen of the vessel. To be capable of imaging the details of a nerve bundle deep to muscle and skin and other tissues would require sufficient penetration, as the nerve bundle was situated at 10 mm on the image, and even deeper structures are visible albeit to a lesser degree. Being able to define the hypoechoic spots within the

nerve bundles that are presumably the nerve axon bundles themselves wrapped in connective tissues demonstrates sufficient resolution at that depth, although the clear contours of the nerve bundle might be better evidence in support of the resolution. Finally, the usage of Doppler with the system demonstrated that vessels with a diameter of under 2 mm and low flow could be well captured, although there was some tissue motion artifact that was unavoidable with slow flow Doppler imaging.

5.3.2 PORCINE SPINE

The porcine spine is similar to the human spine and it has historically been used as a training tool for surgeons learning to perform minimally invasive spine procedures. In the case of this study, the porcine model was sacrificed at the farm less than 6 hours prior to imaging. Unfortunately, it is unknown whether it was due to method of sacrifice, method of transportation or natural run-off post-mortem but by the time the surgical corridor was opened the surgeon involved had judged that there was an absence of CSF within the spinal canal. This was judged by the appearance of the spinal cord and the ligamentum flavum after removal of the lamina, as it was mentioned that the presence of CSF would typically be visualized as an outward bulge of the spinal cord from the canal due to the pressure.

With or without the presence of CSF, the imaging tests still provided illuminating sonographic visualizations of the spinal cord and its surrounding anatomy as depicted previously in Figure 4.8. It was of value to note that probe 9 demonstrated significantly better imaging capabilities than probe 8 during the test, and as such, the images depicted are those collected by probe 9. Of note, one of the aspects that probe 9 performed better than 8 was penetration into the spinal cord itself, allowing visualization of not just the central canal as per Figure 4.8 (b), (c), and (e), but also hinting at the “butterfly”-like appearance of the gray matter within the white matter structure of the spinal cord. Although the butterfly-like structure was demonstrated significantly better in the clips, it can also almost be glimpsed within Figure 4.8 (f) where one of the horns appears visible.

It was also observed in a significant number of the images that it was also possible to visualize hyperechoic, strand-like structures within the spinal cord extending outwards

from the central canal towards the contour. The presence of these strands were also less likely to be due to artifacts because of how they shift when the spinal cord was prodded, following the contour and in a manner that suggests physical presence as opposed to being an artifact. This demonstrates both the endoscope's depth penetration capability, as well as the resolution at depth, as the strands were in the range of 0.1 mm in thickness.

The contour of the spinal cord was also well delineated, where the outer layer of meninges was an echogenic layer encapsulating the entirety of the cord. This is crucial for the purpose of understanding how the spinal cord would appear when compressed, because it was then summarily demonstrated that upon using a surgical tool to manipulate or otherwise poke the spinal cord, it resulted in a noticeable indent, even when the surgical tool was out of the plane of view. The contour of the spinal cord noticeably changes between its neutral state and manipulated state, and as the contour of a compressed spinal cord would likely appear to be indented in some manner, this was important to understand in how the two would compare. However, as spinal compression can be more subtle, without fully impinging on the spinal cord itself and resulting instead in a pinched area where the subarachnoid space is no longer present, this would lead to the next point of acknowledging that a compression would likely be more subtle than a grasper or dissector poking at the spinal cord of a porcine cadaver. The window of the endoscope was also sufficient to capture the entire spinal cord in a transverse plane in the same image, and manipulation of the endoscope demonstrated enough freedom to image the structures lateral to the cord as well, implying that should the cord have a larger transverse diameter, such as that of a human spinal cord, this imaging window and angle would still be a suitable choice.

In regard to the presence of CSF, it would normally exist in the sub-arachnoid space as previously depicted in Figure 3.2 on a scale similar to that shown by [83]. However, this fluid space was not visualized upon scanning. The reason that being able to visualize the CSF was originally such an important detail was because it would allow visualization of the fluid compartment and the free-floating spinal nerves. As it would exist as a fluid layer around the spinal cord, any compression of the fluid compartment would result in an indent in the dura contour and a thinning, or vanishing, of the layer between the dura

and the cord or nerves. Without the presence of CSF in our porcine experiment, this could not be visualized.

However, despite the leak of CSF, it is possible that there remained a thin enough layer beneath the arachnoid mater, just sufficient for both the arachnoid and spinal cord to appear distinct. If such a layer indeed existed, it would present as a thin, anechoic space between the echogenic layers of the mater. A similar visualization was seen in many of the images of Figure 4.8, although upon closer inspection the region appears to be less completely anechoic and more hypoechoic, however consistent its presence is. It is also possible that due to the close proximity and the strength of the arachnoid mater as a reflector that it resulted in artifacts within the potential CSF space, resulting in the receiving of echoes when there should have been none.

Finally, although the surgical corridor was larger than that of a proper MISS due to the lack of a surgical high speed burr for bone excision, it was possible to visualize the surgical tools with ultrasound. The contours of the tools were echogenic, and for the tools that had a larger volume, the internals of the tools also appeared comparatively more hypoechoic than the contour. Surprisingly, there was not much shadowing from the tools or other artifacts in Figure 4.8 (g) and (i), although shadowing was visualized as darker areas on the spinal cord when the larger grasper was in use. During the scanning, the surgical tools could be seen in real time when they moved about the ultrasound plane, and manipulation of the spinal cord by the tools could also be visualized, which may prove to be beneficial in guiding surgery. As the endoscope is only 4 mm × 4 mm, it should be able to easily fit down the tubular retractor alongside the other minimally invasive surgical tools in use.

After examining the porcine cadaveric spinal cord using both probe 8 and probe 9 it was confirmed that the images taken by probe 9 were of significantly higher quality. This was most likely due to the lens casting resulting in a thicker base layer for probe 8 than probe 9. In future iterations, this would be amended by taking more care during the lens casting process to ensure that the sensitivity of the probe is high enough even at deeper depths. Outside of fabrication errors, another reason for the discrepancy could be the high

frequency, as probe 9 operated at a lower frequency of 25 MHz compared to the 29.5 MHz of probe 8. While 25 MHz is still considered high frequency ultrasound, it would have a decreased resolution as compared to ones operating at approximately 30 MHz. However, as the trade-off is between resolution and penetration depth, and the 25 MHz probe was capable of delineating the fine layers existing as the spinal cord's contour, the resolution from a 25 MHz probe was demonstrated to be enough for this purpose. In addition, a lower frequency probe may also better visualize the ventral aspects of the spinal cord due to better penetration, although improving the endoscope sensitivity by methods such as using alternative materials for the array may also prove useful.

CHAPTER 6 CONCLUSION

6.1 SUMMARY

Back pain is extremely common among the aging population, and over one million surgical interventions are performed yearly in the US alone. Common causes are due to compressed spinal nerves from pathologies such as disc herniations, spinal stenosis, and spinal tumors. Of these surgeries, an estimated 75% and growing are performed minimally invasively due to a faster patient discharge, a quicker return to normal life, less blood loss, and reduced patient trauma [50]. However, there are limited visualization methods within this minimally invasive surgical corridor, as typical surgical microscopes run into issues such as blind spots and a lack of depth penetration. There is also a variety of complications that are seen in the use of minimally invasive spine surgeries such as dural tears and injuries to the nerve roots, as well as a concerning reoperation rate for such a common surgery. While some of these complications may be attributed to the learning curve of surgeons learning how to perform these interventions, it is likely that the difficulty of visualizing the actual structures within the spinal canal also plays into these concerning rates. Medical ultrasound imaging is therefore proposed to fulfill this need as it is safe, portable, easily manipulated like other minimally invasive surgical instruments, and will be able to provide penetrative imaging to the original optical blind spots. As such, an angled, high frequency ultrasound endoscope was designed, fabricated, and tested for the purpose of assisting surgeons in minimally invasive spine surgeries as additional imaging guidance.

The ultrasound endoscope described in this work was designed for the function of providing high resolution, penetrative imaging out from the bottom of a long and narrow surgical retractor tube. This resulted in a long-necked endoscope measuring 12 cm in “straight” length to accommodate the length of the retractor tube, and an angled tip due to how the spinal canal is approached during the retractor tube’s insertion. As the tube is positioned lateral to the spinal processes, and therefore the surgical approach is open to the dorsal lateral aspect of the spinal cord, it was necessary to include an angle to capture the breadth of the spinal cord. In addition, as the tube itself would have an internal

diameter of potentially less than 16 mm, the probe was designed with a diameter of 4 mm × 4 mm to accommodate both the endoscope itself and other surgical tools simultaneously down the same corridor. To provide the required imaging, the probe would require resolution in both the axial and lateral dimensions to be less than 150 μm, as this would be sufficient to differentiate the layer of CSF within the subarachnoid space, a space that would likely be compressed or vanished in a compressed spinal cord. Other imaging requirements of the probe were to have side lobes suppressed to or under -60 dB along with grating lobes pushed outside of the image when steering the acoustic beam. This was modeled with a KLM model and a Field II simulation, and the array dimensions were 64 elements that are 52 μm tall, 2 mm in length, and 48 μm in pitch with an 8 μm kerf.

The endoscope was fabricated using a mix of techniques from [79], [81] and additional methods tailored to the changed form factors of the angled probe. While there were multiple challenges encountered along the way both due to its increased length and the angled tip, a detailed description of the fabrication methodology is described above in 3.2 FABRICATION. Of the multiple probes that were successfully fabricated, probes 8 and 9 were chosen to proceed onwards with the full battery of tests for characterization, safety testing, and in vivo and ex vivo testing.

Due to fabrication differences, the two probes demonstrated varying characteristics from a difference in operational frequency, sensitivity, bandwidth, impedance measurements, and resolution. While the probes originally aimed for 30 MHz, probe 9 was experimentally fabricated at a lower frequency and operated at approximately 25 MHz, which was accompanied by a lower axial resolution and bandwidth likely due to a mismatched matching layer. Probe 8 exhibited a frequency of approximately 30 MHz with a longer bandwidth, resulting in a better axial resolution, but also demonstrated a lower sensitivity likely also due to a mismatched matching layer. The crosstalk levels of the probes were satisfactory, and while neither probe achieved the resolution demonstrated by the models, they were both well within the required 150 μm.

Safety testing proceeded with challenges faced more due to the testing conditions than due to the changed form factors of the endoscopes. The probes passed the acoustic and thermal testing for MI and TI without issue, producing values in line with that of their sensitivities. To achieve the limits posed by the thermal contact tests the max system driving voltage was reduced from the original ±28.2 V to ±24.5 V. The thermal contact testing protocol was also further refined to accommodate for the dropping temperature that occurs from the evaporation of ultrasound gel at the sample-probe interface.

Proof of concept testing was conducted with an in vivo human wrist of a volunteer and of the spinal cord of an ex vivo pig, sacrificed less than 6 hours prior. The wrist imaging demonstrated well-delineated anatomy of vascular structures, muscles, the skin and subcutaneous layer, and details of the peripheral nerve bundles. The wrist imaging also demonstrated the use of power Doppler, where vessels of less than 2 mm diameter were highlighted, and blood flow was captured in both sagittal and transverse vessels. The porcine cadaver unfortunately did not have sufficient CSF left within the spinal canal for imaging, although there was a sliver of hypoechoic-anechoic space within the echogenic outer layer of the spinal cord's contour that may imply the remnant of some fluid. During the cadaveric testing, probe 9 demonstrated better imaging capabilities than probe 8, and visualized anatomy included the spinal cord and its central canal, the spinal canal walls, tissue debris, epidural fat, and the visualization of linear strands within the spinal cord. In addition, the endoscope was also capable of evaluating the spinal cord's contour as it was manipulated in real-time with a surgical dissector, observing the distortions as it occurred both in and out of the acoustic beam's plane. Through this, it was shown how the endoscope was clearly capable of delineating any abnormalities in the spinal cord's contour, which was one of the expectations of a compressed cord, and the subsequent relief of the pressure. If the thin layer of anechoic-hypoechoic space was indeed remnant CSF, then the endoscope was likewise capable of resolving the space, and assess for deviations in thickness, as was apparent in the sagittal view.

6.2 LIMITATIONS

While the endoscope was able to perform to the expected function, this study was limited in a few different aspects. Primarily, as the endoscopes had been approved by the Research Ethics Board (REB) for use in the operating room, it was originally anticipated that the gathered data would include images of before and after surgical decompression as well as imaging of the human spinal anatomy. Additional benefits of this testing would be evaluating Doppler signals within the spinal canal, visualizing the dural sac when there is the presence of CSF, and the overall dimensions and morphology of the human spinal cord and canal as opposed to that of a porcine model, however similar they may be. As such, while one of the primary objectives of this work had been to evaluate the difference between a compressed and decompressed spinal cord, it was only possible to partially achieve the goal of imaging a spinal cord within a porcine model and demonstrating the state of the contour between neutral and artificially compressed states.

Another limitation of this study was the quantity of endoscopes prepared. While probe 8 and 9 both performed adequately in the characterization and safety tests, they deviated enough that it would be worth exploring to understand what exact parameters led to the better images from probe 9. Furthermore, having more endoscopes prepared would also be useful in the case of malfunctions in the clinical space, as well as a more consistent performance and capability evaluation.

6.3 FUTURE WORK

Building off the limitations, future work in this realm would entail taking the endoscopes to the OR setting and evaluating its clinical performance, obtaining a surgeon's insight on the usefulness of the probe, what changes the surgeons might find beneficial for better use, and eventually enough quantitative patient data to evaluate if the probe can actually decrease the rates of complications and/or reoperations. As such, future trials will target assessing the subarachnoid space for the consistency of the CSF layer, the presence of blood flow within the spinal vascular system, and evaluating the morphology of a compressed spinal cord, nerve, or nerve roots due to pathologies such as herniated discs, spinal stenosis, and spinal tumors.

More endoscopes of this variety will also be fabricated, with the frequency targeted to be between 25 MHz and 30 MHz, and with more care taken during the process to improve the sensitivity of the final completed endoscope. In addition, exploration into other materials for the array to likewise enhance the properties of the endoscope may also be pursued.

Finally, as surgeries overall are trending towards minimally invasive means and this probe was tailored for imaging down retractor tubes, it should similarly be capable of functioning as imaging guidance for other minimally invasive surgeries featuring channels of this similar size. With a diameter of 4 mm × 4 mm and a neck length of 12 cm, this endoscope can be fit down various straight and narrow corridors, and the ease of maneuvering a tool shaped to mimic other more familiar minimally invasive surgical instruments will also reduce the learning curve for its use. As such, it may be of interest to explore other minimally invasive surgeries where angled, high resolution ultrasound may be of use.

6.4 FINAL CONCLUSION

This work encompassed the design, fabrication, in-lab testing, and anatomy testing of an angled, high resolution ultrasound endoscope intended to verify successful decompressions in minimally invasive spine surgeries. While the endoscope has yet to complete patient testing to evaluate its clinical performance, the design and fabrication process has been recorded and demonstrated to produce probes that achieve the desired resolution, imaging depth, and form factor. When testing within the ex vivo porcine model, the endoscope was capable of clearly delineating the spinal cord, its surrounding anatomy, and even provide sufficient penetrative imaging to visualize the central canal and the boundary between gray and white matter. Furthermore, the capability to evaluate an abnormal spinal cord contour due to indentation from surgical tools within and outside of the imaging plane also demonstrates an ability to assess for contour abnormalities, which would be an anticipated feature of a compressed spinal cord. The endoscope in itself was a success, and its imaging capabilities should be sufficient at capturing the relevant details between a compressed and freed spinal cord. Future work will eventually

bring the endoscope to the OR for further evaluation, and with the demonstrated capabilities it will hopefully be able to reduce the complication and reoperation rates of minimally invasive spine surgeries.

BIBLIOGRAPHY

[1] A. Carovac, F. Smajlovic, and D. Junuzovic, ‘Application of Ultrasound in Medicine’, *Acta Inform. Medica*, vol. 19, no. 3, p. 168, 2011, doi: 10.5455/aim.2011.19.168-171.

[2] P. H. Lento and S. Primack, ‘Advances and utility of diagnostic ultrasound in musculoskeletal medicine’, *Curr. Rev. Musculoskelet. Med.*, vol. 1, no. 1, pp. 24–31, Mar. 2008, doi: 10.1007/s12178-007-9002-3.

[3] W. Lin, M. Chen, B. Li, W. Wang, S. Li, and G. Lyu, ‘Intraoperative ultrasound-guided percutaneous hepatocholangiostomy applied in the cholangioscopic lithotripsy for hepatolithiasis and choledocholithiasis’, *Surg. Endosc.*, vol. 37, no. 1, pp. 486–493, Jan. 2023, doi: 10.1007/s00464-022-09540-z.

[4] G. Kimchi, A. Orlev, A. Hadanny, N. Knoller, and R. Harel, ‘Minimally Invasive Spine Surgery: The Learning Curve of a Single Surgeon’, *Glob. Spine J.*, vol. 10, no. 8, pp. 1022–1026, Dec. 2020, doi: 10.1177/2192568219880872.

[5] J. Yuan, Sorah Rhee, and X. N. Jiang, ‘60 MHz PMN-PT based 1-3 composite transducer for IVUS imaging’, in *2008 IEEE Ultrasonics Symposium*, Beijing, China: IEEE, Nov. 2008, pp. 682–685. doi: 10.1109/ULTSYM.2008.0164.

[6] T. Xu, C. Tekes, S. Satir, E. Arkan, M. Ghovanloo, and F. L. Degertekin, ‘Design, modeling and characterization of a 35MHz 1-D CMUT phased array’, in *2013 IEEE International Ultrasonics Symposium (IUS)*, Prague, Czech Republic: IEEE, Jul. 2013, pp. 1987–1990. doi: 10.1109/ULTSYM.2013.0507.

[7] K. K. Shung, ‘High Frequency Ultrasonic Imaging’, *J. Med. Ultrasound*, vol. 17, no. 1, pp. 25–30, 2009, doi: 10.1016/S0929-6441(09)60012-6.

[8] B.-L. Chen *et al.*, ‘Surgical versus non-operative treatment for lumbar disc herniation: a systematic review and meta-analysis’, *Clin. Rehabil.*, vol. 32, no. 2, pp. 146–160, Feb. 2018, doi: 10.1177/0269215517719952.

[9] K. Ono, K. Ohmori, R. Yoneyama, O. Matsushige, and T. Majima, ‘Risk Factors and Surgical Management of Recurrent Herniation after Full-Endoscopic Lumbar Discectomy Using Interlaminar Approach’, *J. Clin. Med.*, vol. 11, no. 3, p. 748, Jan. 2022, doi: 10.3390/jcm11030748.

[10] Y. Ahn, ‘A Historical Review of Endoscopic Spinal Discectomy’, *World Neurosurg.*, vol. 145, pp. 591–596, Jan. 2021, doi: 10.1016/j.wneu.2020.08.008.

[11] Y. Ahn, ‘Current techniques of endoscopic decompression in spine surgery’, *Ann. Transl. Med.*, vol. 7, no. S5, pp. S169–S169, Sep. 2019, doi: 10.21037/atm.2019.07.98.

[12] F. F. Bombieri, R. Shafafy, and S. Elsayed, ‘Complications associated with lumbar discectomy surgical techniques: a systematic review’, *J. Spine Surg.*, vol. 8, no. 3, 2022.

[13] A. J. Clark, M. M. Safaee, N. R. Khan, M. T. Brown, and K. T. Foley, ‘Tubular microdiscectomy: techniques, complication avoidance, and review of the literature’, *Neurosurg. Focus*, vol. 43, no. 2, p. E7, Aug. 2017, doi: 10.3171/2017.5.FOCUS17202.

[14] S. Masuda *et al.*, ‘Reoperation Rates of Microendoscopic Discectomy Compared With Conventional Open Lumbar Discectomy: A Large-database Study’, *Clin. Orthop.*, vol. 481, no. 1, pp. 145–154, Jan. 2023, doi: 10.1097/CORR.0000000000002322.

[15] J. Tat, J. Tat, S. Yoon, A. J. M. Yee, and J. Larouche, ‘Intraoperative Ultrasound in Spine Decompression Surgery: A Systematic Review’, *Spine*, vol. 47, no. 2, pp. E73–E85, Jan. 2022, doi: 10.1097/BRS.0000000000004111.

[16] T. G. Landry and J. A. Brown, ‘B-mode and Doppler imaging of in vivo rat brain and ex vivo human brain with a high frequency endoscopic phased array’, in *2019 IEEE International Ultrasonics Symposium (IUS)*, Glasgow, United Kingdom: IEEE, Oct. 2019, pp. 2133–2136. doi: 10.1109/ULTSYM.2019.8925902.

[17] D. Drazin, C. Lagman, S. Bhargava, M. Nuño, T. T. Kim, and J. P. Johnson, ‘National trends following decompression, discectomy, and fusion in octogenarians and nonagenarians’, *Acta Neurochir. (Wien)*, vol. 159, no. 3, pp. 517–525, Mar. 2017, doi: 10.1007/s00701-016-3056-1.

[18] M. Miscusi *et al.*, ‘Comparison of minimally invasive surgery with standard open surgery for vertebral thoracic metastases causing acute myelopathy in patients with short- or mid-term life expectancy: surgical technique and early clinical results’, *J. Neurosurg. Spine*, vol. 22, no. 5, pp. 518–525, May 2015, doi: 10.3171/2014.10.SPINE131201.

[19] J. P. Urban and S. Roberts, ‘Degeneration of the intervertebral disc’, *Arthritis Res. Ther.*, vol. 5, no. 3, p. 120, 2003, doi: 10.1186/ar629.

[20] V. Kotheeranurak *et al.*, ‘Comparison of full-endoscopic and tubular-based microscopic decompression in patients with lumbar spinal stenosis: a randomized controlled trial’, *Eur. Spine J.*, Apr. 2023, doi: 10.1007/s00586-023-07678-5.

[21] P. S. Gadjradj *et al.*, ‘Full endoscopic versus open discectomy for sciatica: randomised controlled non-inferiority trial’, *BMJ*, p. e065846, Feb. 2022, doi: 10.1136/bmj-2021-065846.

[22] A. Patil *et al.*, ‘Microendoscopic discectomy for lumbar disc herniations’, *J. Craniovertebral Junction Spine*, vol. 9, no. 3, p. 156, 2018, doi: 10.4103/jcvjs.JCVJS_61_18.

[23] L. H. Kim *et al.*, ‘Expenditures and Health Care Utilization Among Adults With Newly Diagnosed Low Back and Lower Extremity Pain’, *JAMA Netw. Open*, vol. 2, no. 5, p. e193676, May 2019, doi: 10.1001/jamanetworkopen.2019.3676.

[24] F. ÖZer, *Minimally invasive procedures in spine surgery*. Place of publication not identified: Fahir Özer, 2016.

[25] N. Patrick, E. Emanski, and M. A. Knaub, ‘Acute and Chronic Low Back Pain’, *Med. Clin. North Am.*, vol. 98, no. 4, pp. 777–789, Jul. 2014, doi: 10.1016/j.mcna.2014.03.005.

[26] S. Ramanathan, A. Rapp, M. Perez-Cruet, and D. K. Fahim, ‘Long-Term Reoperation Rates After Open versus Minimally Invasive Spine Surgery for Degenerative Lumbar Disease: Five Year Follow-Up of 2130 Patients’, *World Neurosurg.*, p. S1878875022016539, Nov. 2022, doi: 10.1016/j.wneu.2022.11.100.

[27] K. Schöller, M. Alimi, G.-T. Cong, P. Christos, and R. Härtl, ‘Lumbar Spinal Stenosis Associated With Degenerative Lumbar Spondylolisthesis: A Systematic Review and Meta-analysis of Secondary Fusion Rates Following Open vs Minimally Invasive Decompression’, *Neurosurgery*, vol. 80, no. 3, pp. 355–367, Mar. 2017, doi: 10.1093/neuros/nyw091.

[28] A. A. Momin and M. P. Steinmetz, ‘Evolution of Minimally Invasive Lumbar Spine Surgery’, *World Neurosurg.*, vol. 140, pp. 622–626, Aug. 2020, doi: 10.1016/j.wneu.2020.05.071.

[29] J. Levy, D. L. Barrett, N. Harris, J. J. Jeong, X. Yang, and S. C. Chen, ‘High-frequency ultrasound in clinical dermatology: a review’, *Ultrasound J.*, vol. 13, no. 1, p. 24, Dec. 2021, doi: 10.1186/s13089-021-00222-w.

[30] T. Cummins, P. Eliahoo, and K. Kirk Shung, ‘High-Frequency Ultrasound Array Designed for Ultrasound-Guided Breast Biopsy’, *IEEE Trans. Ultrason. Ferroelectr. Freq. Control*, vol. 63, no. 6, pp. 817–827, Jun. 2016, doi: 10.1109/TUFFC.2016.2548993.

[31] B. Zhu, N. Y. Chan, J. Dai, K. K. Shung, S. Takeuchi, and Q. Zhou, ‘New fabrication of high-frequency (100-MHz) ultrasound PZT film kerfless linear array [Correspondence]’, *IEEE Trans. Ultrason. Ferroelectr. Freq. Control*, vol. 60, no. 4, pp. 854–857, Apr. 2013, doi: 10.1109/TUFFC.2013.2635.

[32] F. Gaillard, ‘Intervertebral disc | Radiology Reference Article | Radiopaedia.org’, *Radiopaedia*. https://radiopaedia.org/articles/intervertebral-disc?lang=us (accessed Mar. 20, 2023).

[33] A. Frostell, R. Hakim, E. P. Thelin, P. Mattsson, and M. Svensson, ‘A Review of the Segmental Diameter of the Healthy Human Spinal Cord’, *Front. Neurol.*, vol. 7, Dec. 2016, doi: 10.3389/fneur.2016.00238.

[34] M. L. Yáñez, J. J. Miller, and T. T. Batchelor, ‘Diagnosis and treatment of epidural metastases: Epidural Metastases’, *Cancer*, vol. 123, no. 7, pp. 1106–1114, Apr. 2017, doi: 10.1002/cncr.30521.

[35] C. Cunha, A. J. Silva, P. Pereira, R. Vaz, R. M. Gonçalves, and M. A. Barbosa, ‘The inflammatory response in the regression of lumbar disc herniation’, *Arthritis Res. Ther.*, vol. 20, no. 1, p. 251, Dec. 2018, doi: 10.1186/s13075-018-1743-4.

[36] A. Suzuki and H. Nakamura, ‘Microendoscopic Lumbar Posterior Decompression Surgery for Lumbar Spinal Stenosis: Literature Review’, *Medicina (Mex.)*, vol. 58, no. 3, p. 384, Mar. 2022, doi: 10.3390/medicina58030384.

[37] M. Aljoghaiman, A. Martyniuk, F. Farrokhyar, A. Cenic, and E. Kachur, 'Survey of lumbar discectomy practices: 10 years in the making', *J. Spine Surg.*, vol. 6, no. 3, pp. 572–580, Sep. 2020, doi: 10.21037/jss-20-519.

[38] G. Meyer *et al.*, 'Percutaneous Endoscopic Lumbar Discectomy Versus Microdiscectomy for the Treatment of Lumbar Disc Herniation: Pain, Disability, and Complication Rate—A Randomized Clinical Trial', *Int. J. Spine Surg.*, vol. 14, no. 1, pp. 72–78, Feb. 2020, doi: 10.14444/7010.

[39] J. Patel, V. Kundnani, and S. Kuriya, '"A decade with micro-tubular decompression": Peri-operative complications and surgical outcomes in single and multilevel lumbar canal stenosis', *Int. Orthop.*, vol. 45, no. 7, pp. 1881–1889, Jul. 2021, doi: 10.1007/s00264-021-05032-2.

[40] M. Shi *et al.*, 'Posterior cervical full-endoscopic technique for the treatment of cervical spondylotic radiculopathy with foraminal bony stenosis: A retrospective study', *Front. Surg.*, vol. 9, p. 1035758, Jan. 2023, doi: 10.3389/fsurg.2022.1035758.

[41] J. N. A. Gibson and G. Waddell, 'Surgery for Degenerative Lumbar Spondylosis: Updated Cochrane Review':, *Spine*, vol. 30, no. 20, pp. 2312–2320, Oct. 2005, doi: 10.1097/01.brs.0000182315.88558.9c.

[42] H. I. Süner *et al.*, 'Comparison of the Tubular Approach and Uniportal Interlaminar Full-Endoscopic Approach in the Treatment of Lumbar Spinal Stenosis: Our 3-Year Results', *World Neurosurg.*, p. S1878875023001626, Feb. 2023, doi: 10.1016/j.wneu.2023.02.022.

[43] N. S. C. and O. Branch, 'Spinal Stenosis', *National Institute of Arthritis and Musculoskeletal and Skin Diseases*, Apr. 11, 2017. https://www.niams.nih.gov/health-topics/spinal-stenosis (accessed May 07, 2023).

[44] S. Tsukamoto *et al.*, 'Current Overview of Treatment for Metastatic Bone Disease', *Curr. Oncol.*, vol. 28, no. 5, pp. 3347–3372, Aug. 2021, doi: 10.3390/curroncol28050290.

[45] T. Yamada *et al.*, 'Hypertrophy of the ligamentum flavum in lumbar spinal canal stenosis is associated with abnormal accumulation of specific lipids', *Sci. Rep.*, vol. 11, no. 1, p. 23515, Dec. 2021, doi: 10.1038/s41598-021-02818-7.

[46] U. Hubbe *et al.*, 'Double tubular minimally invasive spine surgery: a novel technique expands the surgical visual field during resection of intradural pathologies', *J. Neurosurg. Spine*, vol. 36, no. 1, pp. 160–163, Jan. 2022, doi: 10.3171/2021.3.SPINE2164.

[47] D. Bakar *et al.*, 'Decompression surgery for spinal metastases: a systematic review', *Neurosurg. Focus*, vol. 41, no. 2, p. E2, Aug. 2016, doi: 10.3171/2016.6.FOCUS16166.

[48] J. M. Orenday-Barraza *et al.*, '10-Year Trends in the Surgical Management of Patients with Spinal Metastases: A Scoping Review', *World Neurosurg.*, vol. 157, pp. 170-186.e3, Jan. 2022, doi: 10.1016/j.wneu.2021.10.086.

[49] F. J. McCabe, M. M. Jadaan, F. Byrne, A. T. Devitt, and J. P. McCabe, ‘Spinal metastasis: The rise of minimally invasive surgery’, *The Surgeon*, vol. 20, no. 5, pp. 328–333, Oct. 2022, doi: 10.1016/j.surge.2021.08.007.

[50] J. L. Goldberg, R. Härtl, and E. Elowitz, ‘Minimally Invasive Spine Surgery: An Overview’, *World Neurosurg.*, vol. 163, pp. 214–227, Jul. 2022, doi: 10.1016/j.wneu.2022.03.114.

[51] ‘Lumbar decompression surgery - How it’s performed’, *nhs.uk*, Oct. 24, 2017. https://www.nhs.uk/conditions/lumbar-decompression-surgery/what-happens/ (accessed Apr. 08, 2023).

[52] M. Rodriguez and M. D. Peer-Reviewed, ‘Surgical Procedure for Lumbar Laminectomy (Open Decompression) in Spinal Stenosis | Spine-health’. https://www.spine-health.com/treatment/back-surgery/surgical-procedure-lumbar-laminectomy-open-decompression-spinal-stenosis (accessed May 07, 2023).

[53] M. G. Yasargil, ‘Microsurgical Operation of Herniated Lumbar Disc’, in *Lumbar Disc Adult Hydrocephalus*, R. Wüllenweber, M. Brock, J. Hamer, M. Klinger, and O. Spoerri, Eds., in Advances in Neurosurgery, vol. 4. Berlin, Heidelberg: Springer Berlin Heidelberg, 1977, pp. 81–81. doi: 10.1007/978-3-642-66578-3_16.

[54] W. Caspar, ‘A New Surgical Procedure for Lumbar Disc Herniation Causing Less Tissue Damage Through a Microsurgical Approach’, in *Lumbar Disc Adult Hydrocephalus*, R. Wüllenweber, M. Brock, J. Hamer, M. Klinger, and O. Spoerri, Eds., in Advances in Neurosurgery, vol. 4. Berlin, Heidelberg: Springer Berlin Heidelberg, 1977, pp. 74–80. doi: 10.1007/978-3-642-66578-3_15.

[55] S. Ruetten, M. Komp, and G. Godolias, ‘An Extreme Lateral Access for the Surgery of Lumbar Disc Herniations Inside the Spinal Canal Using the Full-Endoscopic Uniportal Transforaminal Approach–Technique and Prospective Results of 463 Patients’:, *Spine*, vol. 30, no. 22, pp. 2570–2578, Nov. 2005, doi: 10.1097/01.brs.0000186327.21435.cc.

[56] G. A. W. Gooding’, J. E. Boggan, and P. R. Weinstein, ‘Intraoperative Sonography during Lumbar Laminectomy’:, p. 3.

[57] T. Säteri, J. Nurro, O.-P. Hätinen, M. Hakulinen, V. Leinonen, and A.-P. Elomaa, ‘Ex Vivo Porcine Models Are Valid for Testing and Training Microsurgical Lumbar Decompression Techniques’, *World Neurosurg.*, vol. 155, pp. e64–e74, Nov. 2021, doi: 10.1016/j.wneu.2021.07.147.

[58] H. Abbasi and A. Abbasi, ‘Using Porcine Cadavers as an Alternative to Human Cadavers for Teaching Minimally Invasive Spinal Fusion: Proof of Concept and Anatomical Comparison’, *Cureus*, Nov. 2019, doi: 10.7759/cureus.6158.

[59] S.-R. Sheng *et al.*, ‘Comparison of Cervical Spine Anatomy in Calves, Pigs and Humans’, *PLOS ONE*, vol. 11, no. 2, p. e0148610, Feb. 2016, doi: 10.1371/journal.pone.0148610.

[60] C. Weber-Levine *et al.*, ‘Porcine Model of Spinal Cord Injury: A Systematic Review’, *Neurotrauma Rep.*, vol. 3, no. 1, pp. 352–368, Sep. 2022, doi: 10.1089/neur.2022.0038.

[61] V. R. Yingling, J. P. Callaghan, and S. M. McGill, ‘The porcine cervical spine as a model of the human lumbar spine: an anatomical, geometric, and functional comparison’, *J. Spinal Disord.*, vol. 12, no. 5, pp. 415–423, Oct. 1999.

[62] R. S. C. Cobbold, *Foundations of biomedical ultrasound*. Oxford ; New York: Oxford University Press, 2007.

[63] A. Bezanson, ‘Design, fabrication, and performance of high-frequency phased-array ultrasonic endoscopes’, Dalhousie University, 2020.

[64] W. R. Hedrick and D. L. Hykes, ‘Beam Steering and Focusing With Linear Phiased Arrays’, *J. Diagn. Med. Sonogr.*, vol. 12, no. 5, pp. 211–215, Sep. 1996, doi: 10.1177/875647939601200502.

[65] J. Camacho, M. Parrilla, and C. Fritsch, ‘Phase Coherence Imaging’, *IEEE Trans. Ultrason. Ferroelectr. Freq. Control*, vol. 56, no. 5, pp. 958–974, May 2009, doi: 10.1109/TUFFC.2009.1128.

[66] Z. Torbatian, R. Adamson, and J. A. Brown, ‘Experimental verification of pulse-probing technique for improving phase coherence grating lobe suppression’, *IEEE Trans. Ultrason. Ferroelectr. Freq. Control*, vol. 60, no. 7, pp. 1324–1332, Jul. 2013, doi: 10.1109/TUFFC.2013.2706.

[67] P. Marechal, F. Levassort, L.-P. Tran-Huu-Hue, and M. Lethiecq, ‘Effect of acoustical properties of a lens on the pulse-echo response of a single element transducer’, in *IEEE Ultrasonics Symposium, 2004*, Montreal, Canada: IEEE, 2004, pp. 1651–1654. doi: 10.1109/ULTSYM.2004.1418139.

[68] R. Krimholtz, D. A. Leedom, and G. L. Matthaei, ‘New equivalent circuits for elementary piezoelectric transducers’, *Electron. Lett.*, vol. 6, no. 13, p. 398, 1970, doi: 10.1049/el:19700280.

[69] I. Bickle, ‘Ultrasound-guided biopsy | Radiology Reference Article | Radiopaedia.org’, *Radiopaedia*. https://radiopaedia.org/articles/ultrasound-guided-biopsy-1 (accessed Apr. 17, 2023).

[70] Z. Pilecki, B. Koczy, M. Mielnik, G. Pilecki, J. Dzielicki, and W. Jakubowski, ‘Basic dissecting techniques in ultrasound-guided surgery’, *J. Ultrason.*, vol. 14, no. 57, pp. 171–178, Jun. 2014, doi: 10.15557/JoU.2014.0017.

[71] T. Aoyama, K. Hida, M. Akino, S. Yano, and Y. Iwasaki, ‘Detection of Residual Disc Hernia Material and Confirmation of Nerve Root Decompression at Lumbar Disc Herniation Surgery by Intraoperative Ultrasound’, *Ultrasound Med. Biol.*, vol. 35, no. 6, pp. 920–927, Jun. 2009, doi: 10.1016/j.ultrasmedbio.2008.12.014.

[72] T. A. Ritter, T. R. Shrout, R. Tutwiler, and K. K. Shung, ‘A 30-MHz piezo-composite ultrasound array for medical imaging applications’, *IEEE Trans. Ultrason. Ferroelectr. Freq. Control*, vol. 49, no. 2, pp. 217–230, Feb. 2002, doi: 10.1109/58.985706.

[73] H. R. Chabok, J. M. Cannata, H. H. Kim, J. A. Williams, J. Park, and K. K. Shung, ‘A high-frequency annular-array transducer using an interdigital bonded 1-3 composite’, *IEEE Trans. Ultrason. Ferroelectr. Freq. Control*, vol. 58, no. 1, pp. 206–214, Jan. 2011, doi: 10.1109/TUFFC.2011.1787.

[74] M. Lukacs, M. Sayer, G. Lockwood, and S. Foster, ‘Laser micromachined high frequency ultrasonic arrays’, in *1999 IEEE Ultrasonics Symposium. Proceedings. International Symposium (Cat. No.99CH37027)*, Caesars Tahoe, NV, USA: IEEE, 1999, pp. 1209–1212. doi: 10.1109/ULTSYM.1999.849214.

[75] C. Fei *et al.*, ‘Design of matching layers for high-frequency ultrasonic transducers’, *Appl. Phys. Lett.*, vol. 107, no. 12, p. 123505, Sep. 2015, doi: 10.1063/1.4931703.

[76] J. Brown, S. Sharma, J. Leadbetter, S. Cochran, and R. Adamson, ‘Vacuum deposition of mass-spring matching layers for high-frequency ultrasound transducers’, in *2014 IEEE International Ultrasonics Symposium*, Chicago, IL, USA: IEEE, Sep. 2014, pp. 101–104. doi: 10.1109/ULTSYM.2014.0026.

[77] J. Chen *et al.*, ‘A Review of UltraHigh Frequency Ultrasonic Transducers’, *Front. Mater.*, vol. 8, p. 733358, Jan. 2022, doi: 10.3389/fmats.2021.733358.

[78] J. M. Cannata, T. A. Ritter, Wo-Hsing Chen, R. H. Silverman, and K. K. Shung, ‘Design of efficient, broadband single-element (20-80 MHz) ultrasonic transducers for medical imaging applications’, *IEEE Trans. Ultrason. Ferroelectr. Freq. Control*, vol. 50, no. 11, pp. 1548–1557, Nov. 2003, doi: 10.1109/TUFFC.2003.1251138.

[79] A. Bezanson, R. Adamson, and J. A. Brown, ‘Fabrication and performance of a miniaturized 64-element high-frequency endoscopic phased array’, *IEEE Trans. Ultrason. Ferroelectr. Freq. Control*, vol. 61, no. 1, pp. 33–43, Jan. 2014, doi: 10.1109/TUFFC.2014.6689774.

[80] Z. Han *et al.*, ‘Phased-Array Transducer for Intracardiac Echocardiography Based on 1–3 Piezocomposite’, *Front. Mater.*, vol. 8, p. 663926, Apr. 2021, doi: 10.3389/fmats.2021.663926.

[81] T. G. Landry *et al.*, ‘Endoscopic Coregistered Ultrasound Imaging and Precision Histotripsy: Initial *In Vivo* Evaluation’, *BME Front.*, vol. 2022, pp. 1–14, Jul. 2022, doi: 10.34133/2022/9794321.

[82] M. Zaaroor, G. Kósa, A. Peri-Eran, I. Maharil, M. Shoham, and D. Goldsher, ‘Morphological Study of the Spinal Canal Content for Subarachnoid Endoscopy’, *Min - Minim. Invasive Neurosurg.*, vol. 49, no. 4, pp. 220–226, Aug. 2006, doi: 10.1055/s-2006-948000.

[83] ‘Imaging the spinal cord in swine | FUJIFILM VisualSonics’. https://www.visualsonics.com/resource/featured-images/imaging-spinal-cord-swine (accessed Jun. 14, 2023).

[84] Y. Liu, X. Zhou, J. Ma, Y. Ge, and X. Cao, ‘The diameters and number of nerve fibers in spinal nerve roots’, *J. Spinal Cord Med.*, vol. 38, no. 4, pp. 532–537, Jul. 2015, doi: 10.1179/1079026814Z.000000000273.

[85] J. L. Sherman, P. Y. Nassaux, and C. M. Citrin, ‘Measurements of the normal cervical spinal cord on MR imaging’, *AJNR Am. J. Neuroradiol.*, vol. 11, no. 2, pp. 369–372, 1990.

[86] P. R. Hoskins, K. Martin, and A. Thrush, Eds., ‘The British Medical Ultrasound Society. Guidelines for the safe use of diagnostic ultrasound equipment’, in *Diagnostic Ultrasound*, 2nd ed.Cambridge University Press, 2010, pp. 217–225. doi: 10.1017/CBO9780511750885.020.

[87] T. Sen, O. Tufekcioglu, and Y. Koza, ‘Mechanical index’, *Anadolu Kardiyol. Derg. Anatol. J. Cardiol.*, vol. 15, no. 4, pp. 334–336, Apr. 2015, doi: 10.5152/akd.2015.6061.

[88] J. Gurthie, ‘Ophthalmic Sonography: Through the Lens of a Sonographer’, *J. Diagn. Med. Sonogr.*, vol. 37, no. 6, pp. 517–520, Nov. 2021, doi: 10.1177/87564793211019366.

[89] C. Samson, ‘High-Frequency Ultrasound Beamforming for a Minimally Invasive Endoscopic Probe’, 2020.

[90] H.-C. Yang, J. Cannata, J. Williams, and K. K. Shung, ‘Crosstalk reduction for high-frequency linear-array ultrasound transducers using 1-3 piezocomposites with pseudo-random pillars’, *IEEE Trans. Ultrason. Ferroelectr. Freq. Control*, vol. 59, no. 10, pp. 2312–2321, Oct. 2012, doi: 10.1109/TUFFC.2012.2456.

[91] Shiwei Zhou, G. L. Wojcik, and J. A. Hossack, ‘An approach for reducing adjacent element crosstalk in ultrasound arrays’, *IEEE Trans. Ultrason. Ferroelectr. Freq. Control*, vol. 50, no. 12, pp. 1752–1761, Dec. 2003, doi: 10.1109/TUFFC.2003.1256316.

[92] ‘Insertion loss measurement | Signal Processing’. https://www.signal-processing.com/insertion-loss.php (accessed Apr. 24, 2023).

[93] C. E. M. Demore, J. A. Brown, and G. R. Lockwood, ‘Investigation of cross talk in Kerfless annular arrays for high-frequency imaging’, *IEEE Trans. Ultrason. Ferroelectr. Freq. Control*, vol. 53, no. 5, pp. 1046–1056, May 2006, doi: 10.1109/TUFFC.2006.1632694.